LARGE EDDY SIMULATION OF THE FLOW AROUND A FINITE SQUARE PRISM MOUNTED ON A GROUND PLANE

A Thesis Submitted to the College of

Graduate and Postdoctoral Studies

In Partial Fulfillment of the Requirements

For the Degree of Doctor of Philosophy

In the Department of Mechanical Engineering

University of Saskatchewan

Saskatoon, Saskatchewan

By

NADER MOAZAMIGOODARZI

Permission to Use

In presenting this thesis in partial fulfilment of the requirements for a Postgraduate degree from the University of Saskatchewan, I agree that the Libraries of this University may make it freely available for inspection. I further agree that permission for copying of this thesis in any manner, in whole or in part, for scholarly purposes may be granted by Dr. Donald J. Bergstrom who supervised my thesis work or, in his absence, by the Head of the Department or the Dean of the College in which my thesis work was done. It is understood that any copying or publication or use of this thesis or parts thereof for financial gain shall not be allowed without my written permission. It is also understood that due recognition shall be given to me and to the University of Saskatchewan in any scholarly use which may be made of any

material in my thesis.

Requests for permission to copy or to make other use of material in this thesis in whole or part should be addressed to:

Head of the Department of Mechanical Engineering
57 Campus Drive, College of Engineering
University of Saskatchewan
Saskatoon, Saskatchewan S7N 5A9
Canada

OR

Dean
College of Graduate and Postdoctoral Studies
University of Saskatchewan
116 Thorvaldson Building, 110 Science Place
Saskatoon, Saskatchewan S7N 5C9
Canada

Abstract

Dynamic subgrid-scale models for large eddy simulation (LES) offer the promise of being able to dynamically calibrate the residual stress field to the local flow conditions. The first part of thesis reports on the application of two different dynamic subgrid-scale (SGS) models to predict the turbulent wake of a finite-height square prism mounted vertically on a ground plane. The prism aspect ratio was AR = 3, and the Reynolds number, based on the prism width and freestream velocity, was Re = 500. The approach flow was laminar with a thin boundary layer; the thickness at the location of the prism was approximately 0.2D. The flow over the top of the prism interacts with the flow along the ground plane and the vertical shear layers from the sidewalls to create a complicated wake structure. Both a linear dynamic Smagorinsky model (DSM) and dynamic nonlinear model (DNM) were implemented and tested for their ability to resolve the complex wake structure. Investigation of the dissipation of turbulence kinetic energy reveals that the DSM has a much larger SGS dissipation, whereas the DNM has a greater resolved-scale dissipation. The backscatter associated with the DSM is much more pervasive than that predicted by the DNM, which accounts for the numerical instability of the DSM. Overall, specific differences are observed in the wake predicted by the two SGS models, including some features of the mean velocity field.

The second part of the thesis explores the phase-averaged structure of the wake based on the prediction of the DNM. Phase-averaging based on the Strouhal number reveals a wake structure with quasi-periodic features that is much different from the mean vorticity field, which is characterised by two pairs of counter-rotating streamwise vortex tubes. The phase-averaged near-wake structure is dominated by vertical vortex cores formed by the shear layers being shed from the two sides of the prism. These tubes re-orient and interact as they detach from the prism and move downstream, giving evidence of the half-loop structures documented in previous studies. Each half-loop consists of a short vertical core near the ground plane, and a connector strand that tilts back upstream toward the prism. The shedding process is almost symmetric just downstream of the prism, but develops an asymmetric pattern farther downstream, characterised by the alternate development of half-loop structures on opposite sides of the wake. Further downstream in the wake, the phase-averaged flow is dominated by approximately streamwise vortex tubes associated with the connector strands.

Acknowledgments

I would like to first thank my PhD supervisor, Professor Donald J. Bergstrom, for being patient and supportive from the beginning to completion.

I sincerely thank my advisory committee members, Prof. David Sumner, Prof. Chris Zhang, Prof. Richard Evitts, and Prof. Ron Barron for their valuable comments and feedback on this work. I also would like to thank the staff of the College of Engineering.

In the end, I am grateful to the most wonderful one.

Table of Contents

List of Figures

List of Tables

Nomenclature

English Symbols

AR aspect ratio

A_j flux term

C_N model coefficients

C_s model coefficient

C_W model coefficients

D side length of square prism

E error function

f frequency

H height of the cylinder

H_1 height of the domain

i index

j index

K turbulence kinetic energy

L dimension of the physical domain

L_1 prism upstream

L_2 prism upstream

L_{ij} Leonard stress

l Kolmogorov length scale

M_{ij} differential tensorial function

N phase number

N_{ij} differential tensorial function

N_x number of volumes on the prism in the streamwise direction

N_y number of volumes on the prism in the vertical direction

N_z number of volumes on the prism in the transverse direction

p pressure

Q second invariant of the velocity gradient tensor

Re Reynolds number

S_{ij} strain rate tensor

St Strouhal number

t time

T period time

T_{ij} test-grid level SGS stress

U free stream velocity

u_i velocity component in the i direction

W dimension of the physical domain

W_1 prism sidewall to domain

W_{ij} differential tensorial function

X streamwise direction

x_j spatial coordinate in the j direction

Y vertical direction

Z transverse direction

Greek Symbols

α_{ij} basis function

β_{ij} basis function

γ_{ij} basis functions

δ boundary layer thickness

Δ grid filter size

Δt time-step

Δx grid size

ε resolved-scale dissipation of turbulence kinetic energy

$\mathcal{E}_{SGS}$ SGS dissipation of turbulence kinetic energy

ζ_{ij} basis functions

η_{ij} basis functions

λ_{ij} basis functions

ν kinematic viscosity

ν_{SGS} subgrid-scale viscosity

ρ fluid density

τ shear stress

τ_{ij} grid level SGS stress

υ_{sgs} SGS viscosity

$\upsilon_{sgs}(max)$ maximum SGS viscosity

$\upsilon_{sgs}(min)$ minimum SGS viscosity

$\emptyset$ mass flux

Ω rotation rate tensor

Abbreviations

3D Three-dimensional

ABL atmospheric boundary layer

CFD Computational Fluid Dynamics

CFL Courant–Friedrichs–Lewy number

CV Control Volume

DNM Dynamic Nonlinear Model

DNS Direct Numerical Simulation

DSM Dynamic Smagorinsky Model

EVM Eddy Viscosity Model

FFT Fast Fourier Transform

FVM Finite-Volume Method

LDM Realizable Linear Dynamic Model

LES Large Eddy Simulation

MG Multi-Grid

NDM Realizable Nonlinear Dynamic Model

PIV Particle Image Velocimetry

QUICK Quadratic Upwind Interpolation for Convective Kinematics

RANS Reynolds Averaged Navier-Stokes

SGS Subgrid-scale

Chapter 1

Introduction

1.1 Motivation

Numerical modeling used to obtain a mathematical solution has become a popular methodology in industry for product development and technology advancement because significant improvements in computing systems have made this methodology particularly well suited to solving complex engineering problems. Numerical modeling used to solve fluid flow problems is known as Computational Fluid Dynamics (CFD). According to the Reynolds number, fluid flows can be divided into three different categories: laminar, transitional, and turbulent. In reality, most fluid flows are turbulent. Turbulence is one of the most difficult problems in physics and has no exact solution. CFD provides numerical and approximate solutions for turbulent fluid flow problems. There are three major methods for solving turbulent flows: Direct Numerical Simulation (DNS), Reynolds-Averaged Navier Stokes (RANS), and Large Eddy Simulation (LES). DNS is computationally expensive and still not suitable for complicated geometries. It also provides excessive information, not all of which is necessary for solving industrial problems. RANS is a more practical approach for industry but requires realistic turbulence models. LES is a compromise between DNS and RANS and is especially applicable to complex flows with significant unsteady features.

LES is a tool for analyzing relatively complex turbulent flows; however, it only resolves large-scale motions. LES requires a model to capture the effects of small-scale motions. This model type

is known as the subgrid-scale (SGS) model. Smagorinsky (1963) proposed a SGS model by assuming a linear relationship between the unresolved stress tensor and the local velocity gradient tensor. In this model formulation, the model coefficient needs to be adjusted according to the specific geometry and flow conditions; as well, explicit damping functions are used for near-wall regions. A significant improvement to this model was the implementation of the so-called dynamic procedure (Germano *et al.*, 1991), whereby the model coefficient is computed dynamically at each point and time via a double filtering procedure in physical space. The dynamic Smagorinsky model (DSM) is arguably the most popular SGS model, but it requires stabilizing techniques to control numerical instability. The Dynamic Nonlinear Model (DNM) has two main advantages over the DSM: stability and grid dependence. The current study shows that the stabilization mechanism negatively affects the ability of the DSM to predict the smallest scale motions. The Dynamic Nonlinear Model (DNM) of Wang and Bergstrom (2005) is a dynamic SGS model formulation that adopts a quadratic nonlinear relationship between the SGS tensor and local velocity gradient tensor. In comparison to the DSM, the DNM does not use a smoothing mechanism. Furthermore, for the same grid, the DNM predicts a noticeably finer-scale structure than the DSM, which positively influences the results of time-averaged and instantaneous velocity and vorticity fields.

Most SGS models, including the dynamic formulations noted above, were originally developed for plane channel flows. Their performance in more complex flows has not been as thoroughly investigated. In this work, flow over a wall-mounted finite-height square prism (also referred to in the literature as a square cylinder) is used to assess the performance of the two SGS models. This flow is rich in terms of the complexity of the flow structures because it is strongly three-dimensional, with turbulent and large-scale unsteady motions. Figure 1.1 shows a generic schematic of this flow in terms of the mean flow structure. The flow over the top of the prism interacts with the flow along the ground plane to create a complicated wake structure. The near-wake structure is dominated by the shear layers being shed from the two sides and top wall of the prism. The near-wake is formed from the interactions of the bottom, sides, and top vortices (Wang *et al.* 2004). There are three main zones based on structures: the free-end, which is the location of the tip vortices; the junction (the intersection of the prism and base plate), which is the location of
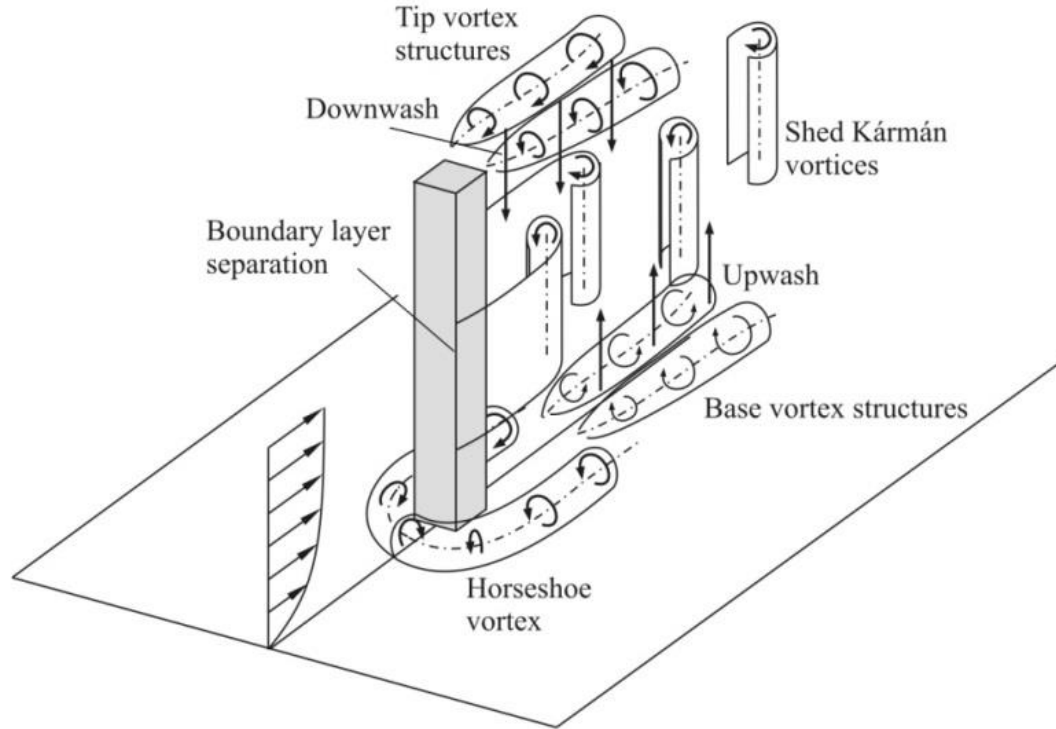
Figure 1.1. Schematic of flow over a finite-height square prism (McClean and Sumner 2014).

the base and horseshoe vortices; and the spanwise vortices at the sides (Wang 2006 and Bourgeois *et al.* 2013). The mean vorticity field in the wake is characterized by one or two pairs of counter-rotating streamwise vortex tubes. The dipole wake is one pair of vortices formed close to the obstacle free-end. The dipole wake, together with another pair of vortices close to the wall junction, is known as the quadrupole wake. The quadrupole wake is created mostly for a relatively high-aspect ratio. Also, the dipole wake occurs for a thin boundary layer, but a thick boundary layer has more potential to form a quadrupole wake (Bourgeois *et al.* 2013 and Hosseini *et al.* 2013). Time-averaged velocity streamlines and vorticity contours on the symmetry plane show a large recirculation behind and close to the free-end and also a secondary recirculation, significantly weaker, behind and at the bottom of the prism (Rostamy *et al.* 2012). A saddle point, characterized by the convergence of four streamlines at one location in a two-dimensional flow, is often present

in the vertical mid-plane of the wake. The boundary layer thickness could be a major contributor to the creation of this saddle point (El Hassan *et al*. 2015).

In addition, a periodic component is associated with this flow (Bourgeois *et al.*, 2011). There is a quasi-periodic behavior in this flow that is formed by a dominant shedding frequency. The Strouhal number (St), a dimensionless number describing periodic flow mechanisms (it gives the ratio of inertial forces caused by flow unsteadiness to the inertial forces caused by velocity variation), shows vortex shedding frequency based on characteristic length and flow velocity. Vortex shedding frequency depends on the Reynolds number, aspect ratio, boundary layer thickness and other parameters, such as the inflow velocity profile and turbulence intensity (Dousset and Potherat 2010, Vinuesa et al. 2015, Bourgeois et al. 2013, Hosseini et al. 2013, Saeedi and Wang 2016). The frequency of this shedding behavior is increased by the aspect ratio. Sometimes there is more than one peak dominating shedding frequency (McClean and Sumner, 2014).

To investigate this flow feature, the phase-averaging methodology was used in this study. Phase-averaging is based on the dominant frequency of a periodic unsteady flow. Phase-averaging based on the Strouhal number reveals a wake structure with quasi-periodic features that is much different from the mean vorticity field. Phase-averaged data capture flow structures, such as shedding vortices and half-loop structures, that are removed in time-averaging (Bourgeois *et al*. 2011 and Sattari *et al.* 2012). A half-loop structure consists of a vertical leg and an approximate streamwise connector strand.

One of the challenges of SGS models relates to backscatter and numerical stability. Backscatter refers to the physically observed process of energy transfer from small scale to large scale. To capture energy transfer, SGS models that use an eddy viscosity model formulation should allow the value of the instantaneous SGS viscosity to become either negative or positive. However, in practice, the SGS-DSM model can become locally unstable for a negative SGS viscosity. When instability occurs, the model requires a stabilizing technique that increases the robustness and also eliminates the potential for local backscatter.

1.2 Objectives and Scope

The main goal of this research was to use LES with two different SGS models to predict the flow structure over a finite-height square prism mounted normally on a ground plane. The aspect ratio (AR = H/D, where H is the cylinder height and D is the cylinder width) was AR = 3, the Reynolds number based on the prism width and freestream velocity was Re = 500, and the inflow was laminar with a relatively thin boundary layer on the ground plane of $\delta/D \approx 0.2$ (where δ is the boundary layer thickness). Two DNS studies (Saha 2013 and Zhang *et al*. 2017) were available for comparison. They indicate that this flow configuration is characterized by quasi-periodic behavior, vortex shedding structures, and large-scale unsteady motions.

This thesis considers the following principal objectives:

> 1.2.1 To compare and assess the performance of two different dynamic SGS models, i.e. a linear and nonlinear model formulation, in predicting the flow over a finite-height prism, with respect to both the flow structure and SGS energy transfer;

> 1.2.2 To use the preferred SGS model to perform an LES of the finite-height prism flow and implement phase-averaging to study the large-scale motions in the near-wake.

To achieve the above objectives, the thesis was completed in three main studies:

The first study describes the implementation of LES using a dynamic subgrid-scale model to predict flow over a wall-mounted finite-height square prism. The purpose, a pre-objective of this thesis, was to evaluate the potential of LES to capture the large unsteady scales of motion associated with this type of flow. The filtered continuity and Navier-Stokes equations were discretized on a relatively coarse grid using the finite-volume method. The discrete form of the continuity and momentum equations were solved using a second-order fractional-step method. Phase-averaging was used to study the large-scale, periodic features of the near-wake.

The second study describes the application of two different dynamic subgrid-scale models for the same flow configuration but a much finer grid. Both linear and nonlinear dynamic subgrid-scale model formulations were implemented and tested for their ability to resolve the complex wake structure associated with this flow. The time-averaged and instantaneous flow fields were compared, including resolved velocity, vorticity, and turbulence kinetic energy dissipation (SGS, resolved, and total scales).

The third study describes the use of DNM with LES to predict the flow structure. To better understand the underlying flow mechanisms and structure, advanced visualization techniques were implemented. The frequency of the flow periodicity was used to perform phase-averaging. The phase-averaged behavior was studied for five cycles and five phases, and the second invariant of the velocity gradient tensor was used to visualize the vortex structures.

1.3 The Expected Contributions

In the context of achieving the objectives outlined above, the thesis research will make the following contributions:

1.3.1 Perform an LES of the flow over a square prism for an aspect ratio AR = 3 and a Reynolds number of Re = 500 for the two different SGS models being considered, i.e. the DSM and the DNM. The quality of the LES calculations will be assessed in terms of the grid resolution and using comparison of flow structures to other low Reynolds number results in the literature.

1.3.2 The main features of the mean and instantaneous velocity fields will be comprehensively explored for both SGS models. The analysis will include multiple kinematic approaches, i.e. streamlines and vorticity contours, as well as both two-dimensional (2D) and three-dimensional (3D) visualizations of the vorticity fields. The analysis of the predicted velocity fields will especially focus on any significant differences due to the use of different SGS models. The predictions of the SGS models for one important SGS stress component will also be documented.

1.3.3 An important contribution of the present study is to analyze the dissipation of turbulence kinetic energy which consists of a resolved-scale contribution, as well as the so-called SGS dissipation of turbulence kinetic energy. The latter quantity represents a kinetic energy flux from the resolved-scale to the SGS motions. The dissipation features associated with each SGS model will be investigated, which are closely related to the prediction for the smallest resolved-scale motions by the LES.

1.3.4 Since the finite-height prism flow includes large-scale unsteady motions, the present study will perform a phase-averaged decomposition of the flow in the near-wake for both SGS models. The dominant characteristics of the phase-average flow field will be examined over one cycle. This analysis will be helpful for understanding the vortex shedding structures, and the anticipated development of half-loop structures farther downstream. It will seek to answer the important question as to how the initially spanwise (vertical) cores shed from the downstream edges of the prism realign to form vortex tubes aligned in the streamwise direction.

A preliminary investigation of the effect of SGS model was performed by Einian (2012) for an aspect ratio of AR = 5 and Reynolds number of Re = 500. She looked at the impact of different SGS models on the time-averaged and instantaneous flow fields, as well as the resolved-scale stresses. The major and distinct contributions of the current study include: use of a smaller aspect ratio prism; analysis and assessment of the grid using the Kolmogorov length scale; use of the phase-averaging method to analyze the periodic behavior; exploration of the energy transfer to the SGS motions, as well as the resolved-scale and total dissipation of turbulence kinetic energy; an in-depth comparison and assessment of the effect of using two different dynamic SGS models.

The present thesis research was based on the use of an in-house LES code written in FORTRAN. The numerical methodology used in this code was verified in previous versions of the code that were applied to the prediction of fully developed turbulent channel flow. Comparisons against DNS and experimental results verified the performance of the numerical solver and LES models. Earlier versions of this code were also used to simulate flow over a finite height square prism of

aspect ratio AR = 5 (Einian, 2012), as well as flow over a two-dimensional square prism in proximity to a wall (Samani, 2014). These two theses made extensive comparisons with experimental and other numerical results that further demonstrated the accuracy of the numerical solver and SGS models, in the context of unsteady flows.

1.4 Literature Review

This section is divided into two main themes related to the objectives of this study. The first theme concerns the background and application of SGS models in predicting complex flows, and the second reviews the flow over a finite-height square prism mounted on a ground plane.

1.4.1 SGS Models

In a turbulent flow, kinetic energy typically transfers from large scale to small scale, but, according to observations of the instantaneous velocity field, energy can also be transferred from small scale to large scale. This latter phenomenon is known as backscatter (Meneveau and Katz, 2000). To capture backscatter in LES, an SGS model, which uses an eddy viscosity formulation, needs to allow the local instantaneous SGS viscosity to become negative. As previously discussed, a dynamic procedure can be added to a SGS model to automatically adjust the model coefficient dynamically in time and space. Often, the application of a dynamic procedure to a Smagorinsky model causes negative values of the SGS viscosity. Since these large negative values can cause computational instability, a stabilization mechanism is required, such as plane averaging and/or a clipping function to control the computational stability (Baya Toda *et al.* 2014). These stabilizing techniques often effectively remove the feature of local backscatter. A DNM formulation that adopts a quadratic nonlinear relationship between the SGS stress tensor and local velocity gradient tensor was proposed by Wang and Bergstrom (2005). Compared to other SGS models, this DNM adopts a much more comprehensive coupling of the subgrid-scale stress to the resolved velocity gradient field. It also has the advantage of being able to predict backscatter in a locally robust manner without any need for plane averaging or other stabilization techniques.

Sohankar *et al.* (1999) compared different SGS models in LES of flow over a square prism. As models have been refined, improvements have been made, so that the dynamic one-equation model

is generally considered to be superior to the dynamic Smagorinsky model, which, in turn, is superior to the standard Smagorinsky model (Sohankar *et al.* 1999). In the evaluation of these SGS models, predicted flow structures have been assessed against experimental data. The dynamic one-equation model has predicted results that are closer to the experimental data. The dynamic one-equation model has one other major advantage over the dynamic Smagorinsky model: it does not require clipping or averaging for the dynamic coefficient and for stability to be maintained.

Both the DSM and the scale-invariant dynamic SGS models were used in LES by Basu and Porté-Agel (2006) to simulate the atmospheric boundary layer (ABL). The results of both models were evaluated versus experimental data. The results were realistic in terms of the mean flow prediction. However, both SGS models exhibited stability issues and required a stabilization function to prevent values of the SGS viscosity from causing convergence problems.

Stabilization mechanisms artificially constrain the SGS model coefficient. Meneveau *et al.* (1996) used a dynamic Smagorinsky SGS viscosity model for LES. This model's results showed negative SGS viscosity, which caused computational stability issues. In this study, the authors introduced a stabilization mechanism applicable for in-homogeneous flows in complex geometries, where plane averaging was not feasible. Whereas existing formulations artificially constrained the model coefficient to be positive, this formulation did not constrain the SGS viscosity to be only positive. This approach implemented an averaging function over the flow pathlines. In similar research, Tran and Sahni (2017) compared the outcomes for LES of inhomogeneous channel flows using a combination of the residual-based variational multiscale (RBVMS) approach and the dynamic Smagorinsky eddy-viscosity model for turbulent flow over a cylinder (Re = 3900) and found the same stabilization problem. In another study in this category, Lee and Cant (2017) compared the performances of DSM and the Smagorinsky model. They assessed the results against experimental data for flow over a bluff body and found good agreement in general but underprediction of the inner shear layer. These studies show that the dynamic Smagorinsky model predicts essential flow features but has stabilization problems.

Other studies have demonstrated the weaknesses of the DSM. An LES study by Bopape *et al.* (2016) showed the deficiencies of the DSM when used with a relatively low grid resolution, which was especially significant for small scale structures. In another study, Khani and Waite (2015)

showed that the DSM needed approximately half of the grid resolution required by the traditional Smagorinsky model to predict a similar flow pattern. To predict the flow structures near the walls, the DSM needed a high-grid resolution. The DSM also required an averaging methodology with a clipping function to control the computational stability issue caused by large values of SGS viscosity.

Heinz *et al.* (2015) and Heinz and Gopalan (2012) compared a realizable linear dynamic model (LDM) and a realizable nonlinear dynamic model (NDM) to the DSM and DNM. They found that the LDM and NDM predicted backscatter and small-scale structures without any stability issues, and were computationally more efficient than the DNM and DSM. However, in earlier research Heinz (2008) noted that the DSM has a stability issue due to uncontrolled fluctuations, which he related to an incorrect scale dependence.

1.4.2 Finite Square Prism Flow

The flow over the top of a finite-height square prism interacts with the flow along the ground plane to create a complicated wake structure. The near-wake structure is dominated by shear layers being shed from the two sides and top wall of the prism. The near-wake is formed from the interactions of vortices shed from the bottom, sides, and top of the prism (Wang *et al.* 2004). There are three main zones based on the flow structure: 1) the free-end, which is the location of the tip vortices; 2) the junction (or intersection of the prism and ground plane), which is the location of the base and horseshoe vortices; and 3) the prism sidewalls, which shed spanwise vorticity (Wang 2006 and Bourgeois *et al.* 2013).

There are two types of vortex shedding patterns behind an obstacle mounted on a surface: antisymmetric and symmetric (Wang and Zhou, 2009). Anti symmetric shedding is formed around prisms with higher aspect ratios, whereas symmetrical shedding (which is almost symmetrical) occurs with shorter obstacles. There are also flows with a combination of these two shedding patterns (Sakamoto and Arie, 1983). The structure of vortex shedding also depends on the Reynolds number (Saha *et al*. 2003). Zhang *et al.* (2017) performed a direct numerical simulation (DNS) of the flow over a finite prism with the aspect ratio AR = 4 for a Reynolds number ranging from 50 to 1000 and found the periodic frequency increased with the Reynolds number. Similarly,

Saha (2013) used DNS to investigate the effect of the aspect ratio (AR = 2, 3, 4, and 5) on a finite prism flow at a Reynolds number of Re = 250 and found the Strouhal number increased for higher aspect ratios.

The mean vorticity field in the wake is characterized by one or two pairs of counter-rotating streamwise vortex tubes. A dipole wake refers to one pair of vortices formed close to the obstacle free-end. When there is a second pair of vortices close to the ground plane, the flow pattern is known as a quadrupole wake. The quadrupole wake is typically observed for flows with relatively high-aspect ratios and thick boundary layers, whereas the dipole wake is associated with thin boundary layers (Bourgeois *et al*. 2013 and Hosseini *et al.* 2013). Time-averaged streamlines and vorticity contours on the symmetry plane show a large recirculation zone behind and close to the free-end, with a secondary recirculation zone, significantly weaker, behind and close to the ground plane (Rostamy *et al*. 2012). The streamlines in the mid-plane typically form a saddle point associated with the interaction between the upwash and downwash velocity fields. This saddle point requires a sufficiently tall prism to create a quadrupole wake. The boundary layer thickness may also affect the formation of a saddle point (El Hassan *et al*. 2015).

Phase-averaging based on the Strouhal number reveals a wake structure with quasi-periodic features that is much different from the mean velocity field. Phase-averaging captures flow structures that are removed by time-averaging, such as vortex cores shed from the sides of the prism and half-loop structures that develop further downstream (Bourgeois et al. 2011 and Sattari et al. 2012). A half-loop structure is a vortex tube that consists of a vertical leg and an approximate streamwise connector strand.

Within the same research group, a LES study of flow over a finite-height square prism mounted on a ground plane with an aspect ratio of AR = 5 and Reynolds number of Re = 500 was previously performed by Einian (2012). In her research, the boundary layer thickness was relatively thin and laminar with $\delta/D = 0.3$. The thesis consisted of three main parts: investigation of the time-averaged and instantaneous flow fields including use of the second invariant to visualise the 3D flow structure; comparing the results for two dynamic SGS models (DSM and DNM) for two grids with lower and higher resolution; and exploring the effect of aspect ratio (AR = 3, 5 and 7) on the flow

structure and aerodynamic forces. The predicted time-averaged results showed reasonable agreement with the experimental data of Wang *et al.* (2006) at a much higher Reynolds number.

1.5 Thesis Outline

This manuscript-based thesis includes five chapters, each having an individual abstract, introduction, methodology, geometry, results, discussion, conclusion, and references. Each chapter's figures are collected together at the end of the chapter.

The first chapter (the current one) is a general introduction to the thesis, describing the motivation, objectives, and contributions and containing the literature review, outlines of chapters, and references.

The second chapter reports a LES using a dynamic Smagorinsky model to evaluate the potential of LES to capture the large unsteady scales of motion for a finite-height prism wake using a relatively coarse grid.

The third chapter investigates dynamic SGS models for large eddy simulation and reports the results of the application of two different dynamic subgrid-scale models. Both linear and nonlinear dynamic subgrid-scale model formulations are implemented and tested for their ability to resolve the complex wake structure associated with this flow.

The fourth chapter reports a large eddy simulation using a dynamic nonlinear subgrid-scale model and focusing on phase-averaging and dominant frequency.

The fifth chapter presents conclusions and contributions along with recommendations for future work.

1.6 References

Basu, S. and Porté-Agel, F. (2006). Large-eddy simulation of stably stratified atmospheric boundary layer turbulence: a scale-dependent dynamic modeling approach. *Journal of the Atmospheric Sciences, 63*, 2074-2091. DOI: 10.1175/JAS3734.1

Baya Toda, H., Cabrit, O., Truffin, K., Bruneaux, G., and Nicoud, F. (2014). Assessment of subgrid-scale models with a large-eddy simulation-dedicated experimental database: The pulsatile impinging jet in turbulent cross-flow. *Physics of Fluids, 26* (7), 075108. DOI: 10.1063/1.4890855

Bopape, M. J. M., Plant, R. S., and Coceal, O. (2016). Simulating the convective boundary layer with a dynamic Smagorinsky model. *32nd Annual Conference of the South African Society for Atmospheric Sciences,* 11-15. University of Cape Town, South Africa, October 31 - November 1, 2016.

Bourgeois, J. A., Noack, B. R., and Martinuzzi R. J. (2013). Generalized phase-average with applications to sensor-based flow estimation of the wall-mounted square cylinder wake. *Journal of Fluid Mechanics, 736*, 316-350. DOI: 10.1017/jfm.2013.494

Bourgeois, J. A., Sattari, P., and Martinuzzi, R. J. (2011). Alternating half-loop shedding in the turbulent wake of a finite surface-mounted square cylinder with a thin boundary layer. *Physics of Fluids, 23* (9), 095101. DOI: 10.1063/1.3623463

Dousset, V. and Pothérat, A. (2010). Formation mechanism of hairpin vortices in the wake of a truncated square cylinder in a duct. *Journal of Fluid Mechanics, 653*, 519-36. DOI: 10.1017/S002211201000073X

Einian, M. (2012). Large eddy simulation of flow around a finite square prism, Doctoral dissertation at University of Saskatchewan, Saskatoon, SK, Canada.

El Hassan, M., Bourgeois, J. A., and Martinuzzi, R. J. (2015). Boundary layer effect on the vortex shedding of wall mounted rectangular prism. *Experiments in Fluids, 56* (33), 1-19. DOI: 10.1007/s00348-014-1882-6

Germano, M., Piomelli, U., Moin, P., and Cabot, W. H. (1991). A dynamic subgrid-scale eddy viscosity model. *Physics of Fluids A: Fluid Dynamics, 3* (7), 1760-1765. DOI: 10.1063/1.857955

Heinz, S. (2008). Realizability of dynamic subgrid-scale stress models via stochastic analysis. *Monte Carlo Methods and Applications, 14* (4), 311-329. DOI: 10.1515/MCMA.2008.014

Heinz, S. and Gopalan, H. (2012). Realizable versus non-realizable dynamic subgrid-scale stress models. *Physics of Fluids, 24*, 115105. DOI: 10.1063/1.4767538

Heinz, S., Gopalan, H., Foroushani, E. K., Stoellinger, M. K., Mokhtarpoor, R., and Balakumar, P. (2015). Realizable dynamic LES subgrid-scale modeling. Proceedings of *9th International Symposium on Turbulence and Shear Flow Phenomena (TSFP-9).* Melbourne, Australia, June 30 - July 3, 2015.

Hosseini, Z., Bourgeois, J. A., and Martinuzzi, R. J. (2013). Large-scale structures in dipole and quadrupole wakes of a wall-mounted finite rectangular cylinder. *Experiments in Fluids, 54* (9), 1595.

Khani, S. and Waite, M. L. (2015). Large eddy simulations of stratified turbulence: the dynamic Smagorinsky model. *Journal of Fluid Mechanics, 773*, 327-344. DOI: 10.1017/jfm.2015.249

Lee, C. Y. and Cant, S. (2017). Assessment of LES subgrid-scale models and investigation of hydrodynamic behaviour for an axisymmetrical bluff body flow. *Flow, Turbulence and Combustion*, *98* (1), 155-176. DOI: 10.1007/s10494-016-9751-4

McClean, J. F. and Sumner, D. (2014). An experimental investigation of aspect ratio and incidence angle effects for the flow around surface-mounted finite-height square prisms. *Transactions of the ASME: Journal of Fluids Engineering, 136* (8), 081206. DOI: 10.1115/1.4027138

Meneveau, C. and Katz, J. (2000). Scale-invariance and turbulence models for large eddy simulation. *Annual Review of Fluid Mechanics, 32*, 1-32. DOI: 10.1146/annurev.fluid.32.1.1

Meneveau, C., Lund, T. S., and Cabot, W. H. (1996). A Lagrangian dynamic subgrid-scale model of turbulence. *Journal of Fluid Mechanics, 319*, 353-385. DOI: 10.1017/S0022112096007379

Rostamy, N., McClean, J. F., Sumner, D., Bergstrom, D. J., and Bugg, J. D. (2012). Local flow field of a surface–mounted finite square prism. *7th International Colloquium on Bluff Body Aerodynamics and Applications (BBAA7)*. Shanghai, China, September 2-6, 2012.

Saeedi, M. and Wang, B. C. (2016). Large-eddy simulation of turbulent flow around a finite-height wall-mounted square prism within a thin boundary layer. *Flow, Turbulence and Combustion*, *97* (2), 513-538. DOI: 10.1007/s10494-015-9700-7

Saha, A. K. (2013). Unsteady flow past a finite square prism mounted on a wall at low Reynolds number. *Computers and Fluids, 88*, 599-615. DOI: 10.1016/j.compfluid.2013.10.010

Saha, A. K., Biswas, G., and Muralidhar, K. (2003). Three-dimensional study of flow past a square cylinder at low Reynolds numbers. *International Journal of Heat and Fluid Flow, 24* (1), 54-66. DOI: 10.1016/S0142-727X(02)00208-4

Sakamoto, H. and Arie, M. (1983). Vortex shedding from a rectangular prism and a circular prism placed vertically in a turbulent boundary layer. *Journal of Fluid Mechanics, 126*, 147-165. DOI: 10.1017/S0022112083000087

Sattari, P., Bourgeois, J. A., and Martinuzzi, R. J. (2012). On the vortex dynamics in the wake of a finite surface-mounted square prism. *Experiments in Fluids, 52* (5), 1149-1167. DOI: 10.1007/s00348-011-1244-6

Smagorinsky, J. (1963). General circulation experiments with the primitive equations: I. The basic experiment, *Monthly Weather Review, 91*, 99-164. DOI: 10.1175/1520-0493(1963)091<0099:GCEWTP>2.3.CO;2

Sohankar, A., Davidson, L., and Norberg, C. (1999). Large eddy simulation of flow past a square cylinder: Comparison of different subgrid scale models. *Transactions of the ASME: Journal of Fluids Engineering, 122* (1), 39-47. DOI: 10.1115/1.483224

Tran, S. and Sahni, O. (2017). Finite element-based large eddy simulation using a combination of the variational multiscale method and the dynamic Smagorinsky model. *Journal of Turbulence, 18* (5), 391-417. DOI: 10.1080/14685248.2017.1280607

Vinuesa, R., Schlatter, P., Malm, J., Mavriplis, C., and Henningson, D. S. (2015). Direct numerical simulation of the flow around a wall-mounted square cylinder under various inflow conditions. *Journal of Turbulence, 16* (6), 555-587. DOI: 10.1080/14685248.2014.989232

Wang, B. C. and Bergstrom, D. J. (2005). A dynamic nonlinear subgrid-scale stress model. *Physics of Fluids, 17 (3)*, 035109. DOI: 10.1063/1.1858511

Wang, H. F. (2006). Effect of initial conditions on interaction between a boundary layer and a wall-mounted finite-length-cylinder wake. *Physics of Fluids, 18* (6), 065106. DOI: 10.1063/1.2212329

Wang, H. F. and Zhou, Y. (2009). The finite-length square cylinder near-wake. *Journal of Fluid Mechanics, 638*, 453-490. DOI: 10.1017/S0022112009990693

Wang, H. F., Zhou, Y., Chan, C. K., Wong W. O., and Lam K. S. (2004). Flow structure around a finite-length square prism. Proceedings of *15th Australasian Fluid Mechanics Conference*. The University of Sydney, Sydney, Australia, December 13-17, 2004.

Zhang, D., Cheng, L., An, H., and Zhao, M. (2017). Direct numerical simulation of flow around a surface-mounted finite square cylinder at low Reynolds number. *Physics of Fluids, 29* (4), 045101. DOI: 10.1063/1.4979479

Chapter 2

Large Eddy Simulation of Phase-Averaged and Mean Structures in the Wake of a Finite Square Prism as Predicted by Dynamic Smagorinsky Model

Preamble

The purpose of this chapter is to implement large eddy simulation (LES) using a dynamic subgrid-scale model to predict flow over a wall-mounted finite-height square prism. Evaluating the potential of LES to capture the large unsteady scales of motion associated with this type of flow is a pre-objective of this thesis.

The aspect ratio of the prism is 3 (AR = H/D, where H is the cylinder height and D is the cylinder width), and the Reynolds number based on the cylinder width and freestream velocity is 500. The inflow is laminar with a boundary layer that is relatively thin $\delta/D \approx 0.2$, where δ is the boundary layer thickness.

The current chapter forms part of the first contribution of the thesis (described in Section 1.3.1), which is to evaluate the potential of LES code to capture the main structures associated with this type of flow.

The solution method is based on Large Eddy Simulation and a dynamic Smagorinsky model (DSM) for the SGS stress. The grid is relatively coarse (1/8 final grid) in order to reduce the time required for phase-averaging. The flow over the top of the cylinder interacts with the flow along the ground plane to create a complicated wake structure. The near-wake structure is dominated by the shear layers being shed from the two sides and top wall of the cylinder. The wake is characterized by a velocity field that changes rapidly in both direction and magnitude. Phase-averaging based on the Strouhal number reveals a wake structure with quasi-periodic features that is much different from the mean vorticity field.

Abstract

This paper reports a Large Eddy Simulation of turbulent flow over a finite-height square prism mounted normal to a ground plane. The prism aspect ratio is AR = 3 and the Reynolds number based on the prism width and freestream velocity is Re = 500. The cylinder is immersed in a uniform freestream flow, which creates a thin laminar boundary layer on the ground plane: $\delta/D \approx$ 0.2 (δ is the boundary layer thickness and D is the cylinder width. The flow over the top of the cylinder interacts with the flow along the ground plane to create a complicated wake structure. The near-wake structure is dominated by the shear layers being shed from the two sides and top wall of the cylinder. The wake is characterised by a velocity field that changes rapidly in both direction and magnitude. The mean vorticity field in the wake is characterised by two pairs of counter-rotating streamwise vortex tubes. Phase-averaging based on the Strouhal number reveals a wake structure with quasi-periodic features (such as half-loop structure) that is much different than the mean vorticity field.

2.1 Introduction

Turbulent flow over external bodies characterized by shear layer separation is complex, and is often marked by both large-scale periodic motions such as vortex shedding, as well as smaller-scale motions associated with the fluid turbulence. To predict the aerodynamic forces on a bluff body, as well as transport behaviour downstream, the instantaneous and mean structure of the wake need to be understood. In this paper we focus on the special case of a square prism, which is finite in height and mounted perpendicular to a ground plane. An important characteristic of such flows is the aspect ratio AR = H/D (where H is the height and D is the width of the prism), which can be regarded as a measure of the slenderness of the prism. For a finite-height prism, the wake is strongly influenced by both the tip vortex structures which develop at the free end of the cylinder, as well as the boundary layer developing on the ground plane. Wang and Zhou (2009) studied the flow over a square prism and observed both asymmetric and symmetric shedding; they also postulated a model for the structure of the time-averaged wake. In contrast, Bourgeois et al. (2011) concluded that the wake structure should be understood in terms of the phase-averaged behaviour;

20

for the case of a square prism of AR = 4, they identified a so-called half-loop structure, which consists of two vortex tube segments aligned primarily in the vertical and streamwise directions.

The present paper reports on a Large Eddy Simulation (LES) of a low Reynolds number (Re = U D/ν = 500 , where U is the freestream velocity and ν is the kinematic viscosity) flow over a square prism of aspect ratio AR = 3 mounted on a ground plane. The boundary layer on the ground plane is thin and laminar: $\delta/D \approx 0.2$ where δ is the boundary layer thickness. Two and three-dimensional visualisations of the mean and phase-averaged flow structures are used to investigate the flow dynamics. Of special interest is the mechanism whereby the shear layers being shed from the vertical sides of the cylinder are modified to form vortex structures with a streamwise orientation. It confirms the presence of quasi-periodic vortical structures, which is surprising at this low aspect ratio.

2.2 Solution Method

The mathematical model consisting of the filtered Navier-Stokes equations was discretised using the finite-volume method. A localized dynamic Smagorinsky model (DSM) was used to represent the subgrid-scale (SGS) stresses. The resultant equation set was solved using a fractional step method, where the convective and diffusive terms were formulated using the Crank-Nicolson method. A multi-grid (MG) method was used to efficiently solve pressure correction field. The initial velocity field was first developed in time to obtain realistic flow behaviour. Thereafter, velocity data were collected to obtain time and phase-averaged values, to supplement the instantaneous velocity fields.

In terms of boundary conditions, the surfaces on the ground plane and prism were modeled as no-slip impermeable walls. The side and top surfaces were modeled as free-slip walls. The velocity profile specified at the inlet plane was uniform laminar flow with a thin boundary layer region of thickness $\delta/D = 0.01$. The outlet uses a convective boundary condition.

For phase-averaging, the Strouhal number, determined from multiple time traces of the velocity field within the wake, was used to estimate the period of the vortex shedding. The time period

associated with one complete cycle was divided into five smaller phase periods or bins. The velocity field in the wake was time-averaged over each phase of the cycle, and the result stored in that bin. At the end of one periodic cycle, five phase bins were collected, each of which contained the velocity field averaged over the phase period. The velocity field in each bin can be considered indicative of the characteristic features of the velocity field at a time in the periodic cycle corresponding to the center of the bin. This procedure was repeated five times to provide data for five complete cycles. Finally, for each phase the velocity fields in the five bins were averaged again, which resulted in the phase-average velocity field for the prism wake. As documented in the next section, phase-averaging revealed a wake structure with quasi-periodic features that is much different from the structure suggested by the mean velocity field.

2.3 Flow Description

Figure 2.1 shows the solution domain. Note that given the short upstream extent of the solution domain, the boundary layer developed on the ground place was laminar and relatively thin. The thickness at the location of the cylinder was estimated to be approximately 0.2D. The blockage of the flow associated with the cylinder was approximately 7 percent. For the present simulation, the total number of control volumes was $64 \times 72 \times 48$, in the streamwise (X), vertical (Y) and transverse (Z) directions, respectively. Horizontal, streamwise and transverse sections of the grid are shown in Figures 2.2 and 2.3 respectively. The inflow was uniform velocity and laminar. The present simulation adopted a relatively coarse grid to perform a preliminary study of this flow. The coarse grid enabled a larger time-step, which facilitated the extensive run-times required to perform the phase and time-averaging.

Prism:
H = 3D
AR= H/D=3

Domain:
L = 16D
H_1 = 6D
W = 7D
L_1 = 3D
L_2 = 12D
W_1 = 3D

Blockage ratio: 7%.

Re = 500
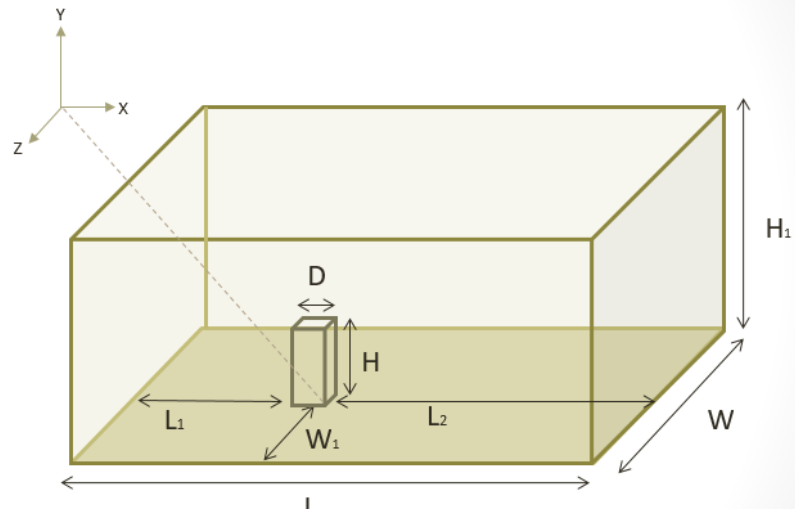
Figure 2.1. Sketch of the flow domain and prism geometry.
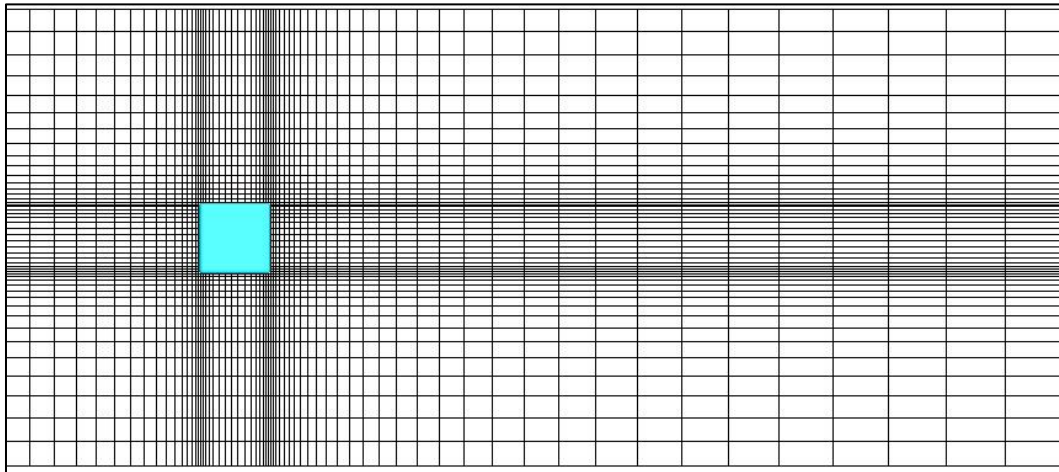
Figure 2.2. Grid section in the horizontal (X-Z) plane.
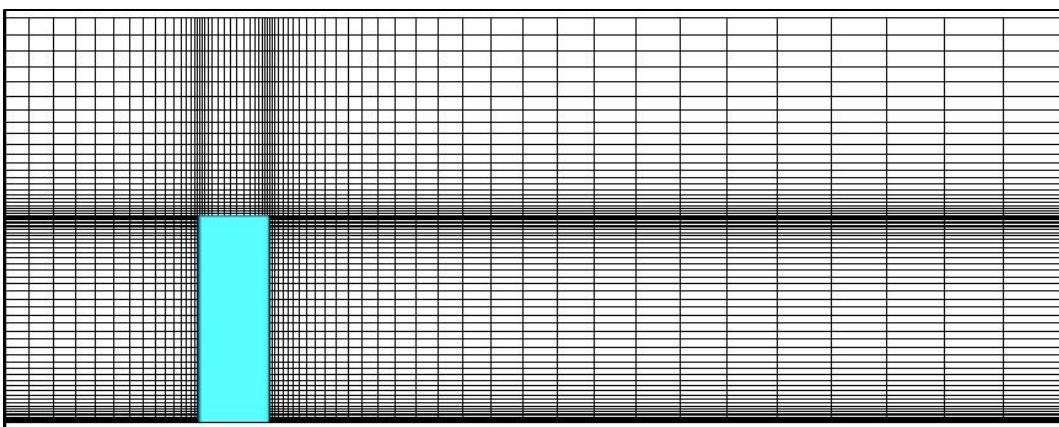
Figure 2.3. Grid section in the streamwise (X-Y) plane.

2.4 Results and Discussion

Figure 2.4a) presents the time-averaged streamlines in the vertical (X-Z) symmetry-plane of the wake, together with contours of transverse vorticity. The flow initially separates from the leading edge of the top of the prism; this shear layer does not reattach but extends into the near-wake region. Just above the top of the prism there is evidence of a small separation region with reverse flow. The near-wake region immediately downstream of the prism is characterized by a large vortex located directly behind the free end of the prism. The vortex creates a large recirculation zone in the near-wake, which includes regions of reverse flow and upward flow along the rear surface of the prism. In the lower portion of the wake just above the ground plane, the reverse flow swirls downward to form a focal point located near the base of the rear wall of the prism. The near-wake region is separated from the wake region further downstream by a dividing streamline. No strong upward flow and associated saddle point is observed, which may be due to the fact that the boundary layer is relatively thin. All of these main features are observed in an experimental study by Rostamy *et al.* (2012) for the same aspect ratio but a higher Reynolds number of Re = 4.2×10^4 in Figure 2.4b).

Figures 2.5 and 2.6 present the velocity vectors and spanwise vorticity contours for horizontal sections through the wake at two different elevations. The flow in Figure 2.5 is located at an elevation equal to 25 percent of the height of the prism. The flow pattern indicates separation from the vertical leading edges of the prism, with narrow regions of reverse flow along the sides of the prism. The near-wake region is dominated by reverse flow, with two strong vortices/recirculation zones downstream of the rear edges of the prism pumping fluid back toward the prism. The reverse flow extends for a significant distance downstream, and the streamwise momentum deficit in the wake persists for a long distance downstream of the prism.

The horizontal section shown in Figure 2.6 is located at 75 percent of the height of the prism. It is strongly affected by the downwash flow in this region of the wake. The separating shears layers from the leading edges of the prism turn back toward the wake centreline downstream of the cylinder, resulting in a wake that is narrower in transverse extent. The velocity vectors well downstream of the prism indicate that fluid in the outer region is being drawn into the wake. The
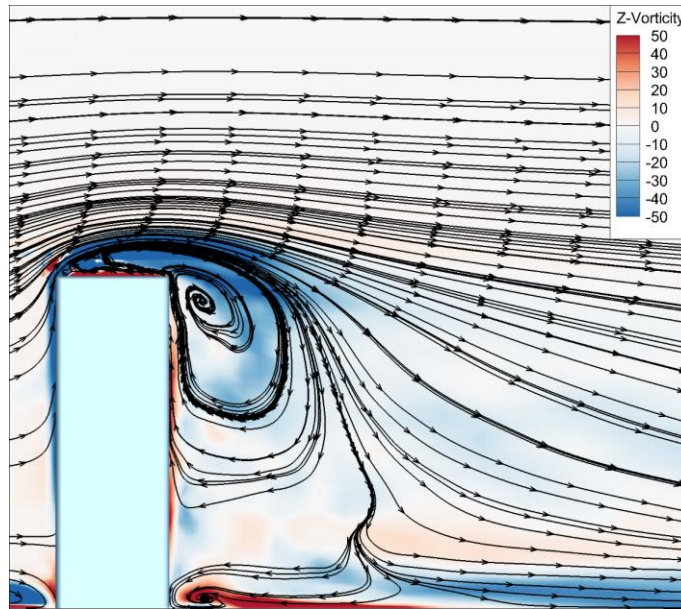
a) Current study
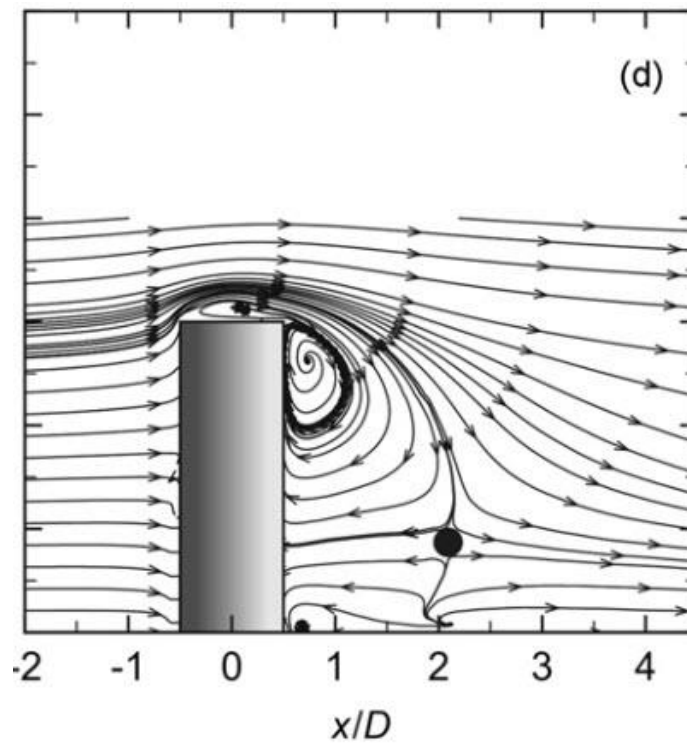
b) Rostamy *et al.* (2012).

Figure 2.4. Mean streamlines and contours of transverse vorticity in the symmetry plane.
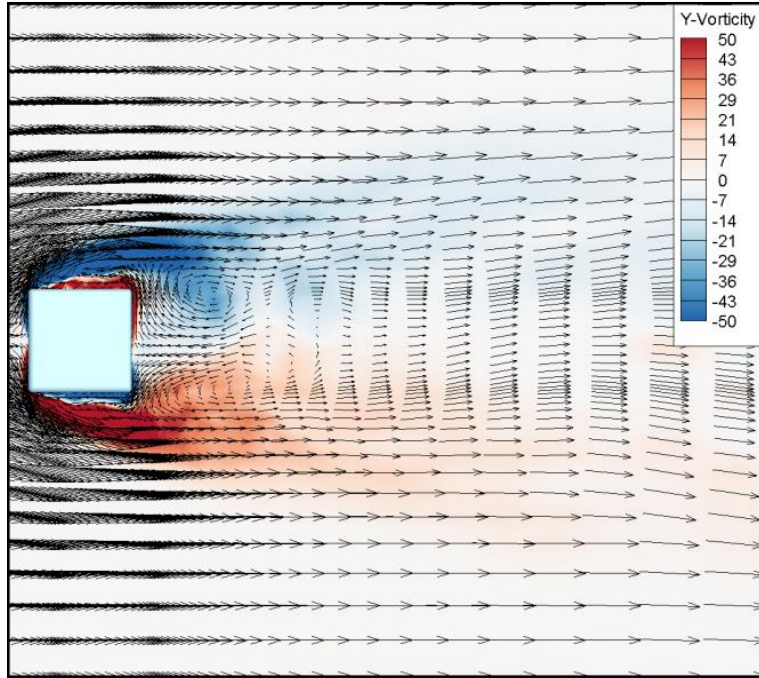
Figure 2.5. Mean velocity vectors and contours of spanwise vorticity for a horizontal section located at Y = 0.25 H.
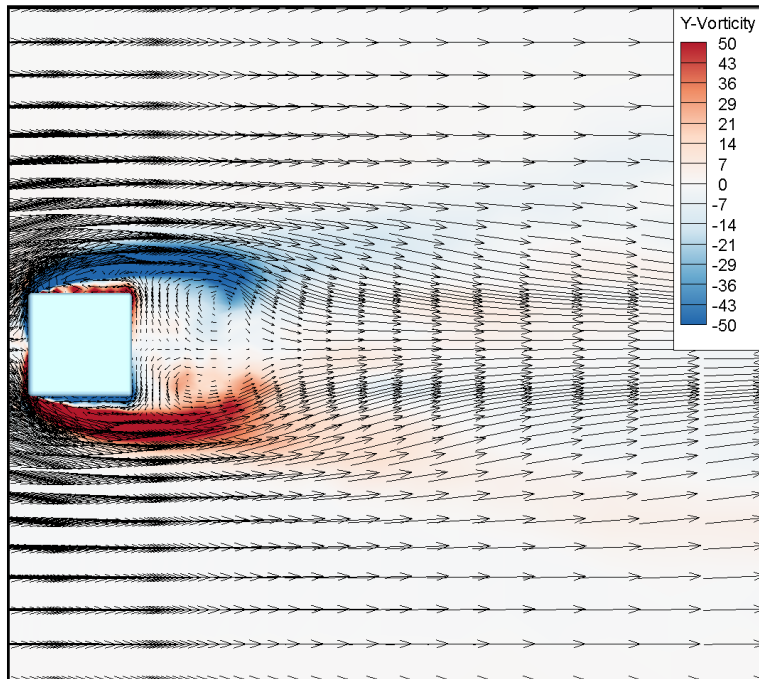
Figure 2.6. Mean velocity vectors and contours of spanwise vorticity for a horizontal section located at Y = 0.75 H.

reverse flow and associated vortices in the near-wake are weaker than those shown in Figure 2.5. The recovery of the momentum deficit along the centreline of the wake is more rapid, partly due to the downwash flow which brings high velocity fluid into this region. The mean velocity field in the wake as discussed thus far does not give any evidence of periodic behaviour, since that feature would be lost upon time-averaging.

However, when time traces of the velocity field were collected at discrete locations in the prism wake, the resulting velocity fields showed strong evidence of periodicity. Figures 2.7 shows a temporal trace of the instantaneous transverse velocity and the associated power spectra at a reference point located at $(X = 2D, Y = 3H/4, Z = D/2)$ in the cylinder wake. The velocity exhibits a strong periodic component. Examination of the power spectrum of the fluctuating velocity field indicated a single dominant peak at a frequency of $f = 2.4$ Hz corresponding to a Strouhal number $(St = fD/U)$ of $St = 0.128$. This compares to the value of approximately $St = 0.12$ calculated by Saha *et. al.* (2003) for the infinite prism case at the same Reynolds number. Based on the Strouhal number, the velocity field was phase-averaged using five phases based on data collected over five periods.

a)   b)
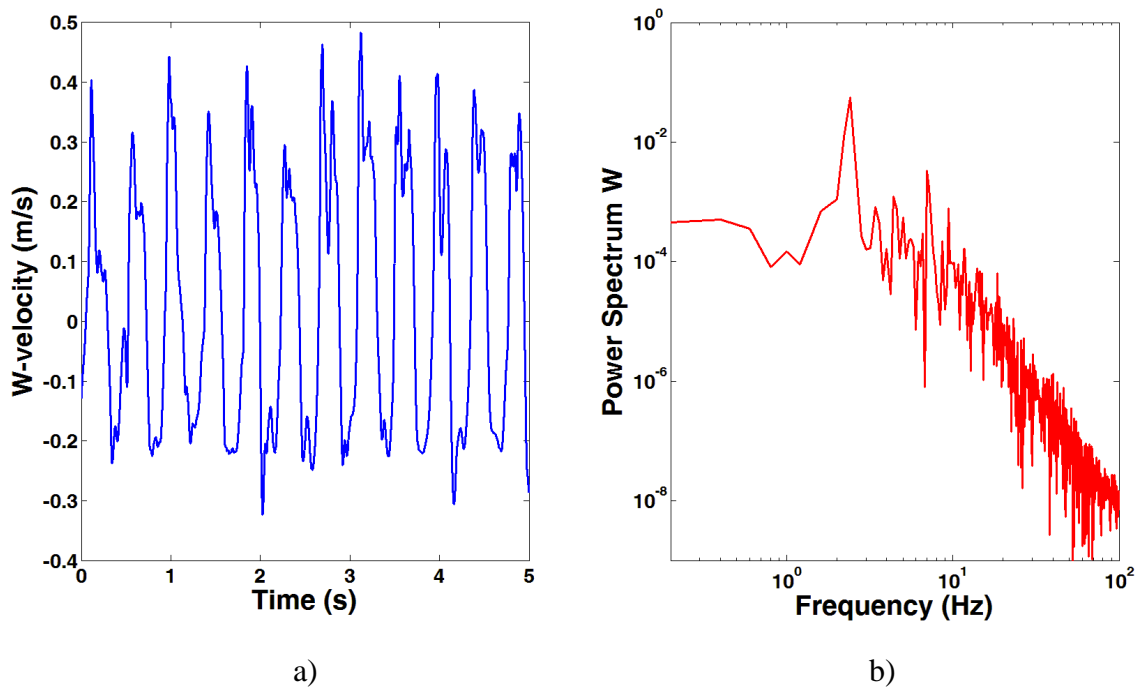
Figure 2.7. a) Trace, and b) power spectrum of transverse velocity for a probe in the near-wake of the prism $(X = 2D, Y = 3H/4, Z = D/2)$

27

Figure 2.8 shows the phase-averaged streamwise vorticity and velocity vectors in a transverse plane at X = 3D. Five phases are shown, N = 1 to 5. The velocity field includes a transverse component that sweeps across the wake creating strongly asymmetric flow patterns. The associated movement of the dominant vortices across the wake is clear evidence of periodicity. For phases 1 and 2, strong vortices with clockwise rotation (negative vorticity) are observed on the left side of the wake; for phases 4 and 5, strong vortices with counter-clockwise rotation (positive vorticity) are present on the right side of the wake. Phase 3 might be a transition phase where there are strong vortices of each sign, and the dominant structure is moving from left to right.

Figure 2.9 presents the velocity vectors and associated in-plane spanwise vorticity in a horizontal plane at Y = H/4 for the discrete phases N = 1 to 5. Unlike the time-averaged flow field, the phase-averaged results provide strong evidence of periodicity and reveal the characteristic features of vortex shedding. For phases 1, 2 and 3 a structure with clockwise rotation (negative vorticity) is observed to detach from the upper corner of the cylinder; subsequently, in phases 3, 4 and 5 a structure with counter-clockwise rotation (positive vorticity) detaches from the lower corner. In each case, the wake region downstream tends to swing away from the side where separation occurs. It is in some ways unexpected that the flow relatively close to the ground plane should exhibit a vortex shedding pattern reminiscent of that on an infinite prism. It turns out that the periodic structure responsible for this behaviour is much more complex than for the two-dimensional case.

Figure 2.10 shows the 3D (three-dimensional) vortical structure of the wake for phases N = 1 to 5 visualized using the second invariant of the velocity gradient tensor flooded by streamwise velocity. The flow field is strongly asymmetric with a very clear periodic structure. The shear layers being shed from the two sidewalls and top surface of the prism roll up to form vortex tubes that change their orientation as they move downstream. For phase N = 2, the streamwise extent of the structure shed from the left-hand sidewall is greater than the structure shed from the right-hand sidewall. Furthermore, a distinct tube-like strand extends from the left-hand side of the flow across the centre of the wake and then connects vertically to the ground plane. This phenomenon is strongly suggestive of the half-loop structure proposed by Bourgeois et al. (2011). It also resembles the instantaneous flow structure described by Palau-Salvador et al. (2010) for the case of a finite circular cylinder at higher Reynolds numbers. The flow development over the five

c)Phase N = 3

a)Phase N = 1

d)Phase N = 4

b)Phase N = 2

e)Phase N = 5
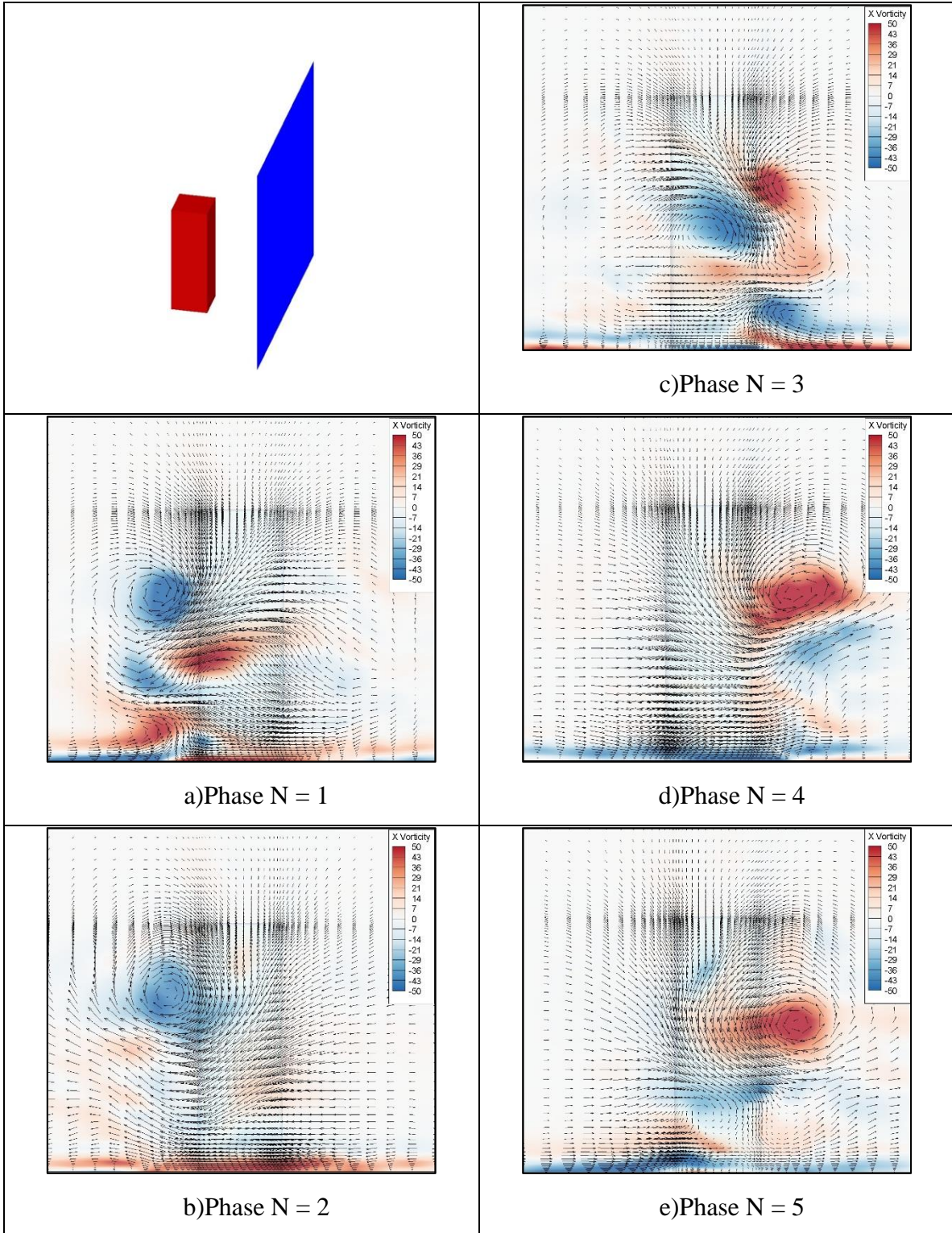
Figure 2.8. Phase-averaged streamwise vorticity and velocity vectors at X = 3D for phases N = 1 to 5 .

29
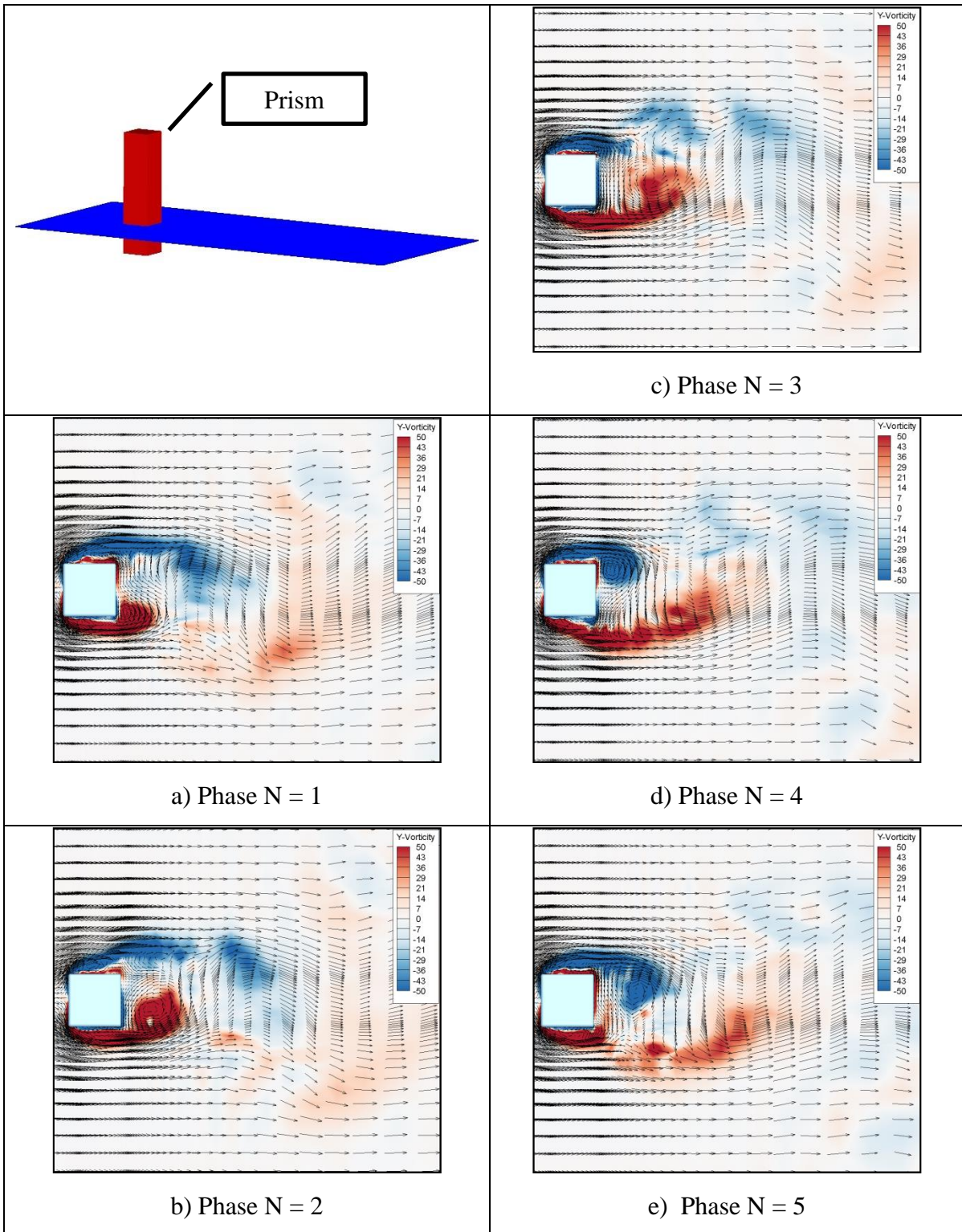
Figure 2.9. Phase-averaged velocity vectors and vertical vorticity contours in a horizontal plane located at Y = H/4 for phases N = 1 to 5.

a) Phase N = 1

b) Phase N = 2

c) Phase N = 3

d) Phase N = 4

e) Phase N = 5
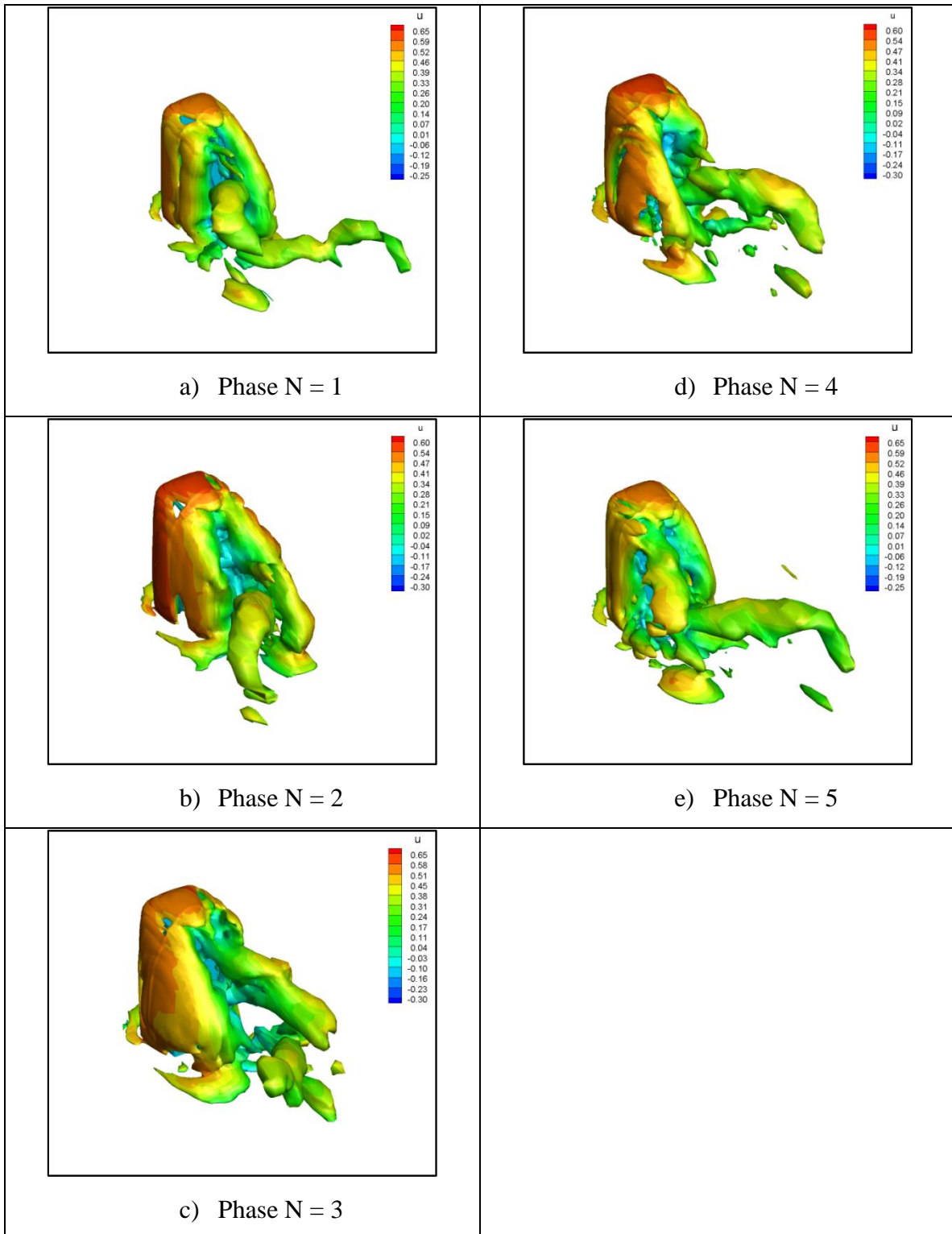
Figure 2.10. Phase-averaged 3D vortical structure visualized using second invariant (Q = 200)

flooded by streamwise velocity for phases N = 1 to 5.

phases suggests that during a single period, a half-loop structure is generated sequentially on each side of the prism wake, e.g. for phases N = 2 and N = 4, a half-loop is observed on the left and right side of the wake, respectively.

2.5 Conclusions

The present paper documents an LES study of a low Reynolds number flow over a finite-height square prism mounted on a ground plane. The flow field predicted for this sub-critical aspect ratio of AR = 3 reveals a complex wake structure created by the interaction of the flow over top of the prism with the flow near the ground plane. The time-averaged flow structure shows two strong tip vortices aligned in the streamwise direction. Unlike the time-averaged velocity field, the phase-averaged velocity field indicates asymmetric and periodic flow structures associated with the vortex tubes being shed from the top and side walls of the prism. These tubes re-orient and interact as they detach from the prism, and give evidence of the half-loop structure proposed by Bourgeois *et al.* (2011). The phase-averaged velocity field in transverse plane sections through the wake also indicates strong downwash flow between pairs of dominant vortical streamwise structures that change their location over the course of a single periodic cycle.

2.6 Acknowledgements

2.7 References

Bourgeois, J. A., Sattari, P., and Martinuzzi, R. J. (2011). Alternating half-loop shedding in the turbulent wake of a finite surface-mounted square cylinder with a thin boundary layer. *Physics of Fluids, 23* (9), 095101. <u>DOI: 10.1063/1.3623463</u>

Palau-Salvador, G., Stoesser, T., Frohlich, J., Kappler, M., and Rodi. W., (2010). Large eddy simulations and experiments of flow around finite-height cylinders. *Flow, Turbulence and Combustion, 84* (2), 239-275. <u>DOI: 10.1007/s10494-009-9232-0</u>

Rostamy, N., Sumner, D., Bergstrom, D.J., and Bugg., J.D. (2012). Local flow field of a surface-mounted finite circular cylinder. *Journal of Fluids and Structures, 34*, 105-122. <u>DOI: 10.1016/j.jfluidstructs.2012.04.014</u>

Saha, A. K., Biswas, G., and Muralidhar, K. (2003). Three-dimensional study of flow past a square cylinder at low Reynolds numbers. *International Journal of Heat and Fluid Flow, 24* (1), 54-66. <u>DOI: 10.1016/S0142-727X(02)00208-4</u>

Wang, H. F. and Zhou, Y. (2009). The finite-length square cylinder near wake. *Journal of Fluid Mechanics, 638*, 453-490. <u>DOI: 10.1017/S0022112009990693</u>

Chapter 3

Large Eddy Simulation of a Finite Prism Wake Flow Using Dynamic Linear and Nonlinear Subgrid-Scale Models

A similar version of this chapter has been submitted as:

N. Moazamigoodarzi and D.J. Bergstrom, "Large Eddy Simulation of a Finite Prism Wake Flow Using Dynamic Linear and Nonlinear Subgrid-Scale Models", *International Journal of Computers & Fluids.*

In addition, a part of this chapter was presented at the following conference:

N. Moazamigoodarzi and D.J. Bergstrom, "LES of Finite Cylinder Wake Flows using Dynamic Linear and Nonlinear Subgrid-Scale Models", *24th Canadian Congress of Applied Mechanics*, University of Saskatchewan, Saskatoon, Canada, 2-6 June 2013.

Preamble

The third chapter of this thesis concerns dynamic subgrid-scale models for large eddy simulation. The current chapter reports the application of two different dynamic subgrid-scale models. Both linear and nonlinear dynamic subgrid-scale model formulations are implemented and then tested for their ability to resolve the complex wake structure associated with this flow.

The current chapter contributes to the first objective of this thesis (described in Section 1.2.1), which is to compare and assess the performance of two different dynamic SGS models in predicting the flow over a finite-height prism, with respect to flow structure and SGS energy transfer.

The current chapter forms a major part of the first contribution of the thesis (described in Section 1.3.1), which is to perform two large eddy simulation (LES) studies and assess the validity of the results. The chapter also forms a part of the second contribution (described in Section 1.3.2), which is to explore and contrast the main features of the mean and instantaneous velocity fields for the two SGS models. Finally, the chapter forms a part of the third contribution (described in Section 1.3.3), which is to analyze the dissipation of turbulence kinetic energy for the two different SGS models.

In this context, the present chapter considers the application of linear and nonlinear dynamic subgrid-scale models to predict the complex wake flow behind a finite-height square prism of the aspect ratio AR = 3 (AR = H/D, where H is the cylinder height and D is the cylinder width), mounted normal to a ground plane. The boundary layer is relatively thin and laminar $\delta/D \approx 0.2$ where δ is the boundary layer thickness, and the Reynolds number, based on the cylinder width and freestream velocity, is Re = 500. The time-averaged and instantaneous flow fields are compared, including resolved velocity, vorticity, and turbulence kinetic energy dissipation (SGS, resolved, and total). The characteristics of the velocity and vorticity fields predicted by the two dynamic models are documented. Overall, significant differences are observed in the mean wake structure predicted by the two models.

Abstract

Dynamic subgrid-scale models for large eddy simulation offer the promise of being able to dynamically calibrate the residual stress field to the local flow conditions. The current paper reports the application of two different dynamic subgrid-scale models to predict turbulent flow over a finite-height square prism mounted normal to a ground plane. The prism aspect ratio was AR = 3, the Reynolds number based on the prism width and freestream velocity was Re = 500, and the boundary layer thickness at the location of the prism was 5% of the height of the prism. The flow field is complex, since the flow over the top of the prism interacts with the flow along the ground plane to create a complicated wake structure. The wake is characterized by a velocity field that changes rapidly in both direction and magnitude. Both linear and nonlinear dynamic subgrid-scale model formulations were implemented, and tested for their ability to resolve the complex wake structure associated with this flow. Of special interest were the instantaneous backscatter and subgrid-scale dissipation of kinetic energy predicted by the dynamic models. Overall, differences were observed in the wake structure predicted by the two models, including some features of the mean velocity field.

3.1 Introduction

Large Eddy Simulation (LES) is a reasonably affordable numerical method to predict relatively complex flows. LES resolves the large-scale motions directly, but it requires a subgrid-scale (SGS) model to incorporate the effects of the small-scale structures. Smagorinsky (1963) introduced a SGS model that was based on a linear relationship between the SGS or residual stress tensor and the local resolved-scale velocity gradient field. In the Smagorinsky model formulation, the unknown model coefficient must be selected for a specific flow, and explicit damping functions are required in near-wall regions. Germano *et al.* (1991) introduced an improved version of the Smagorinsky formulation. This model, called the dynamic Smagorinsky model (DSM), implements a dynamic procedure whereby the model coefficient is computed dynamically at each point and time via a double filtering procedure in physical space rather than input a priori.

Typically, in a turbulent flow kinetic energy transfers from large scales to small scales, which is termed forward-scatter. However, observations of the instantaneous velocity field also show that energy can be transferred from the small scales to the large scales. This phenomenon is called backscatter (Meneveau and Katz, 2000). In order to admit backscatter in LES, the DSM needs to allow the local instantaneous SGS viscosity to become negative. Although the dynamic procedure computes both Forward-scatter and backscatter, in practice, the DSM can become locally unstable for a negative value of the SGS viscosity. It is therefore most often implemented using procedures such as plane-averaging and/or a clipping function to control the computational stability (Baya Toda *et al*. 2014). These stabilizing techniques often effectively remove the feature of local backscatter.

Some SGS models are inherently capable of predicting backscatter. A dynamic SGS model formulation which adopts a quadratic nonlinear relationship between the SGS stress tensor and local velocity gradient tensor was proposed by Wang and Bergstrom (2005). This dynamic nonlinear model (DNM) adopts a much more comprehensive coupling of the SGS stress to the resolved velocity gradient field. It also has the advantage of being able to predict backscatter in a locally robust manner without any need for plane-averaging or other stabilization techniques. Heinz (2008) noted that the DSM has a stability issue due to uncontrolled fluctuations, which he related to an incorrect scale dependence. Heinz and Gopalan (2012) and Heinz *et al.* (2015) compared a realizable linear dynamic model (LDM) and a realizable nonlinear dynamic model (NDM) to the DSM and DNM. They found the LDM and NDM predicted backscatter and small-scale scale structures without any stability issues, and were computationally more affordable than the DNM and DSM. Using a different approach, Sohankar *et al.* (1999) developed a dynamic one-equation model that provides better performance than the standard Smagorinsky model and DSM, and does not require any stabilization methods.

Various techniques have been used to stabilize the coefficients in dynamic models, for example spatial averaging over statistically homogeneous planes. The DSM and a scale-invariant dynamic model were tested in a LES of an atmospheric boundary layer flow by Basu and Porté-Agel (2006). Both SGS models used a stability function to limit the value of the SGS viscosity. Meneveau *et al*. (1996) introduced a stabilization mechanism that is applicable for inhomogeneous flows in

complex geometries and does not constrain the SGS viscosity to be only positive. Their model implemented averaging along the flow pathlines, i.e. used a Lagrangian averaging technique. Tran and Sahni (2017) used LES based on a residual-based variational multiscale model and the DSM to predict a turbulent channel flow and flow over a cylinder. To stabilize the model coefficients, they used a spatial averaging method for the channel flow and Lagrangian averaging for the cylinder flow.

Note that most SGS models, including the dynamic formulations noted above, were originally developed for plane channel flows. Their performance in more complex flows has not been as thoroughly investigated. An example of a more complex flow is the flow over a finite-height square prism mounted on a ground plane. In this case, the prism wake is strongly influenced by both the tip vortex structures which develop at the free end of the prism, as well as the boundary layer developing on the ground plane. The wake of a finite prism has a complicated structure (Bourgeois *et al.*, 2011), and has been shown to include a quasi-periodic component in addition to the turbulent fluctuations (Wang and Zhou, 2009). As such, these flows provide a much more critical test case for dynamic SGS models than the turbulent channel flows originally used for their validation. For the flow over a finite prism, the Reynolds number and aspect ratio of the prism affect the flow structure. Zhang *et al.* (2017) performed a direct numerical simulation (DNS) of the flow over a finite prism of aspect ratio AR = 4 for a Reynolds number that ranged from 50 to 1000. Saha (2013) used DNS to investigate the effect of aspect ratio (AR = 2, 3, 4, and 5) on a finite prism flow at a Reynolds number of Re = 250.

The present paper considers the application of a linear (DSM) and nonlinear (DNM) dynamic SGS model to predict the wake flow behind a finite-height square prism of aspect ratio AR = 3 (AR = H/D, where H is the prism height and D is the prism width) mounted normal to a ground plane for a Reynolds number based on the prism width and free-stream velocity of Re = 500. The study investigates the effects of the SGS model on both the mean and instantaneous velocity fields in the wake. It also examines the effect of the SGS model on the resolved and total dissipation of the turbulence kinetic energy.

3. 2 Mathematical Model

This section will summarize the filtered Navier-Stokes equations used for the LES, and then briefly describe the dynamic SGS models. For the purpose of describing the dynamic procedure, two filtering operations are introduced, i.e. the grid filter and the test filter. The grid-filtered Navier-Stokes and continuity equations for constant properties are given as follows (Sagaut, 2002):

$$\frac{\partial \bar{u}_\iota}{\partial t} + \frac{\partial (\bar{u}_\iota \, \bar{u}_j)}{\partial x_j} = -\frac{1}{\rho}\frac{\partial \bar{p}}{\partial x_i} - \frac{\partial \tau_{ij}}{\partial x_j} + \nu \frac{\partial^2 \bar{u}_\iota}{\partial x_j^2} \tag{3.1}$$

$$\frac{\partial \bar{u}_\iota}{\partial x_i} = 0 \tag{3.2}$$

where x_j is spatial coordinate in the j direction; u_i is the velocity component in the i direction; p is the pressure, τ_{ij} is the ij component of the SGS stress tensor; t is the time; ν is the kinematic viscosity; and ρ is the density. The overbar indicates that these variables are grid-filtered. The quantity

$$\tau_{ij} = \overline{u_\iota u_j} - \bar{u}_\iota \bar{u}_j \tag{3.3}$$

is the SGS stress tensor at the grid-scale and represents the contribution of the unresolved scales to the momentum transport.

The test-grid filtered Navier-Stokes equation for constant properties is similarly defined (Germano *et al.*, 1991), i.e.,

$$\frac{\partial (\widetilde{\bar{u}}_\iota)}{\partial t} + \frac{\partial (\widetilde{\bar{u}}_\iota \, \widetilde{\bar{u}}_j)}{\partial x_j} = -\frac{1}{\rho}\frac{\partial \widetilde{\bar{p}}}{\partial x_i} - \frac{\partial T_{ij}}{\partial x_j} + \nu \frac{\partial^2 \widetilde{\bar{u}}_\iota}{\partial x_j^2} \tag{3.4}$$

where the tilde indicates filtering at the test-grid level. In this case the test-grid is defined by a control volume that is twice as large as the grid-scale control volume. The quantity

$$T_{ij} = \widetilde{\overline{u_i u_j}} - \widetilde{\overline{u}}_i \widetilde{\overline{u}}_j \tag{3.5}$$

is the *ij* component of the SGS stress at the test-grid level.

In this study, the LES predictions consider two different models for the SGS stress, i.e. the DSM and DNM. Both of these dynamic models use information from the test-grid level to determine the unknown model coefficient.

3.2.1 Dynamic Smagorinsky Model

Arguably the most popular dynamic procedure was introduced by Germano *et al.* (1991) to address the inadequacies of the Smagorinsky model. In this procedure, the model coefficient is computed dynamically at every point for each time-step directly from the instantaneous velocity field predicted by the LES itself. The dynamic procedure extracts information via a double filtering in physical space. Applying the test filter to the grid-filtered SGS stress tensor results in

$$\tilde{\tau}_{ij} = \widetilde{\overline{u_i u_j}} - \widetilde{\overline{u}_i \overline{u}_j} \tag{3.6}$$

The two SGS stress tensors are related by the resolved-scale Leonard stress, which can be calculated explicitly as follows:

$$L_{ij} = \widetilde{\overline{u}_i \overline{u}_j} - \widetilde{\overline{u}}_i \widetilde{\overline{u}}_j = T_{ij} - \tilde{\tau}_{ij} \tag{3.7}$$

This relation implies that the velocity fields on the grid and test scales are related through the intermediate scales, which represent a type of test window (Germano *et al.*, 1991).

The DSM assumes similarity of the SGS motions, and uses the following expressions for the anisotropic form of the grid and test-filtered SGS stress tensors:

$$\tau_{ij}^* = -2C_s \Delta^2 |\bar{S}| \overline{S_{ij}} = -C_s \beta_{ij} \tag{3.8}$$

$$T_{ij}^* = -2C_s \tilde{\Delta}^2 \left| \widetilde{\bar{S}} \right| \widetilde{\overline{S_{ij}}} = -C_s \alpha_{ij} \tag{3.9}$$

40

where C_s is a model coefficient, and β_{ij} and α_{ij} can be viewed as the basis functions for the SGS stress at the grid and test-grid scale, respectively. For the grid-scale field, the strain rate tensor and its magnitude are defined as follows:

$$\bar{S}_{ij} = \frac{1}{2}\left(\frac{\partial \bar{u}_i}{\partial x_j} + \frac{\partial \bar{u}_j}{\partial x_i}\right)$$
(3.10)

$$|\bar{S}| = (2\bar{S}_{ij}\bar{S}_{ij})^{0.5}$$
(3.11)

The strain rate tensor, $\widetilde{\bar{S}_{ij}}$, and its magnitude, $\widetilde{|\bar{S}|}$, for the test-scale field are defined in a similar fashion.

Substituting equations (3.8) and (3.9) into the equation (3.7) for the Leonard stress, and assuming that the model coefficient C_s is unaffected by the test-grid filter operation yields the following relation:

$$L_{ij} = -C_s\,\alpha_{ij} + C_s\widetilde{\beta_{ij}} = -C_s\left(\alpha_{ij} - \widetilde{\beta_{ij}}\right)$$
(3.12)

Lilly (1992) modified the model originally developed by Germano *et al.*, (1991) by using a least squares method to determine the value of the coefficient C_s working from an indeterminate set of equations. He minimized the error between the calculated and modelled values of the Leonard stress given by

$$E = \left(L_{ij} + C_s\,M_{ij}\right)^2$$
(3.13)
where
$$M_{ij} = \alpha_{ij} - \widetilde{\beta_{ij}}$$
(3.14)

The resultant expression for the model coefficient is given by:

$$C_s = -\frac{L_{ij}M_{ij}}{M_{ij}M_{ij}} \tag{3.15}$$

The stability of Lilly's model is an improvement over the original model formulation of Germano *et al.* (1991). However, it still requires application of some *ad hoc* numerical techniques to prevent the prediction of large negative values of the model coefficient, which can cause numerical instability and divergence of a solution. For the wake flow being considered, averaging over homogenous planes was not possible. Instead, the model coefficient was first volume-averaged and subsequently the value of the implied SGS viscosity ($v_{sgs} = C_s(\Delta)^2|\bar{S}|$) was limited based on the following constraints:

$$v_{sgs}(\text{max}) = 5v \tag{3.16}$$
$$v_{sgs}(\text{min}) = -v \tag{3.17}$$

This approach yielded a sufficiently robust numerical algorithm, while the bounds considered still allowed the possibility of backscatter.

3.2.2 Dynamic Nonlinear Model

In the dynamic nonlinear model formulation of Wang and Bergstrom (2005), the SGS stress tensors are defined as follows:

$$\tau_{ij}^* = -C_s\beta_{ij} - C_w\gamma_{ij} - C_N\eta_{ij} \tag{3.18}$$
$$T_{ij}^* = -C_s\alpha_{ij} - C_w\lambda_{ij} - C_N\zeta_{ij} \tag{3.19}$$

where the additional basis functions depend on both the local strain rate and rotation rate tensors, i.e.

$$\gamma_{ij} = 4\Delta^2 \left(\bar{S}_{ik} \bar{\Omega}_{kj} - \bar{\Omega}_{ik}\bar{S}_{kj} \right) \tag{3.20}$$

$$\eta_{ij} = 4\Delta^2 \left(\bar{S}_{ik}\bar{S}_{kj} - \frac{1}{3} \bar{S}_{mn}\bar{S}_{nm}\delta_{ij} \right) \tag{3.21}$$

$$\lambda_{ij} = 4 \, \tilde{\Delta}^2 \left(\tilde{\bar{S}}_{ik} \widetilde{\tilde{\bar{\Omega}}}_{kj} - \widetilde{\tilde{\bar{\Omega}}}_{ik} \tilde{\bar{S}}_{kj} \right) \tag{3.22}$$

$$\zeta_{ij} = 4 \, \tilde{\Delta}^2 \left(\tilde{\bar{S}}_{ik} \tilde{\bar{S}}_{kj} - \frac{1}{3} \tilde{\bar{S}}_{mn} \tilde{\bar{S}}_{nm} \, \delta_{ij} \right) \tag{3.23}$$

For the grid-scale field, the rotation rate tensor and its magnitude are defined as follows:

$$\bar{\Omega}_{ij} = \frac{1}{2} \left(\frac{\partial \bar{u}_i}{\partial x_j} - \frac{\partial \bar{u}_j}{\partial x_i} \right) \tag{3.24}$$

The rotation rate tensor for the test-grid scale field is defined in a similar fashion.

Introducing the above relations in the expression for the Leonard stress given by equation (3.7) results in the following equation:

$$L_{ij}^* = -C_s M_{ij} - C_w W_{ij} - C_N N_{ij} \tag{3.25}$$

where in addition to M_{ij} given by equation (3.14), we have introduced the following definitions:

$$W_{ij} = \lambda_{ij} - \widetilde{\gamma_{ij}} \tag{3.26}$$

$$N_{ij} = \zeta_{ij} - \widetilde{\eta_{ij}} \tag{3.27}$$

and C_W and C_N are two new model coefficients. The values of the model coefficients can be obtained from solving the following set of linear algebraic equations using the value of the Leonard stress evaluated from the resolved-scale and test-grid fields:

$$\begin{bmatrix} M_{ij}M_{ij} & M_{ij}W_{ij} & M_{ij}N_{ij} \\ W_{ij}M_{ij} & W_{ij}W_{ij} & W_{ij}N_{ij} \\ N_{ij}M_{ij} & N_{ij}W_{ij} & N_{ij}N_{ij} \end{bmatrix} \begin{bmatrix} C_s \\ C_w \\ C_N \end{bmatrix} = - \begin{bmatrix} L_{ij}^* M_{ij} \\ L_{ij}^* W_{ij} \\ L_{ij}^* N_{ij} \end{bmatrix} \tag{3.28}$$

According to the above equations, the first order term of the DNM is given by the DSM relation.

3.2.3 Transport equation for resolved-scale turbulence kinetic energy

One of the important features of a SGS model is to provide adequate dissipation of turbulence kinetic energy, which can be viewed as the transport of energy from the resolved scales to the unresolved scales. Following Meneveau and Katz (2000), the transport equation for the time-averaged resolved-scale turbulence kinetic energy, $K = \frac{1}{2} < \bar{u}_i \bar{u}_i >$, is given as follows where angle brackets denote time-averaging:

$$\frac{\partial K}{\partial t} + < \bar{u}_j > \frac{\partial K}{\partial x_j} = -\frac{\partial A_j}{\partial x_j} - 2v < \bar{S}_{ij} \bar{S}_{ij} > + < \tau_{ij} \bar{S}_{ij} > \tag{3.29}$$

The term A_j is a flux term consisting of third-order moments of the velocity field, pressure and viscous stress transport. The second term on the right-hand side, typically denoted ε , is the time-averaged resolved-scale dissipation. The third term is the so-called SGS dissipation associated with the transfer of energy from the resolved-scale to unresolved-scale fields. The negative sign for the SGS dissipation indicates that it acts as a sink for the resolved-scale energy but as a source for the SGS energy. The resolved-scale and SGS dissipation will be used to analyse the performance of the two SGS models in predicting the wake flow.

3.3 Numerical Method

The mathematical model consisting of the filtered continuity and Navier-Stokes equations was discretized using the finite-volume method. The discrete form of the continuity and momentum equations were solved using a second order fractional-step method, where the convective and diffusive terms are advanced in time using the semi-implicit Crank-Nicolson method. Upstream of the cylinder where the turbulence field was zero, a third-order QUICK scheme was used to stabilise the flow and eliminate spurious values of the SGS viscosity calculated by the DSM. The velocity field was corrected to ensure mass conservation using a pressure-correction method. A four-level multi-grid (MG) method was used to efficiently solve the linear algebraic equations obtained from the pressure-correction method.

Figure 3.1 shows the solution domain and identifies the boundary conditions. In this simulation, the freestream velocity was set to U = 0.375 m/s, the prism width was D = 0.02 m, and the prism height was H = 0.06 m, which yielded a Reynolds number of Re = 500. Note that given the short upstream extent of the solution domain, the laminar boundary that developed on the ground plane was relatively thin, i.e. the boundary layer thickness δ at the location of the prism was estimated to be approximately δ/D ≈ 0.2.
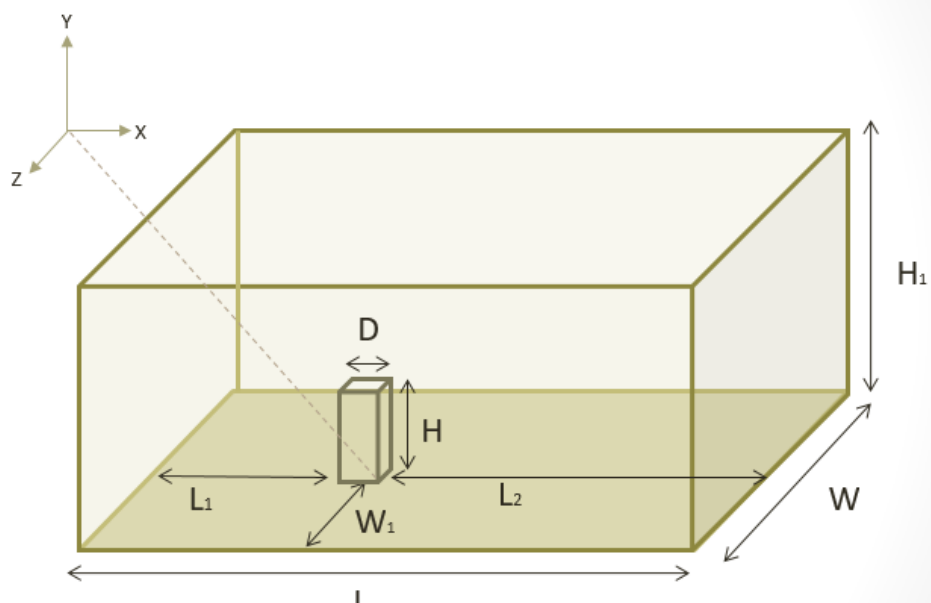
Figure 3.1. Domain and prism location.

The domain size was chosen to ensure that it is large enough to not adversely impact the development of the wake. The domain size was 16D in the streamwise (X) direction, consisting of an upstream length of 3D, 1D for the prism and 12D downstream of the prism. The domain was 6D in the wall-normal (Y) direction and 7D in the transverse (Z) direction. The blockage ratio, which is the cross-sectional area of the prism divided by cross-sectional area of the domain, was approximately 7.1%. The domain size was chosen based on the study of Frohlich and Rodi (2004) of a finite circular cylinder with AR = 2.5, Re = 43000, and a boundary layer thickness equal to 10% of the cylinder height. As shown in Table 3.1 their study used the same blockage ratio.

	AR	Re	Boundary layer thickness	Domain (width * height*length)	Blockage ratio
Frohlich and Rodi (2004)	2.5	43000	10% H	7D*5D*19D	7.1%
Current study	3	500	5% H	7D*6D*16D	7.1%

Table 3.1. Domain comparison

Frohlich and Rodi (2004) validated their numerical results against the experimental study performed by Kappler (2002), which confirmed that the domain size was sufficient. Although the wake width varies slightly with Reynolds number and aspect ratio, the effect of the domain size can also be assessed by comparison to the two DNS studies. The maximum width of the wake in the current study is approximately 2D, which is comparable to the value of 2.5D in the study by Zhang *et al.* (2017) for AR = 4 and Re = 500, and 2.2D in the study by Saha (2013) for AR = 3 and Re = 250. Finally, one erroneous effect of too small a domain size is the acceleration of the flow along the lateral boundaries of the domain. According to Figure 3.11, the streamlines show very little curvature near the lateral surfaces of the domain, which in this case were no-slip walls.

Figures 3.2 and 3.3 show vertical and horizontal sections, respectively, of the non-uniform Cartesian grid used for this study. Hyperbolic-tangent functions were used to cluster the hexahedral cells. The grid was refined near the no-slip walls, which included the prism walls and the ground plane. The grid was coarsened downstream and away from the solid walls. The total number of control volumes was approximately 1.77 million, consisting of $128 \times 144 \times 96$ control volumes in the streamwise (X), vertical (Y) and transverse (Z) directions, respectively. The number of control volumes used to define the prism were $N_x = N_z = 34$ in the streamwise and transverse directions, and $N_y = 98$ in the vertical direction.
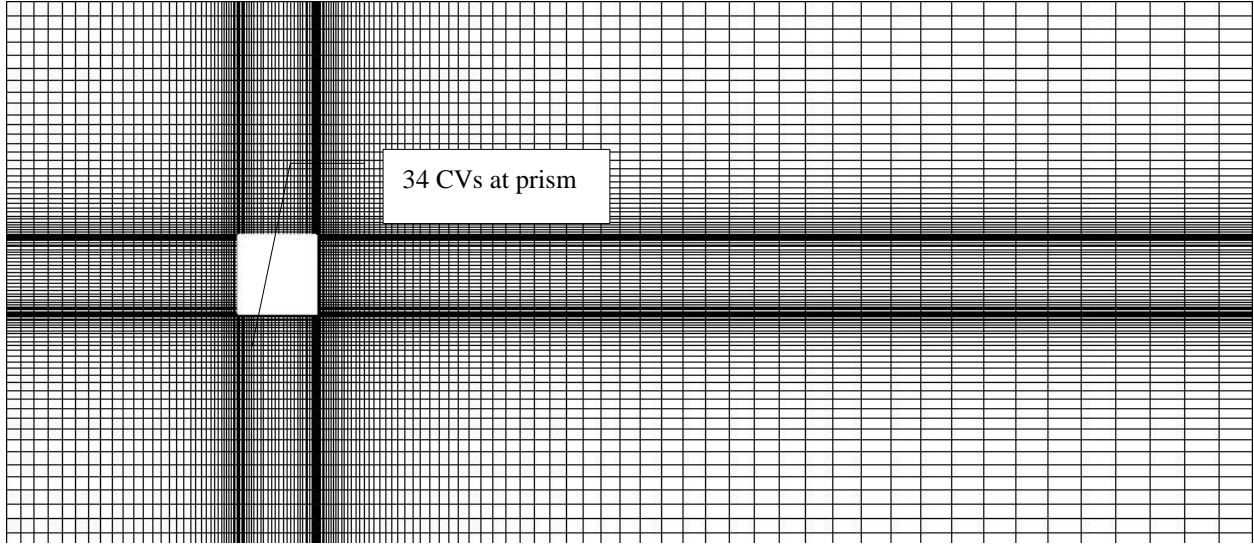
Figure 3.2. Grid section in the horizontal $(X - Y)$ mid-plane.
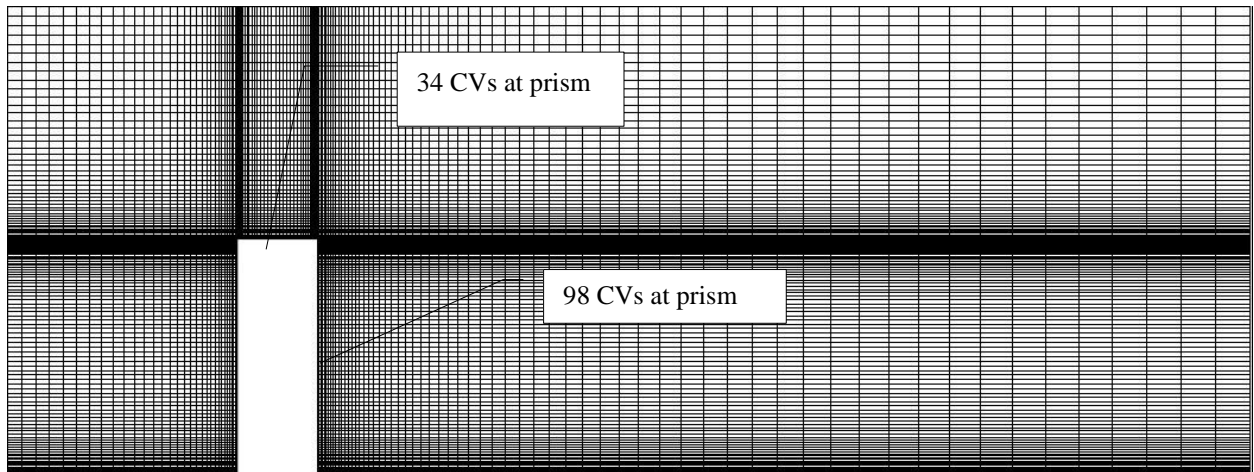
Figure 3.3. Grid section in the vertical $(Y - Z)$ mid-plane.

Table 3.2 compares the current study with two other low Reynolds DNS studies, i.e. Saha (2013) and Zhang *et al.* (2017), in terms of such parameters as the number of control volumes, number of control volumes used to define the prism, domain size, near-wall spatial resolution and time-step. The overall size of the grid is less than that of the DNS studies, as expected. This study has the highest near-wall resolution and therefore the smallest time-step. In terms of the overall resolution, defined as the ratio of the number of control volumes to the volume of the solution domain, this study has the second highest resolution after the fine grid study of Zhang *et al.* (2017). Overall, we

47

Study	Current work	Zhang et al. 2017 fine	Zhang et al. 2017 coarse	Saha (2013) fine	Saha (2013) medium	Saha (2013) coarse
Method	LES	DNS	DNS	DNS	DNS	DNS
Re	500	1000	50, 100, 150, 250, 500	250	250	250
Aspect ratio	3	4	4	2, 3, 4, 5	2, 3, 4, 5	2, 3, 4, 5
Domain size (X,Y,Z)	16D, 7D, 6D	24D, 16D, 10D	24D, 16D, 10D	24D, 16D, 10D	24D, 16D, 10D	24D, 16D, 10D
Control volumes	144×128×96	303×228×202	262×185×170	204×150×132	177×136×120	152×112×98
N_x, N_y, N_z	34×34×98	48×48×118	42×42×104	42×42×92	34×34×83	26×26×71
Y-coordinate at first node	0.0002	0.0006	0.001	0.005	0.010	0.025
Time-step (s)	Max: 0.0001	0.0005	0.0008	0.002	0.002	0.002

Table 3.2. Grid comparison of previous low Reynolds number square prism studies.

can conclude that compared to the DNS studies, the present LES uses a coarser grid, but with a comparable grid resolution along the prism walls.

The Kolmogorov length scale given by

$$l = \left(\frac{\nu^3}{\varepsilon}\right)^{\frac{1}{4}}$$
(3.30)

is indicative of the smallest scales of motion in a turbulent flow where the dissipation process occurs. For an LES, the total dissipation is given by the sum of the resolved-scale and SGS contributions. The ratio of the local grid scale Δ, which is defined as the maximum dimension of the control volume, to the Kolmogorov length scale l can be used to assess the resolution of the LES. Generally, one would expect the smallest resolved length scale to be within a factor of 10 of the Kolmogorov scale. The value of this ratio for the DNM is plotted in Figure 3.4 for the horizontal mid-plane. Note that in order to better visualise the contours, all values of 1.0 and greater were shown by the same maximum contour level. Although both SGS models have a similar resolution, the DNM predicts a smaller turbulence length scale in the wake compared to the DSM, and hence it was used for the visualization in Figure 3.4. According to this figure, the ratio is highest near the front face of the prism and in the shear layers which separate from the leading edges. Even though the grid is very fine in these regions, the Kolmogorov scales are even smaller, and hence the ratio reaches its largest values in these regions. The maximum value of the ratio is 2.8 for the DNM and 2.1 for the DSM (not shown). Another measure of the resolution of an LES is to compare the effective SGS viscosity to the molecular value. For the DSM, in the same horizontal mid-plane shown in Figure 3.4, the maximum value of the SGS viscosity normalized by the molecular value is $\frac{\nu_{SGS}}{\nu} = 3.7$ and occurs in the mixing region downstream of the near-wake. Overall, the grid adopted is sufficiently fine to ensure a well-resolved LES near the prism and in the near-wake region.

In terms of boundary conditions, the surfaces on the ground plane and prism are modeled as no-slip impermeable walls. The side and top surfaces are modeled as free-slip walls. The velocity

Figure 3.4. Ratio of grid size to Kolmogorov length scale in the horizontal $(X - Z)$ mid-plane predicted by the DNM.

profile specified at the inlet plane is uniform flow with a thin boundary layer region of thickness $\delta/D = 0.01$. The outlet uses a convective boundary condition, i.e.

$$\frac{\partial \emptyset}{\partial t} + U \frac{\partial \emptyset}{\partial x} = 0 \tag{3.31}$$

The mass flux at the exit is corrected to ensure overall mass conservation.

The time-step was selected to ensure a maximum CFL number of $\text{CFL} = \frac{u \, \Delta t}{\Delta x} = 0.3$, which corresponds to a maximum time-step of $\Delta t = 0.0001$ s. After the flow had become fully developed, velocity data were collected to obtain the time-averaged values of the velocity field, as well as the resolved-scale fluctuations. The physical time required to simulate the time-averaged data was 4 s which required 40,000 time-steps. This time interval corresponds to approximately 75 passes of the flow across the top of the prism.

3.4. Results and Discussion

3.4.1 Velocity fields

The present section documents a comparison of the two SGS models, i.e. the DSM and DNM, in terms of predictions for the velocity field in the near-wake region. In each case, both instantaneous and mean flow fields are presented. However, any conclusions drawn from comparisons of the instantaneous fields must be qualified due to the significant variability of the instantaneous velocity field.

Figures 3.5a) and 3.5b) show visualizations of the three-dimensional (3D) instantaneous vortex structures in the near-wake for the DSM and DNM, respectively, using contours of the second invariant of the velocity gradient tensor flooded by streamwise velocity. Recall that the second invariant of the velocity gradient tensor is defined as follows:

$$Q = \frac{\Omega_{ij}\Omega_{ij} - S_{ij}S_{ij}}{2}$$

(3.32)

and is a measure of the local balance between straining and rotational motions (Dubief and Delcayre, 2000). As such it can be used to visualize vortical motions. It is useful to color the structures using the streamwise velocity, since the change in the magnitude and direction of the velocity field in the near-wake results in a strong deformation of the vortical structures shed from the prism.

For both models, the instantaneous 3D wake structure is characterized by the realignment of initially vertical vorticity cores in the streamwise direction. The shear layers being shed from the sides of the prism roll up to form vertically aligned vortex cores. As these cores move downstream, they are stretched and reoriented. Along the outer edge of the near-wake, they form structures which resemble the half-loops observed by Bourgeois *et al.* (2011). A proto-typical half-loop consists of a vertical leg and an approximately streamwise connector strand. Upstream of the prism, multiple horseshoe vortices are observed to wrap around the base and extend downstream along the ground plane interacting with the wake flow. Both SGS models generate very similar
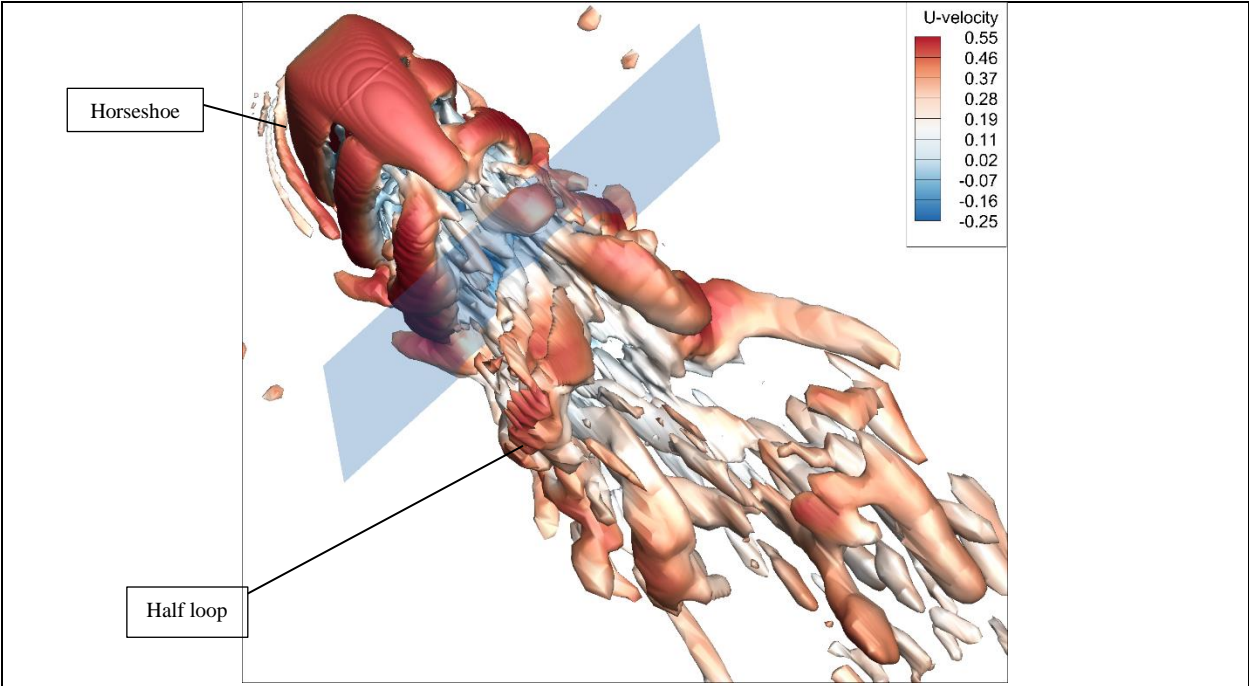
a) DSM, instantaneous, Q=100
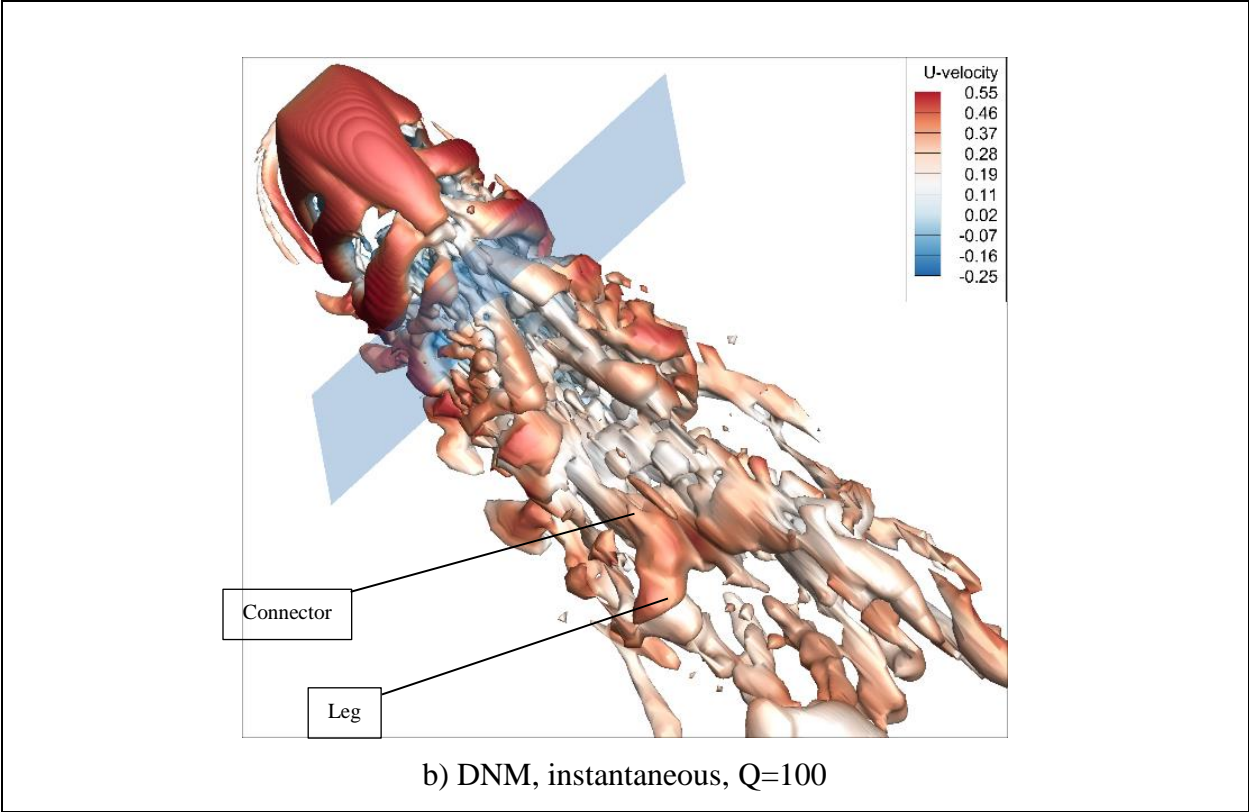
b) DNM, instantaneous, Q=100

Figure 3.5. Visualization of instantaneous vorticity field using second invariant contours flooded by streamwise (**X**) velocity as predicted by: a) DSM, and b) DNM.

flow structures, which are also consistent with the results of previous studies. For the same grid and contour levels, the DNM predicts a noticeably finer-scale structure.

Figures 3.6a) and 3.6b) show visualizations of the 3D time-averaged vortex structures in the near-wake for the DSM and DNM, respectively, using contours of the second invariant of the velocity gradient tensor flooded by streamwise velocity. Both models predict approximately symmetric structures, which is consistent with previous studies by Saha (2013) and Zhang *et al.* (2017). Shear layers are shed from the sides and top of the prism, and reorient themselves in the wake to form two large vortical tubes al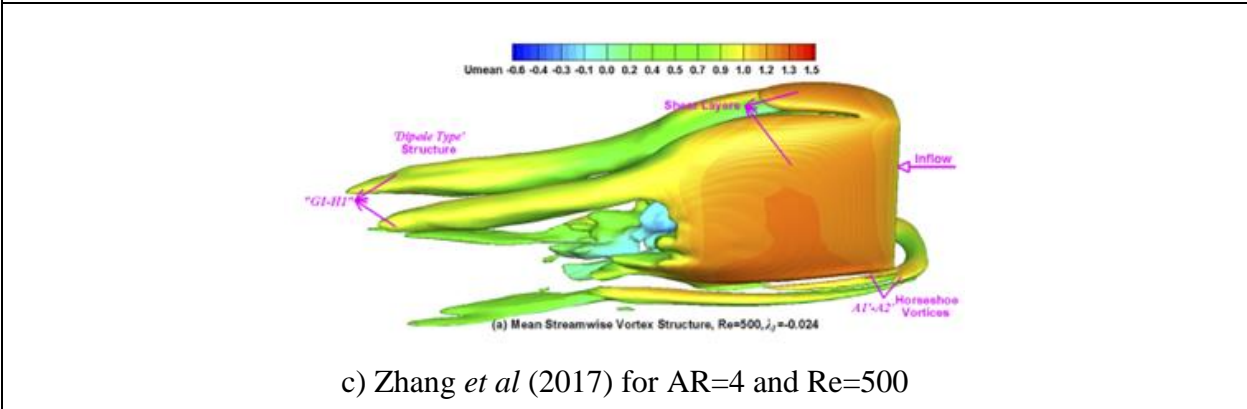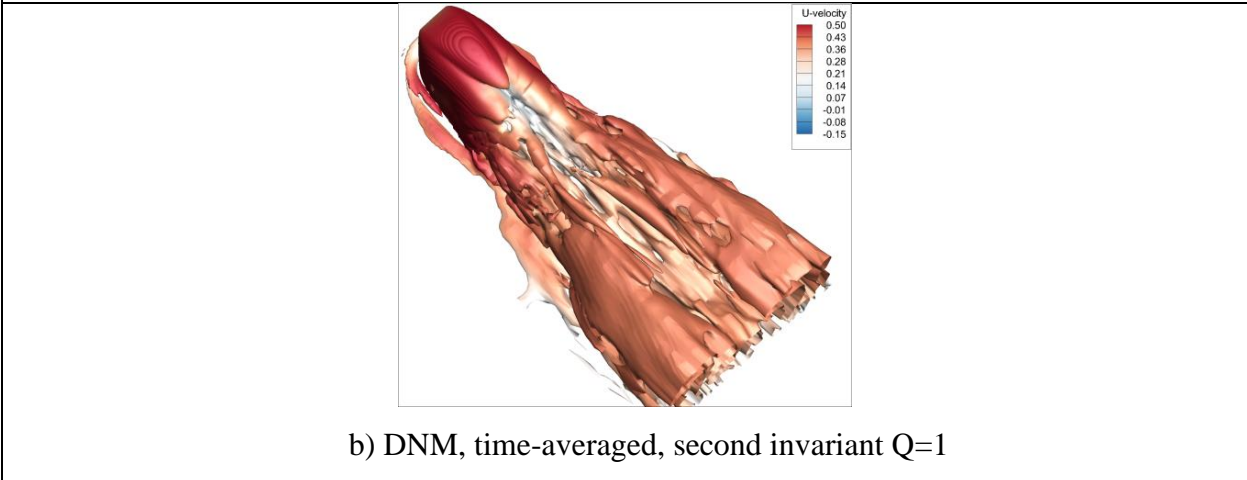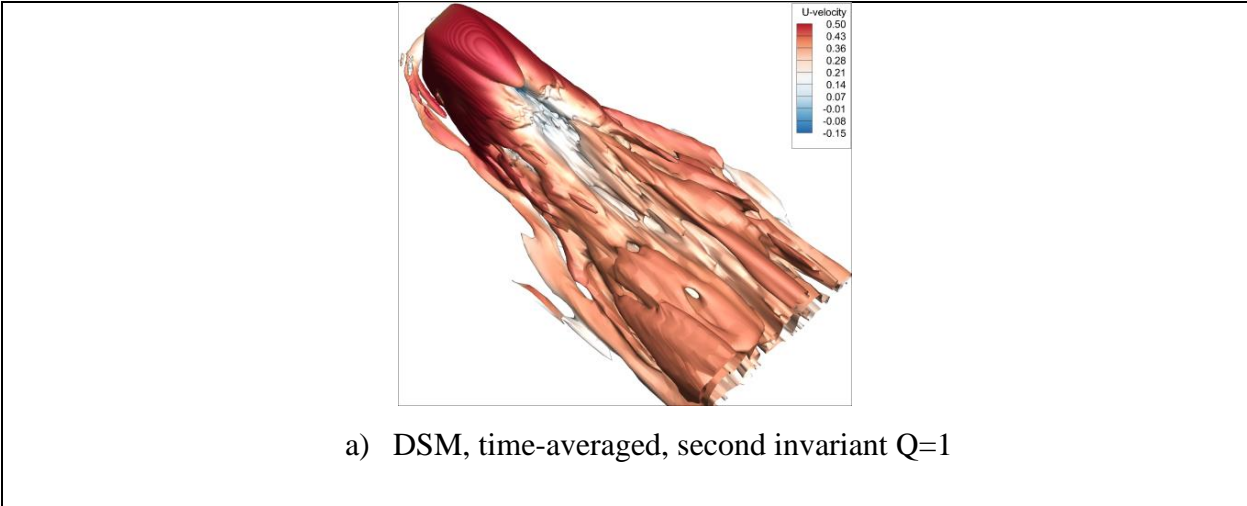igned in the streamwise direction which expand as they extend further downstream. Each larger tube consists of a bundle of smaller tube-like structures. In general, the structure predicted by the DNM is wider than that predicted by the DSM by approximately 10 to 15%. Similar to the instantaneous flow, multiple horseshoe vortices are observed upstream of the prism, which wrap around the prism and extend into the wake region. As shown in Figure 3.6c) Zhang *et al.* (2017) found similar mean flow structures for the case of AR = 4 and Re = 500 using a visualization based on the λ_2 criterion of Jeong and Hussain (1995), i.e. multiple horseshoe vortices, a cap vortex extending from the free-end, and a predominant dipole structure in the wake. However, their visualisation did not reveal the smaller tube-like structures observed in this study. In general, both SGS models predict similar instantaneous and time-averaged 3D vortex structures in the near-wake region.

Figures 3.7a) and 3.7b) show transverse section views of the streamwise vortex structures in a vertical plane located at X = 3D (shown in Figure 3.5) as predicted by the DSM and DNM, respectively. The figures show the instantaneous velocity vectors in the plane, as well as streamwise vorticity. Note that all vorticity contour levels in this paper use dimensional values. For both SGS models the wake region is characterized by a complex pattern of vorticity and becomes wider (in the spanwise direction) near the ground plane. There are many small-scale structures, with vorticity of opposite sign, which can be associated with the streamwise vortex cores shown in the instantaneous 3D field in Figure 3.5. The vortical motions create a complex and dynamic pattern of entrainment into and out of the wake region.

a)   DSM, time-averaged, second invariant Q=1

b) DNM, time-averaged, second invariant Q=1

c) Zhang *et al* (2017) for AR=4 and Re=500

Reprinted from [Zhang, D., Cheng, L., An, H., and Zhao, M. (2017). Direct numerical simulation of flow around a surface-mounted finite square cylinder at low Reynolds number. Physics of Fluids, 29 (4)], with the permission of AIP Publishing.

Figure 3.6. Visualization of time-averaged vorticity field as predicted by: a) DSM, b) DNM, and c) Zhang *et al* (2017).
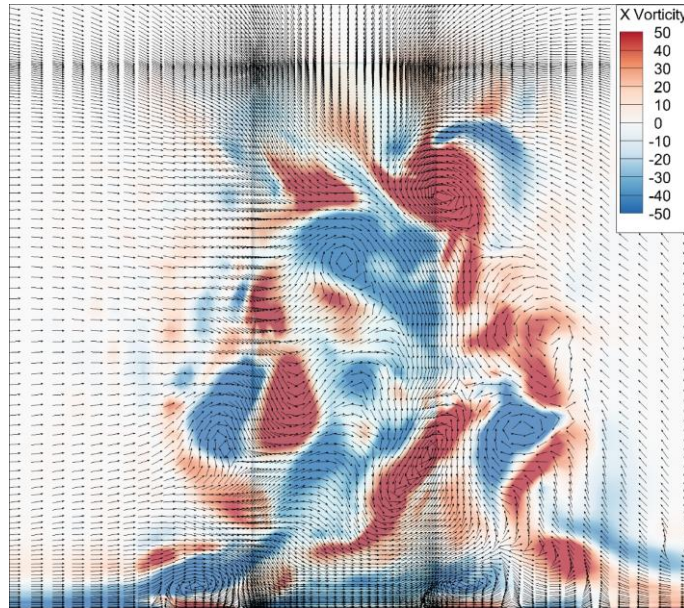
a) DSM, instantaneous
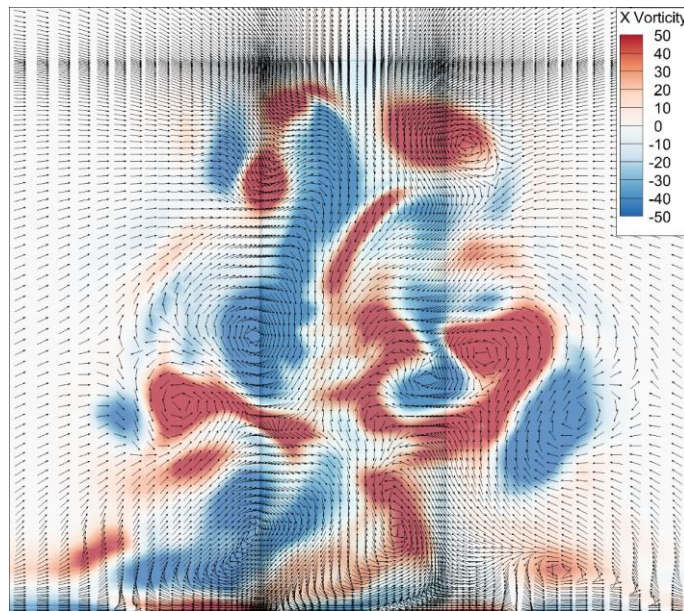
b) DNM, instantaneous

Figure 3.7. Instantaneous streamwise (**X**) vorticity and velocity vectors in a vertical plane located at X = 3D from the downstream face of the prism as predicted by: a) DSM, and b) DNM.

Figures 3.8a) and 3.8b) show the corresponding time-averaged streamwise (X) vorticity contours in a vertical plane located at X = 3D as predicted by the DSM and DNM, respectively. In the time-averaged field there are fewer vortices compared to the instantaneous field. The time-averaged flow is dominated by two streamwise vortical structures of opposite sign; these structures are in general aligned with the sides of the prism, and extend over the entire height of the wake region. The time-averaged vorticity is not completely symmetric, although the patterns of positive and negative vorticity are similar. The vorticity distribution is similar to that observed in the DNS study of Zhang *et al.* (2017) (Figure 3.8c) for an aspect ratio AR = 4 cylinder for a Reynolds number of Re = 1000. They both show two main vortices that are complex in shape and extend over almost the entire height of the prism.

The spanwise extent of the wake region is slightly narrower for the DSM prediction compared to the DNM. Furthermore, the DNM predicts more individual structures compared to the DSM, e.g. on the right-hand side of the wake in Figure 3.8, the DNM contains 6 distinct vortex cores, while the DSM predicts only three cores.

Figures 3.9a) and 3.9b) show instantaneous streamtraces along with transverse (**Z**) vorticity contours on the symmetry plane (**X** − **Y**) as predicted by the DSM and DNM, respectively. Note that for the instantaneous field, the use of sectional streamtraces (or streamlines) assumes two-dimensional flow, although the transverse component of the velocity is not necessarily zero. In both cases, the flow is dominated by separation from the leading edge of the free-end, a large clockwise recirculation zone just below the trailing edge of the free-end, and a weak secondary counter-clockwise recirculation zone near the ground plane. For these specific realizations of the instantaneous velocity, the field predicted by the DSM appears to contain multiple localised recirculation zones, while the DNM prediction more closely resembles the time-averaged flow pattern discussed below.

Figures 3.10a) and 3.10b) show time-averaged streamtraces along with transverse (Z) vorticity contours on the symmetry plane (X − Y) as predicted by the DSM and DNM, respectively. The overall topology is similar for both SGS models, consisting of a large primary clockwise recirculation zone located just behind the top of the prism, and a much weaker secondary counter-

a) DSM, time-averaged

b) DNM, time-averaged

c) Zhang *et al* (2017) for AR=4 and Re=1000

Reprinted from [Zhang, D., Cheng, L., An, H., and Zhao, M. (2017). Direct numerical simulation of flow around a surface-mounted finite square cylinder at low Reynolds number. Physics of Fluids, 29 (4)], with the permission of AIP Publishing.
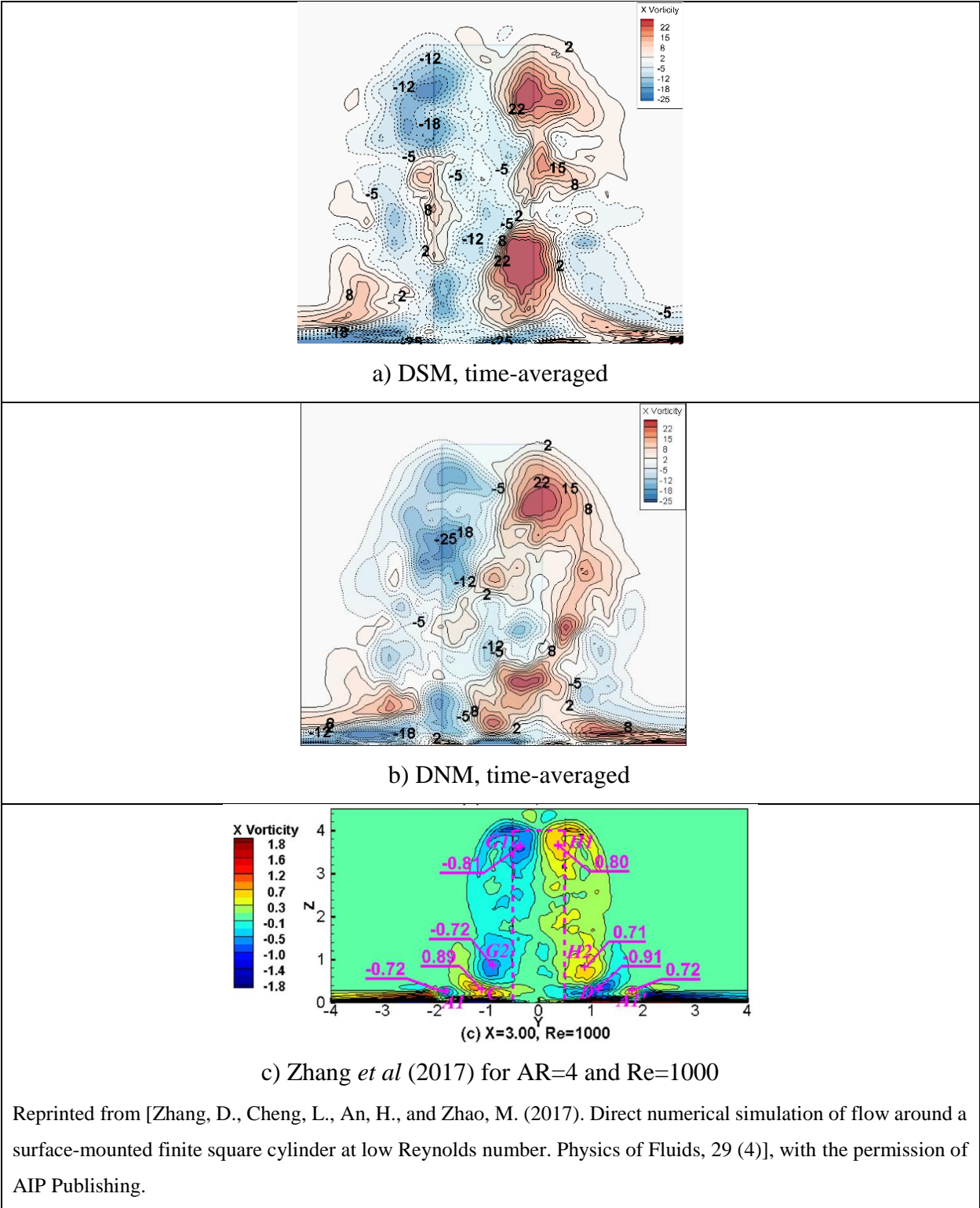
Figure 3.8. Time-averaged streamwise (**X**) vorticity and contour lines in a vertical plane located at X = 3D from the downstream face of the prism as predicted by: a) DSM, b) DNM and c) Zhang *et al* (2017).
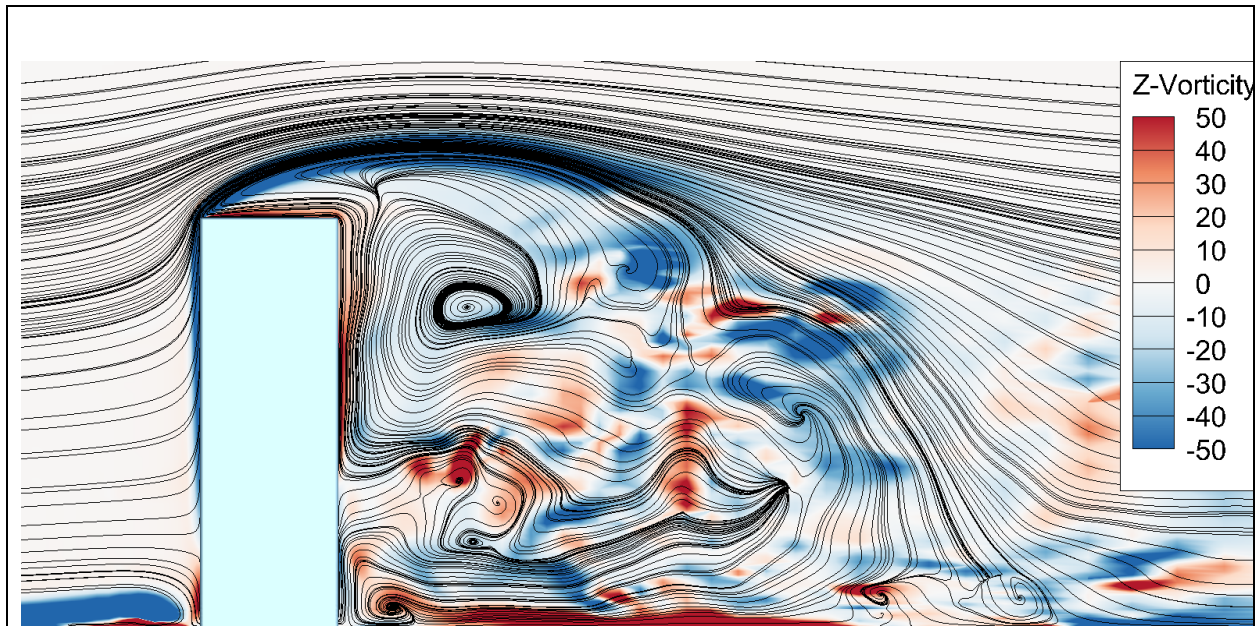
a) DSM, instantaneous
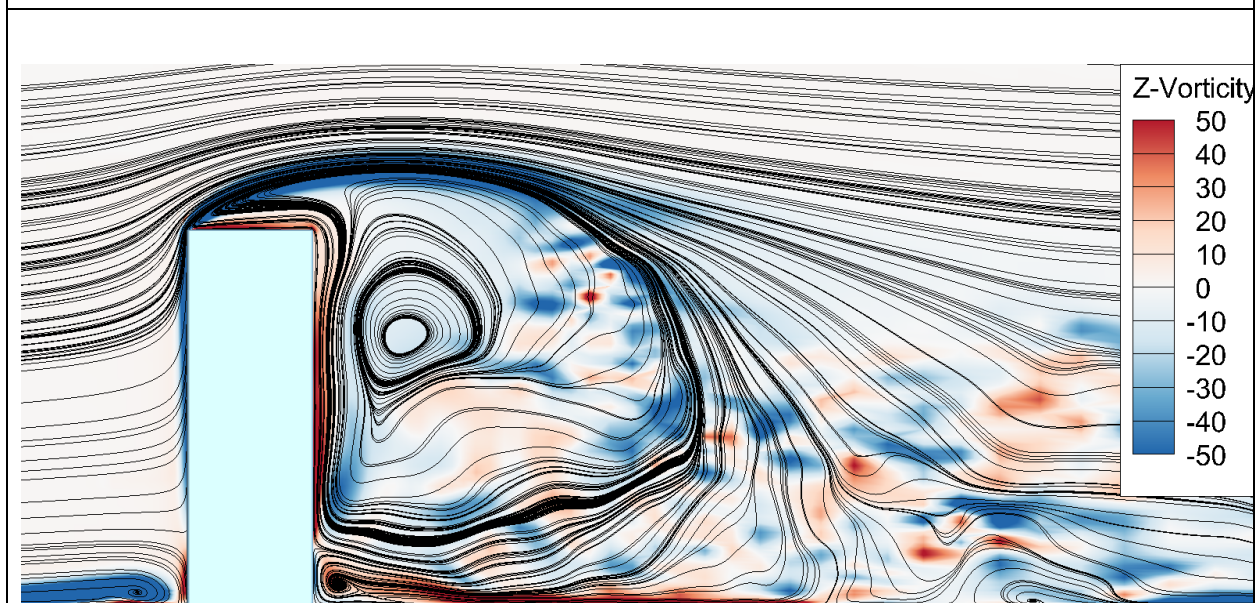
b) DNM, instantaneous

Figure 3.9. Instantaneous transverse ($\mathbf{Z}$) vorticity contours along with streamtraces on the symmetry plane ($\mathbf{X} - \mathbf{Y}$) as predicted by: a) DSM, and b) DNM.

clockwise recirculation zone just above the ground plane. Clear differences in the flow patterns exist, e.g. the shape as defined by the dividing streamtrace is different, and the DSM predicts a more extensive recirculation region compared to the DNM, especially near the ground plane. It is significant to observe distinct differences in the mean vortex structure due to the use of different SGS models.

The extent of the primary vortex in the streamwise direction at mid-height is approximately 2.7D for the DSM compared to 3.0D for the DNM. The focus of the primary recirculation zone is located approximately 1.0D from the prism and 2.3D from the ground plane for the DSM compared to approximately 0.7D from the prism and 2.5D from the ground plane for the DNM. For the same Reynolds number but aspect ratio of AR= 4, Zhang *et al.* (2017) (Figure 3.10c) predicted the location of the focus of the primary vortex to be approximately 2D from the prism and 3D from the ground plane. The location of the secondary vortex for the DSM is approximately 0.3D from the prism and 0.1D from the ground plane, compared to 0.3D from the prism and 0.15D from the ground plane for the DNM. Zhang *et al.* (2017) (Figure 3.10c) predicted the location of the secondary vortex to be approximately 0.5D from the prism and 0.3D from the ground plane. The location of the upstream stagnation point on the prism for the DSM is 0.6D from the ground plane, while the DNM predicts a location of 0.7D. The location of the downstream stagnation point for the DSM is 0.3D from the ground plane, while the DNM predicts a location of 0.6D. Zhang *et al.* (2017) (Figure 3.10c) predicted the location of the upstream stagnation point to be 1D from the ground plane, while the location of the downstream stagnation point was 0.8D. The comparison to Saha shows the significant effect of a lower Re on the wake structure, i.e. the secondary vortex is much larger and higher, as is the rear stagnation point.

As a result of the interaction between the flow at the wall junction and the free-end, a saddle point is formed. Recall that a saddle point occurs when four streamtraces converge at a single point, and is typically observed for the flow behind an obstacle when the flow over the top does not attach directly to the ground plane (Bourgeois *et al* 2011). In this study, the boundary layer was laminar and the thickness was relatively thin, so that the saddle point was located at or very close to the ground plane (Vinuesa *et al.*, 2015). For the DSM, the flow over the top impinged on the ground plane at a distance of 5D from the prism, hence there was no saddle point. For the DNM, the saddle

a) DSM, time-averaged

b) DNM, time-averaged

c) Zhang *et al* (2017) for AR = 4, Re = 500

Reprinted from [Zhang, D., Cheng, L., An, H., and Zhao, M. (2017). Direct numerical simulation of flow around a surface-mounted finite square cylinder at low Reynolds number. Physics of Fluids, 29 (4)], with the permission of AIP Publishing.
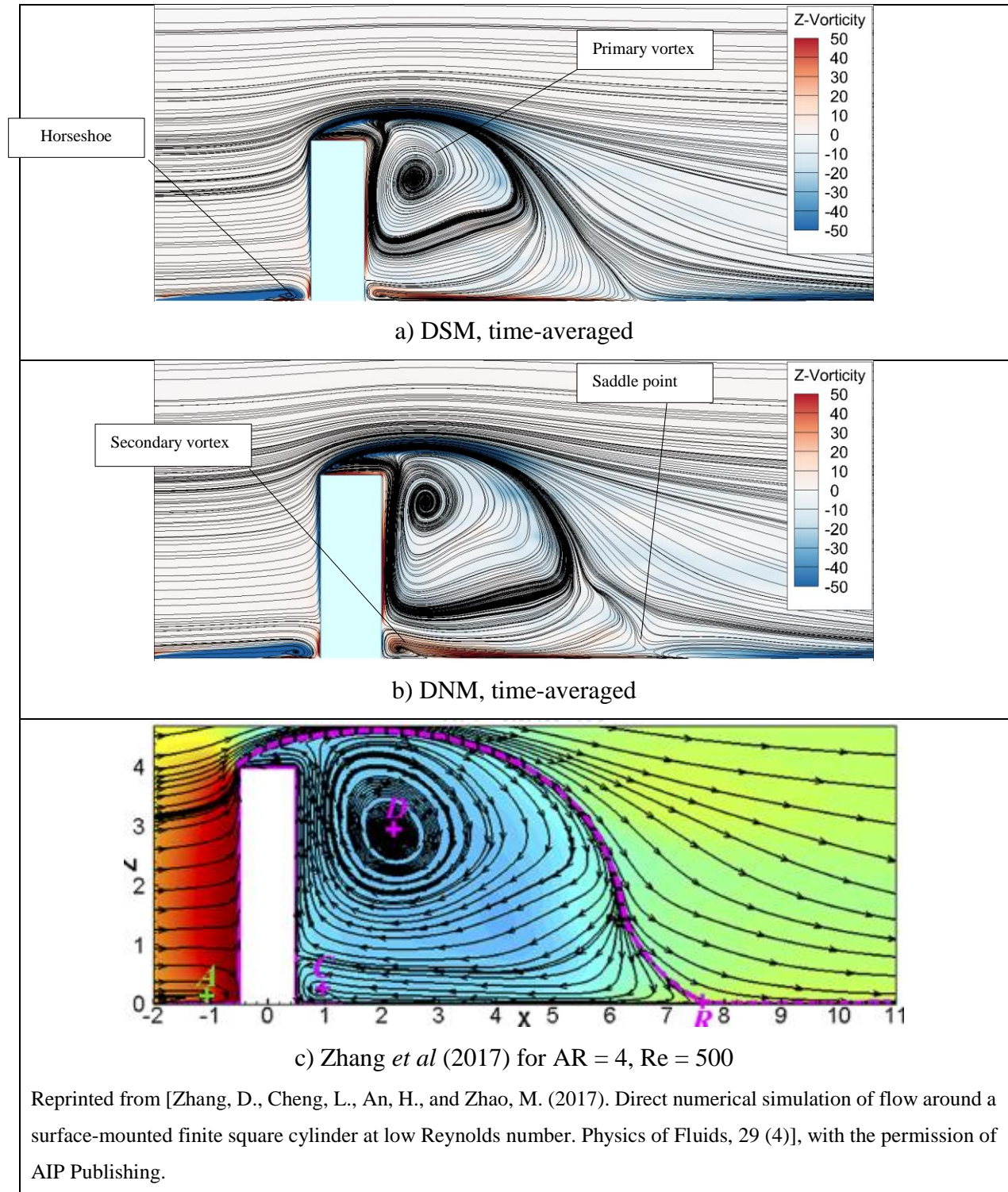
Figure 3.10. Time-averaged transverse (**Z**) vorticity contours along with streamtraces on the symmetry plane (**X** − **Y**) as predicted by: a) DSM, b) DNM, c) Zhang *et al* (2017).

point was located just above the ground plane (0.15D) at a distance of 4.6D from the prism. For the study of Zhang *et al.* (2017) (Figure 3.10c), no clear saddle point is evident in the streamtraces in the wake.

Figures 3.11a) and 3.11b) show the predictions of the two SGS models (DSM and DNM, respectively) for instantaneous streamtraces along with contours of spanwise (Y) vorticity in the horizontal mid-plane of the prism located at $Y = H/2$. Again, for both the instantaneous and mean velocity fields, the wall-normal component is not necessarily zero but likely relatively weak, so the two-dimensionality inferred by the streamtraces is at best an approximation. The instantaneous results for both models show a series of distinct vortices within the shear layers detaching from the front corners of the prism, with recirculation within the near-wake. The streamtrace pattern immediately behind the prism shows some evidence of vortex shedding, as does the asymmetry of the vortices. The vortices shown in Figure 3.11 can be identified with the vertical vortex cores being shed from the prism in the 3D visualization shown in Figure 3.5.

Figures 3.12a) and 3.12b) show time-averaged spanwise (Y) vorticity contours along with streamtraces in the horizontal mid-plane located at $Y = H/2$ as predicted by the DSM and DNM, respectively. The main structure is the same for both SGS models, and consists of a pair of counter-rotating spanwise vortices in an approximately symmetric arrangement. There are noticeable differences in the shape and streamtrace patterns predicted by each SGS model. The streamtraces predicted by the DSM tend to converge beyond the near-wake, whereas they tend to diverge, especially along the centerline, for the DNM. The shape of the recirculation zone predicted by the DNM model is closer to that predicted by Zhang *et al.* (2017) (3.12c) for a prism with aspect ratio $AR = 4$ and $Re = 500$. For both SGS models, saddle points are located at the downstream edge of the recirculation zone, which is 3.5D downstream of the prism for the DSM and 3.1D for the DNM. Although the recirculation zone is longer for the DSM, the centers of the vortices are closer to the prism for the DNM. For comparison, for the $AR = 4$ prism flow simulated by Zhang *et al.* (2017) (3.12c) the corresponding location was approximately 5D. Based on further analysis of additional horizontal planes distributed along the prism height (not shown), the size of the recirculation region becomes smaller with height and finally disappears just above the free-end of the prism. This observation is consistent with previous studies for higher Reynolds number flows such as
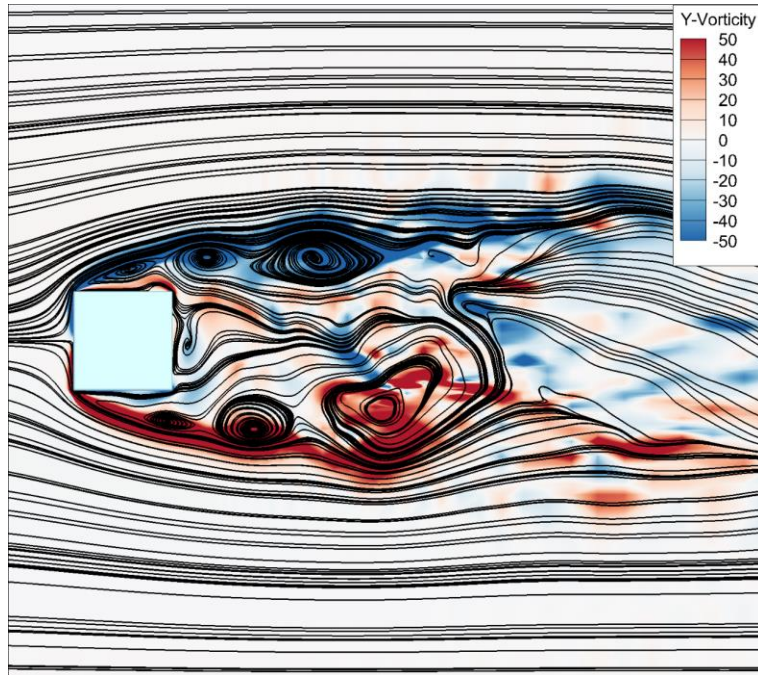
a) DSM, instantaneous
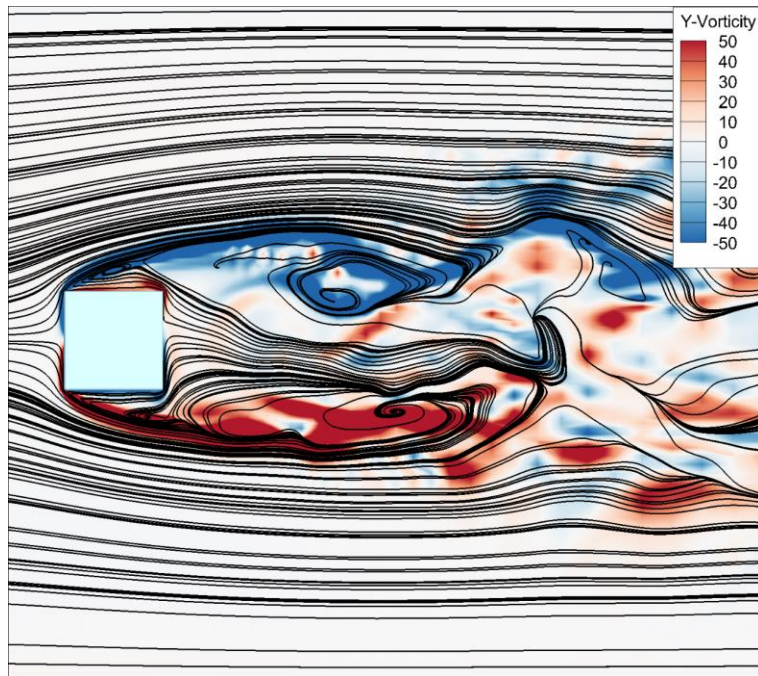
b) DNM, instantaneous

Figure 3.11. Instantaneous streamtraces and spanwise (**Y**) vorticity contours in the horizontal mid-plane located at Y = H/2 as predicted by: a) DSM, and b) DNM.

a) DSM, time-averaged

b) DNM, time-averaged

c) Zhang *et al* (2017) for AR=4 and Re=500

Reprinted from [Zhang, D., Cheng, L., An, H., and Zhao, M. (2017). Direct numerical simulation of flow around a surface-mounted finite square cylinder at low Reynolds number. Physics of Fluids, 29 (4)], with the permission of AIP Publishing.
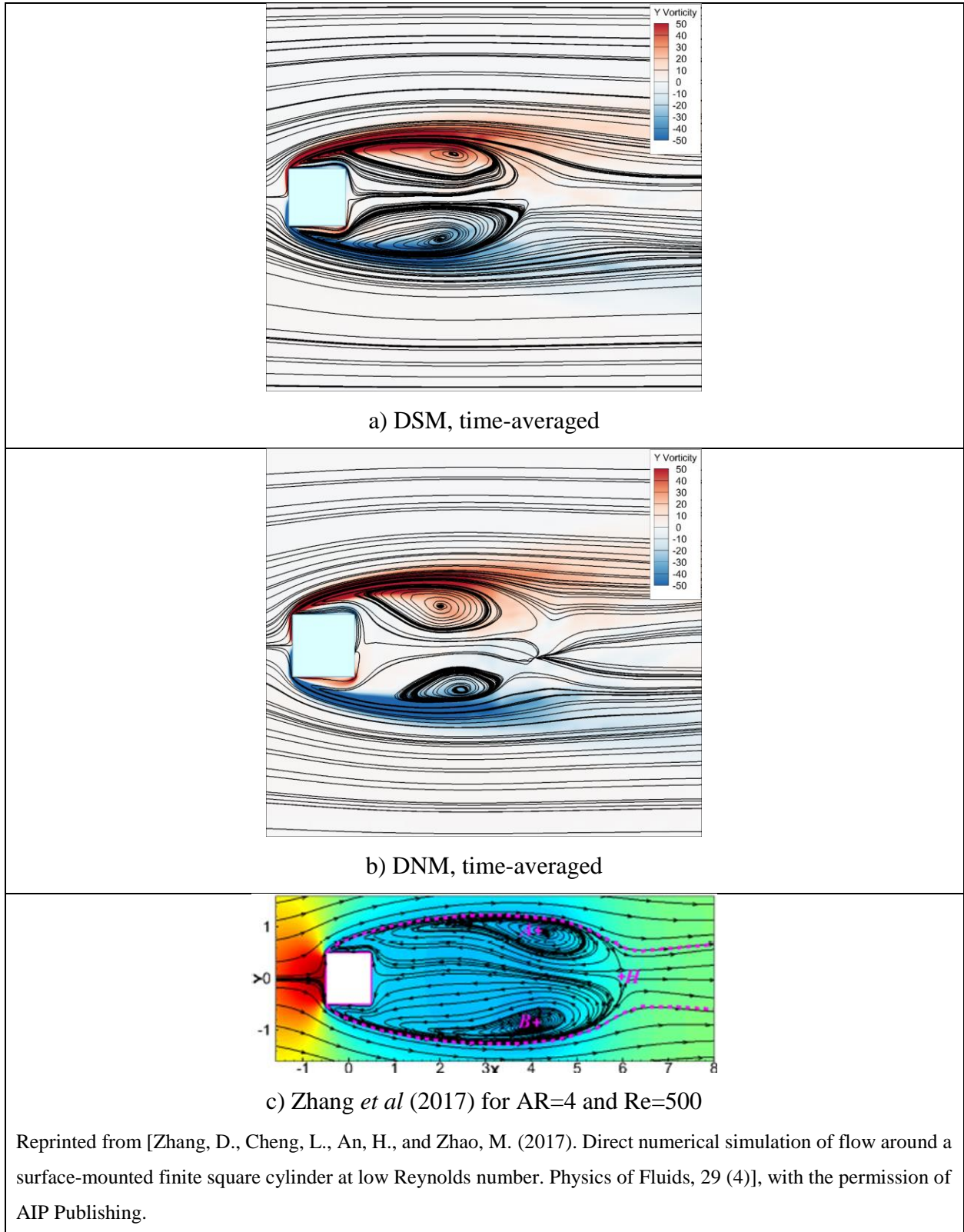
Figure 3.12. Time-averaged streamtraces and spanwise (**Y**) vorticity contours in the horizontal mid-plane located at Y = H/2 as predicted by: a) DSM, b) DNM, and c) Zhang *et al* (2017).

Bourgeois *et al.* (2011) and Sattari *et al.* (2012). Overall, the LES predicted similar mean flow structures to those documented by the DNS studies.
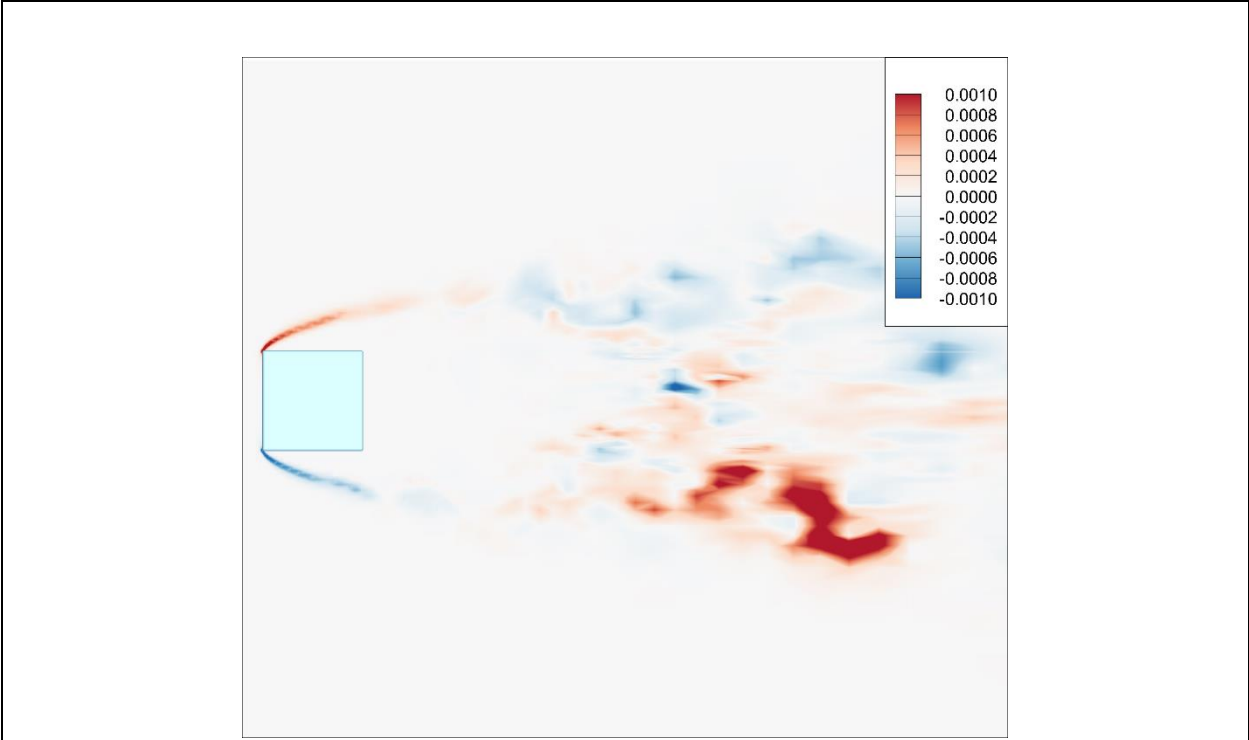
3.4.2 SGS stress tensor

The analysis above has focused on a comparison of the velocity fields (instantaneous and time-average) predicted by the two SGS models. A more direct comparison of the two SGS models relates to the predictions for the SGS stress tensor itself. Figures 3.13a) and 3.13b) show instantaneous values of the SGS shear stress component (τ_{xz}) in the horizontal mid-plane located at Y = H/2 as predicted by the DSM and DNM, respectively. The mean velocity fields in this plane are shown in Figure 3.12. In Figure 3.13, as well as the other contour plots presented in sections 4.2 and 4.3, the range of contour values is selected to maximise the visual contrast and hence readability. Using this approach, any peak values that exceed the limits, are shown with the color of the limiting contour value. In order to provide a more precise description, the peak values are also given. The SGS stress is most significant in the region of the shear layers separating from the upstream corners of the prism, as well as the mixing region downstream of the recirculation zone. There is minimal SGS stress in the region just behind the prism, which is explained by the relatively low velocities and weak gradients in this region of reverse flow. For the instantaneous fields, the stress is more pronounced for the DNM in the shear layer near the location of separation. In the mixing region, the DSM evidences a distribution of both negative and positive peak values, whereas the peak values predicted by the DNM are generally lower and concentrated in a few local regions. The maximum and minimum peak values for the DSM and DNM are as follows: 0.007 and -0.01 for the DSM, and 0.003 and -0.003 for the DNM. For this instantaneous realization of the flow, the DNM predicts significantly lower peak values.

Figures 3.14a) and 3.14b) show the time-averaged value of the SGS shear stress (τ_{xz}) in the horizontal mid-plane at Y = H/2 as predicted by the DSM and DNM, respectively. Both SGS models predict similar and symmetric distributions, however there are some significant differences relating to the magnitude of the local stress. The DSM predicts peak values on the upstream face of the prism and for an extensive region located in the mixing region. In contrast, the DNM predicts
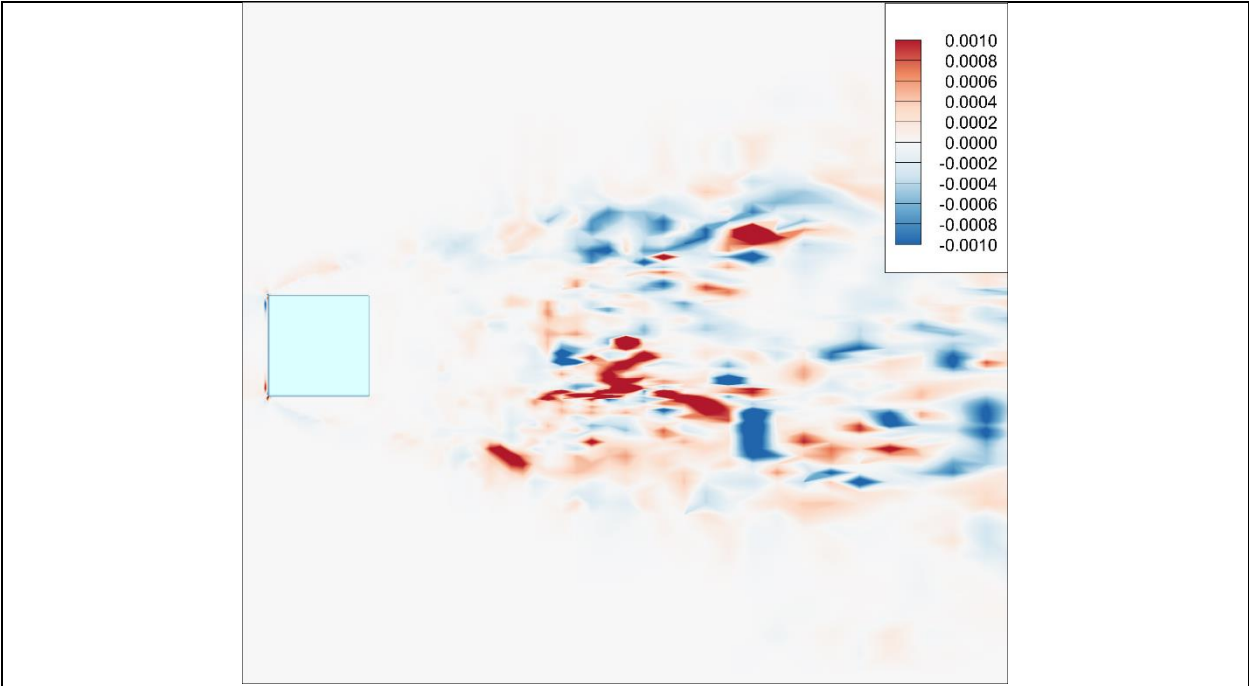
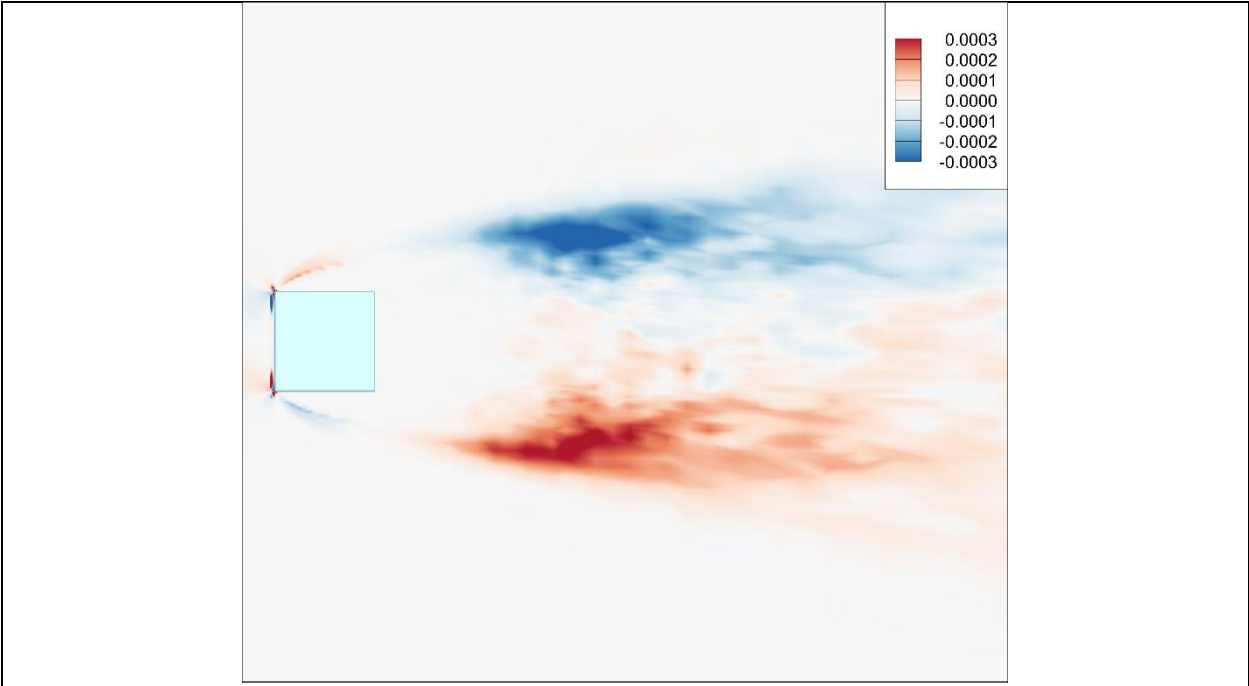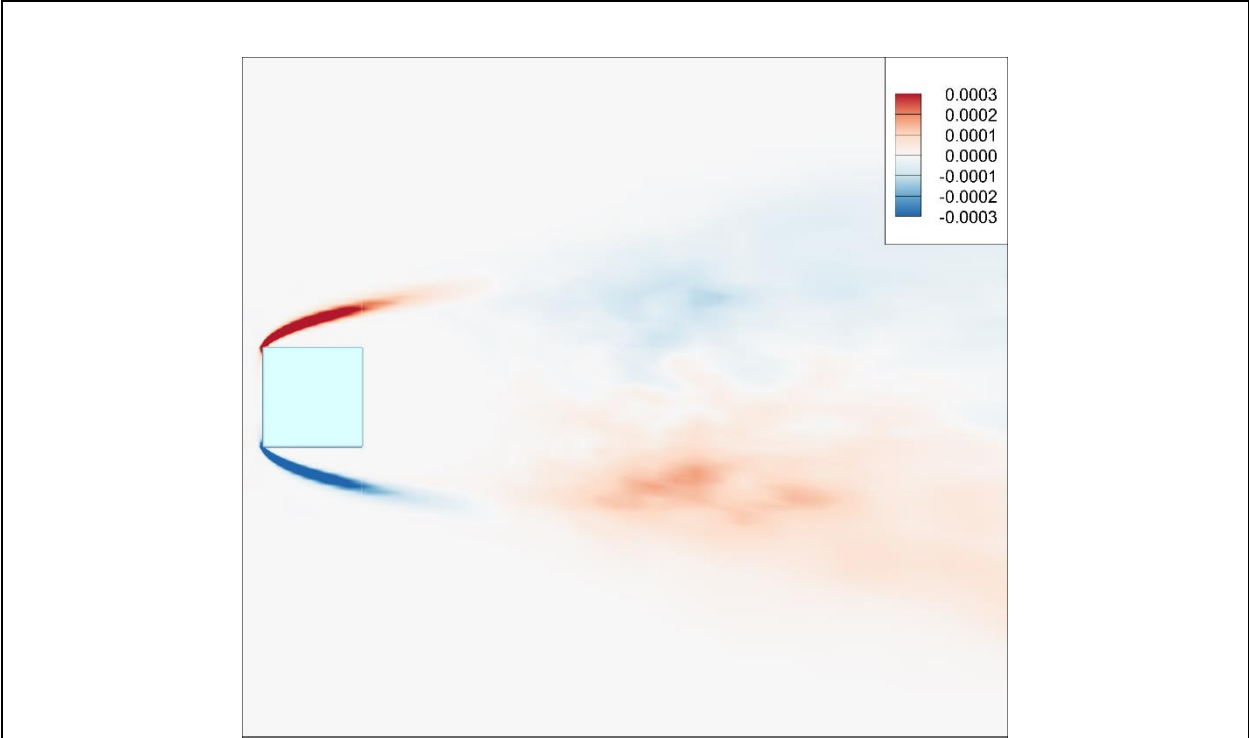a) DSM, instantaneous

b) DNM, instantaneous

Figure 3.13. Instantaneous values of SGS stress tensor (τ_{xz}) in the horizontal mid-plane located at Y = H/2 as predicted by: a) DSM, and b) DNM.

a) DSM, time-averaged


b) DNM, time-averaged

Figure 3.14. Time-averaged values of SGS stress tensor (τ_{xz}) in the horizontal mid-plane located at $Y = H/2$ as predicted by: a) DSM, and b) DNM

peak values in the initial region of the shear layers separating from the upstream edges of the prism; the values in the mixing region are relatively low. For comparison, the maximum and minimum peak values for the DSM and DNM are as follows: 0.004 and -0.003 for the DSM, and 0.003 and -0.003 for the DNM.

3.4.3 SGS energy transfers

Recall that the interaction of the SGS stress and the strain-rate field results in a transfer of turbulence kinetic energy from the resolved scales to the unresolved scales, which is given by the quantity $\mathcal{E}_{SGS} = -\tau_{ij}^{*}\bar{S}_{ij}$, which is nominally referred to as the SGS dissipation of turbulence kinetic energy. Forward-scatter is shown by positive values of $\mathcal{E}_{SGS}$, while backscatter is indicated by negative values. Recall that backscatter is associated with the transfer of energy from the subgrid to the resolved scales. Figures 3.15a) and 3.15b) show the instantaneous values of $\mathcal{E}_{SGS}$ as predicted by the DSM and DNM, respectively, in the horizontal mid-plane at Y = H/2. The SGS dissipation as predicted by the DSM shows significant regions of backscatter in the initial region of the separating shear layers and in the mixing region downstream of the prism; in contrast, the DNM predicts much less backscatter. This is consistent with previous studies that indicate the prediction of backscatter by the DNM is more controlled and does not lead to numerical instabilities (Einian 2012). In the mixing region, the DSM predicts peak values of the SGS dissipation of turbulent kinetic energy that are nearly four times larger than those predicted by the DNM. Note that the level of the SGS dissipation of turbulent kinetic energy depends on the magnitude of the the SGS stress tensor. Figure 3.14 indicates that the level of the SGS shear stress is generally lower for the DNM, which is consistent with the lower levels shown for the SGS dissipation of turbulence kinetic energy predicted by the DNM.

Figure 3.16 compares the DSM and DNM predictions for the instantaneous SGS dissipation of turbulence kinetic energy along a line section located at X = 3D and Y = H/2 as indicated on Figure 3.15. Comparison of the peak values for the two SGS models shows significant differences. The
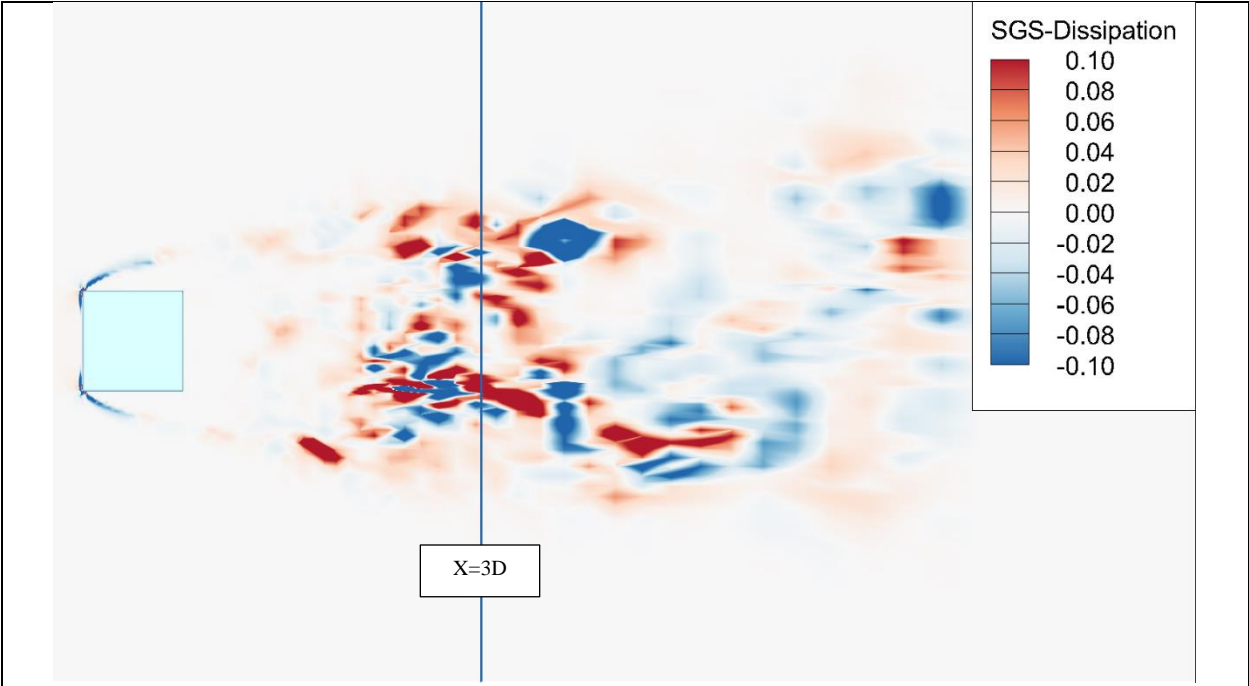
a) DSM, instantaneous
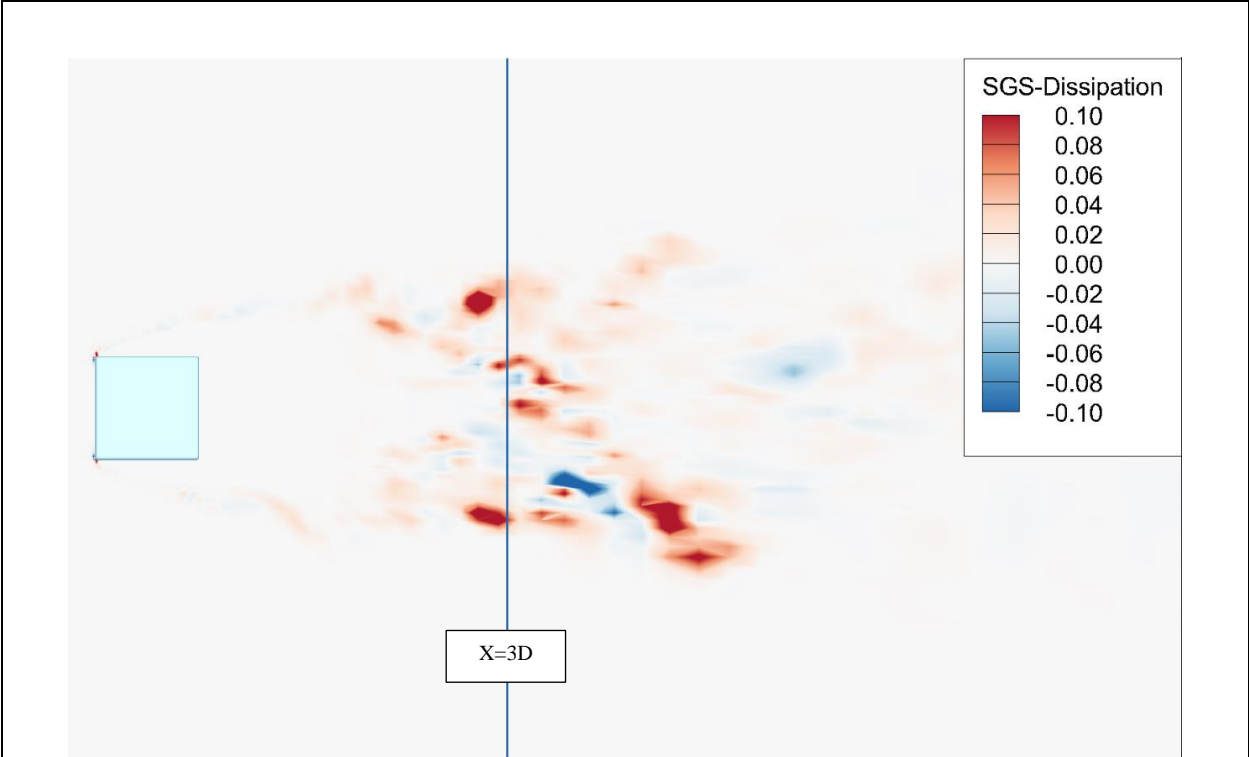
b) DNM, instantaneous

Figure 3.15. Instantaneous SGS dissipation of turbulence kinetic energy in the horizontal mid-plane located at Y = H/2 as predicted by: a) DSM, and b) DNM.

68

peak positive value predicted by the DNM is approximately $\mathcal{E}_{SGS} = 0.2$ compared to $\mathcal{E}_{SGS} = 0.60$ for the DSM. The peak negative value predicted by the DNM is approximately $\mathcal{E}_{SGS} = -0.03$ compared to $\mathcal{E}_{SGS} = -0.35$ for the DSM. The magnitude of the backscatter predicted by the DNM is relatively small compared to the DSM. Furthermore, the DSM frequently predicts local regions where the value of the SGS dissipation rapidly changes from large negative to large positive values (or vice versa.) The results in Figure 3.16 imply that even with the use of clipping and volume-averaging to stabilize the DSM, local extreme values of the eddy viscosity are present. This in turn creates large values of forward- and backscatter in local regions of the flow.
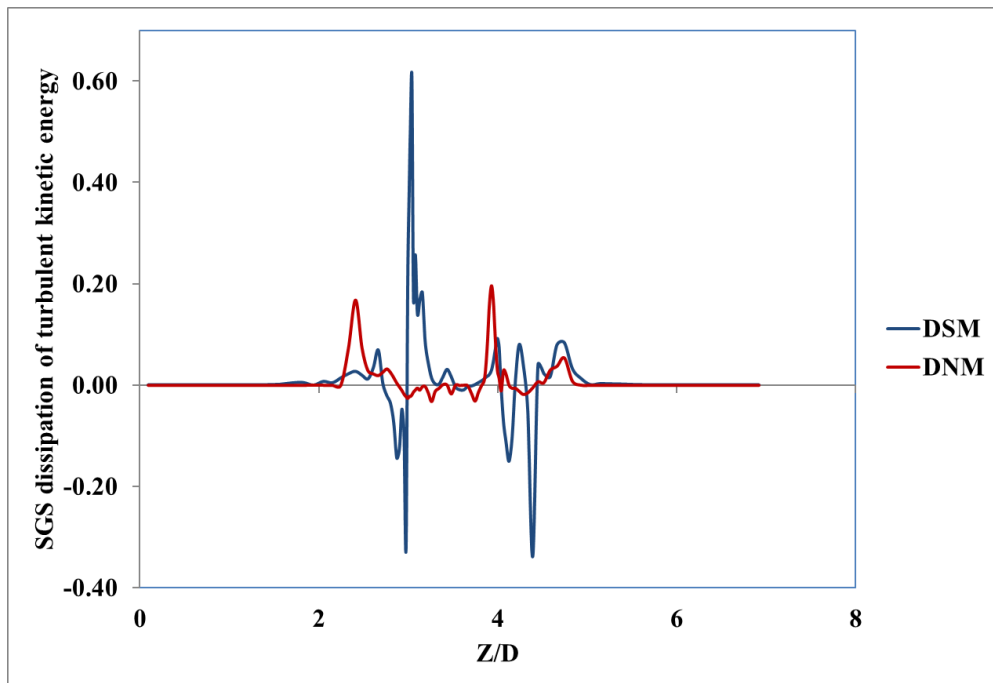
Figure 3.16. Instantaneous SGS dissipation of turbulence kinetic energy along the line
X = 3D and Y = H/2 as predicted by: a) DSM, and b) DNM.

Figures 3.17a) and 3.17b) show the instantaneous resolved dissipation of turbulence kinetic energy given by $2\nu\bar{S}_{ij}\bar{S}_{ij}$, in the horizontal mid-plane as predicted by the DSM and DNM, respectively. Based on the instantaneous results predicted by both SGS models, the peak values of the dissipation occur near the upstream edge of the prism, within the separating shear layers and in the mixing region where these shear layers interact. In the near-wake region, the DNM predicts a higher maximum value of the resolved dissipation of turbulence kinetic energy (approximately

69

a) DSM, instantaneous

b) DNM, instantaneous

Figure 3.17. Instantaneous resolved dissipation of turbulence kinetic energy in the horizontal mid-plane located at Y = H/2 as predicted by: a) DSM, and b) DNM.

1.2) compared to the DSM (approximately 0.2). In general, the DNM results are characterised by a much larger resolved-scale dissipation, which can be explained by the fact that this SGS model produces a finer-scale structure for the resolved scale field.

Figure 3.18 shows the instantaneous resolved dissipation of turbulence kinetic energy on a line section located at $X = 3D$ and $Y = H/2$ in the near-wake (indicated in Figure 3.17) as predicted by the DSM and DNM. This figure shows a distinct difference in the peak values of the resolved dissipation: the peak value of approximately 0.15 for the DSM is much less than the peak value of 1.0 for the DNM. The much larger values of resolved-scale dissipation obtained by the DNM relates to the fact that the DNM preserves a finer scale structure at the grid-scale, since it does not use the smoothing mechanism adopted to stabilize the DSM.
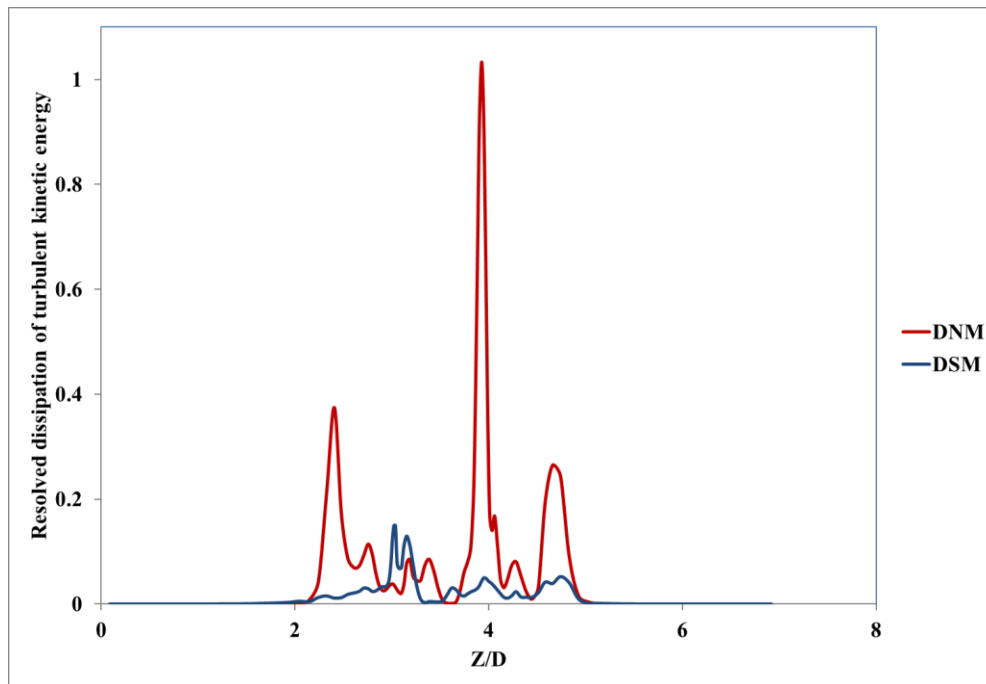
Figure 3.18. Instantaneous resolved dissipation of turbulence kinetic energy along a line section located at $X = 3D$ and $Y = H/2$ as predicted by the DSM and DNM.

Figures 3.19a) and 3.19b) show the total time-averaged dissipation of turbulence kinetic energy in the horizontal mid-plane located at $Y = H/2$ as predicted by the DSM and DNM, respectively. The values predicted by the DSM range between -0.6 and 5, while the values predicted for the DNM

71
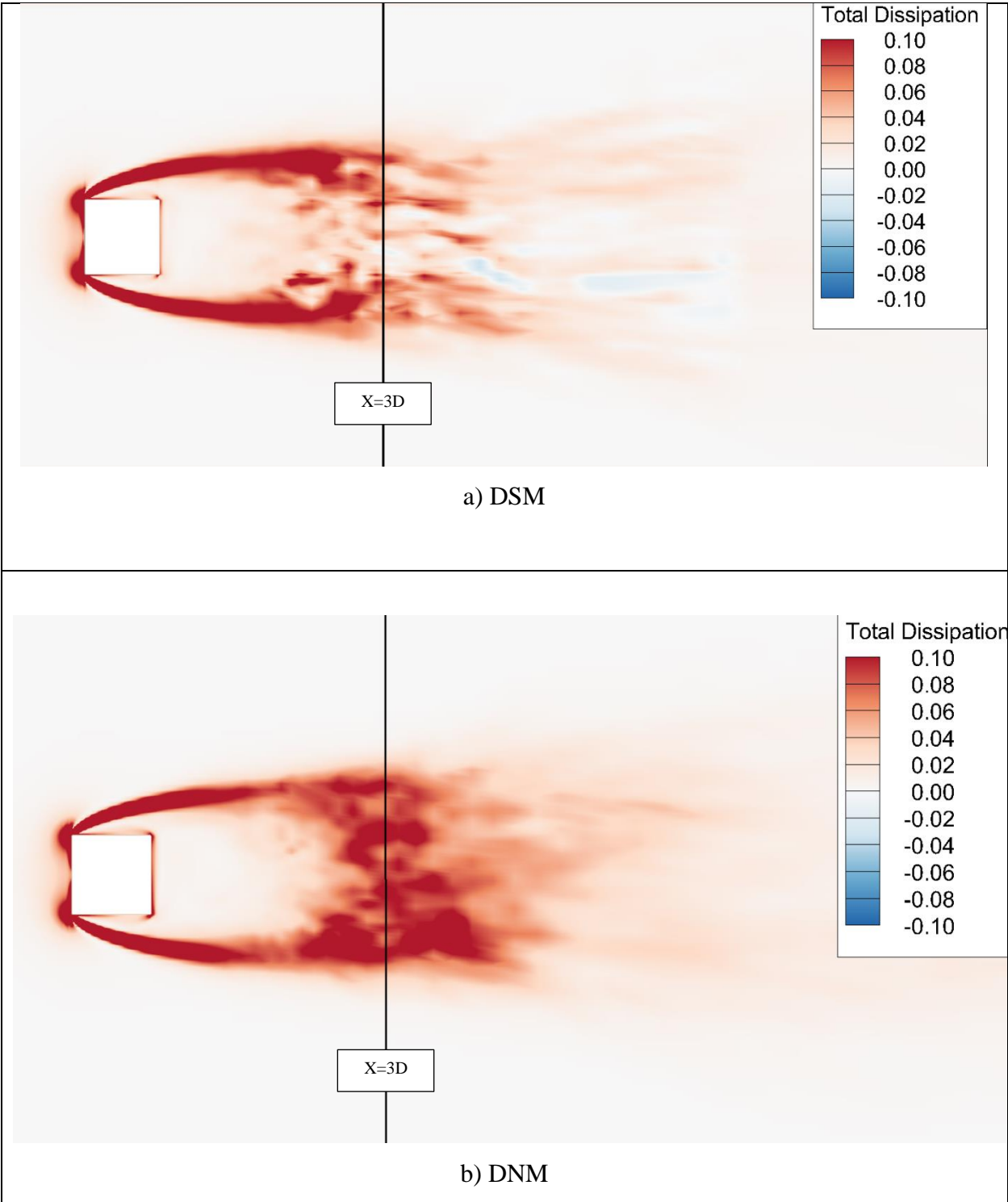
a) DSM

b) DNM

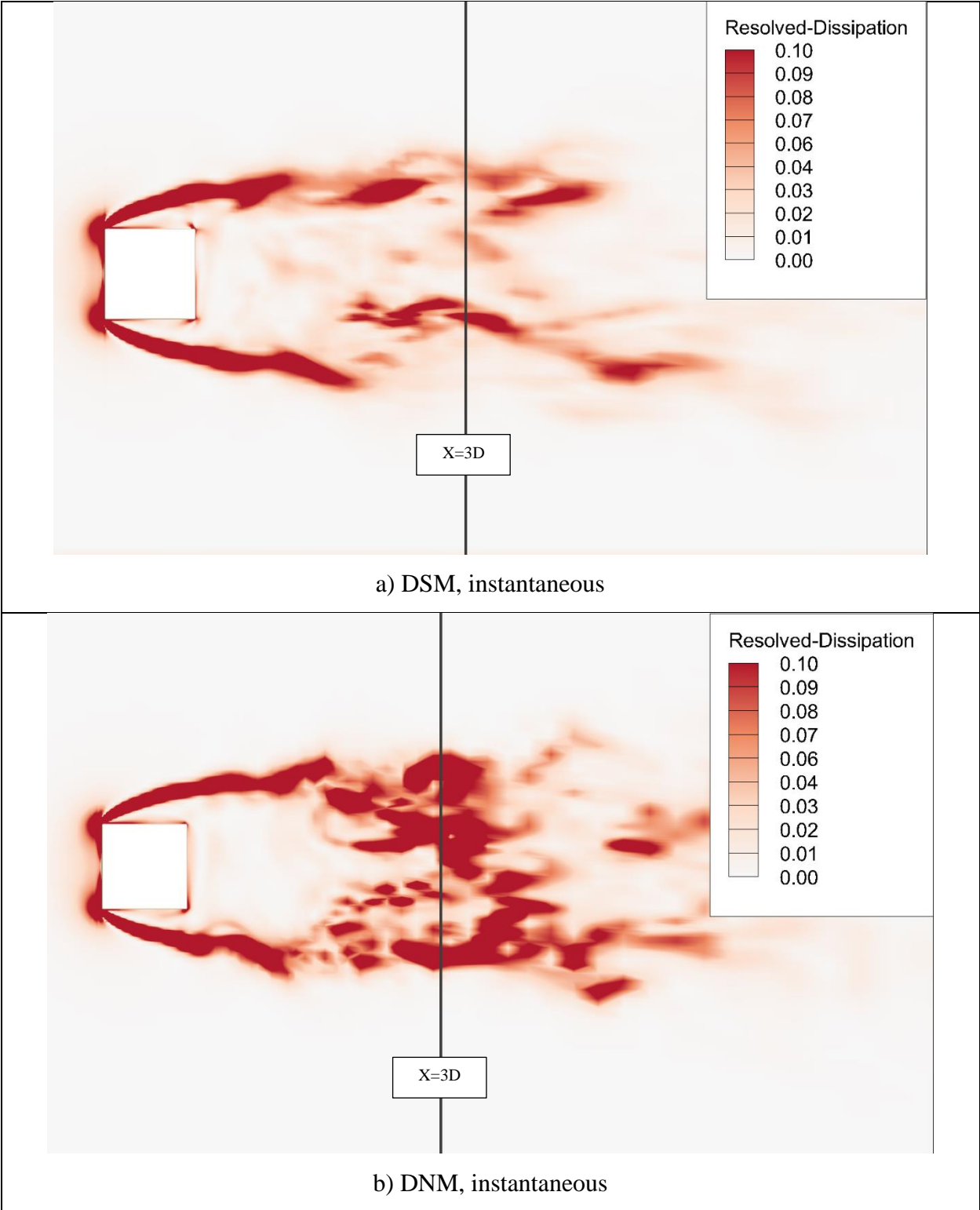Figure 3.19. Time-averaged total dissipation of turbulence kinetic energy in the horizontal mid-plane located at Y = H/2 as predicted by: a) DSM, and b) DNM.

range between 0 and 10. Somewhat surprisingly, the DSM shows a few local regions of relatively weak backscatter in the time-averaged field, which may be due to the limited ensemble size (four seconds) used for time-averaging. Since the DNM captures finer-scale structures, the amount of total dissipation of turbulence kinetic energy is considerably larger than that predicted by the DSM.

Figure 3.20 shows the total time-averaged dissipation of turbulence kinetic energy on a line section located at X = 3D and Y = H/2 as predicted by the DSM and DNM. As shown in the figure, the DNM predicts a slightly higher and more uniform value for the total dissipation. Although the DSM predicts a higher SGS dissipation while the DNM predicts a higher resolved-scale dissipation, when both contributions are combined, the DNM is found to predict a larger value for the total dissipation. The DSM is also observed to predict local regions of suppressed dissipation and even small negative values implying the local dominance of backscatter.
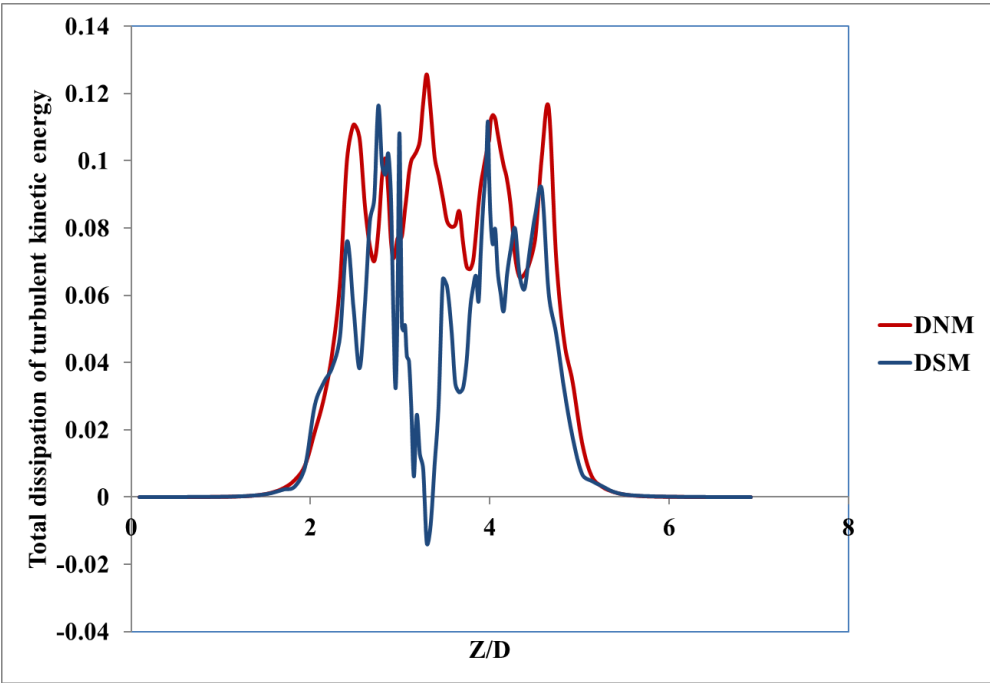

Figure 3.20. Time-averaged total dissipation of turbulence kinetic energy along a line section at X = 3D and Y = H/2 as predicted by the DSM and DNM.

3.5 Conclusion

LES predictions of low Reynolds number flow over a finite-height square prism mounted on a ground plane are presented based on linear (DSM) and nonlinear (DNM) dynamic SGS models. The velocity field predicted for this sub-critical aspect ratio of AR = 3 reveals a complex wake structure with periodic behaviour associated with vortex shedding from the sides of the prism. Although the velocity fields predicted by the two different SGS models are similar in many ways, there are also notable differences in both the instantaneous and mean velocity fields. For example, it is surprising to see that the SGS model affects the shape and extent of the recirculation patterns in the near-wake on both the vertical and horizontal mid-planes. For the same grid the DNM predicts a noticeably finer-scale structure compared to the DSM (as shown and discussed in Figure 3.5 for the 3D vortex structures). This is caused by the stabilization technique used for the DSM, i.e. volume-averaging and then clipping the dynamic model coefficient. In contrast, the DNM does not use any stabilizing procedure. This is a clear advantage of the DNM is the fact that there is no need for a stabilization technique that in the case of the DSM arbitrarily modifies the coefficients and hence SGS viscosity.

Although overall the predictions for the mean field were very similar for both SGS models, there are some small differences which suggest that the prediction of the DNM is more realistic. For example, in Figure 3.10 the prediction for the time-averaged streamtraces and transverse vorticity in the symmetry plane for the DNM were more similar to those of Zhang *et al.* (2017). Likewise, in the Figure 3.12, the shape of the recirculation zone predicted by the DNM model is closer to that predicted by Zhang *et al.* (2017) based on the time-averaged streamtraces in the horizontal mid-plane. A more definitive assessment of the SGS models would require comparison to a DNS solution for the same aspect ratio and Reynolds number, which was not presently available.

The comparison shows closer outcomes predicted by DNM in current study to Zhang et al (2017) (as shown and discussed in Figure 3.10 for time-averaged streamtraces along with transverse (Z) vorticity contours on the symmetry plane). As shown in the Figure 3.12, the shape of the recirculation zone predicted by the DNM model is closer to that predicted by Zhang et al. (2017) for time-averaged spanwise (Y) vorticity contours along with streamtraces in the horizontal mid-plane.

Even when the DSM is stabilized, it produces a large amount of backscatter, as shown in the Figures 15 and 16 for the SGS dissipation of turbulence kinetic energy. In contrast, the DNM predicts much less backscatter and instead is characterized by a much larger resolved-scale dissipation (see Figures 3.17 and 3.18. for the resolved scale dissipation of turbulence kinetic energy). This relates to the fact that the DNM preserves a finer-scale structure at the grid-scale and better capture the flow structures.

Recall from the paper by Wang and Bergstrom (2005), one of the compelling arguments in favor of the DNM was that, following RANS modeling, the constitutive relation is much more comprehensive and realistic than the eddy viscosity model formulation used by the DSM. This explains some significant differences in the magnitude and distribution of the SGS stress obtained for the two different SGS models. For the SGS shear stress in the horizontal mid-plane, the DSM predicts the peak values to occur on the upstream face of the prism and for an extensive region located in the shear layers bounding the mixing region (about 3D downstream of the prism). In contrast, the DNM predicts peak values in the initial region of the shear layers separating from the upstream edges of the prism; the values in the mixing region are relatively small.

The present study is one of the first to critically assess the performance of linear and nonlinear dynamic SGS models in a relatively complex flow. Based on the argument given above, it concludes that the DNM is a more realistic model formulation compared to the DSM. Typically, the SGS energy and momentum are relatively small for low Reynolds number flows. If there are noticeable difference in the velocity fields predicted by the two different SGS models in this study for Re = 500, then one would expect these differences to become more significant at higher Reynolds numbers where the resolution of the smallest scales becomes more challenging and the relative level of SGS energy increases.

3.6 Acknowledgements

75

3.7 References

Baya Toda, H., Cabrit, O., Truffin, K., Bruneaux, G., and Nicoud, F. (2014). Assessment of subgrid-scale models with a large-eddy simulation-dedicated experimental database: The pulsatile impinging jet in turbulent cross-flow. *Physics of Fluids, 26* (7), 075108. DOI: 10.1063/1.4890855

Basu, S. and Porté-Agel, F. (2006). Large-eddy simulation of stably stratified atmospheric boundary layer turbulence: a scale-dependent dynamic modeling approach. *Journal of the Atmospheric Sciences, 63*, 2074. DOI: 10.1175/JAS3734.1

Bourgeois, J. A., Sattari, P., and Martinuzzi, R. J. (2011). Alternating half-loop shedding in the turbulent wake of a finite surface-mounted square cylinder with a thin boundary layer. *Physics of Fluids, 23* (9), 095101. DOI: 10.1063/1.3623463

Dubief, Y. and Delcayre, F. (2000). On coherent-vortex identification in turbulence. *Journal of Turbulence, 1*, 011. DOI: 10.1088/1468-5248/1/1/011

Germano, M., Piomelli, U., Moin, P., and Cabot, W. H. (1991). A dynamic subgrid-scale eddy viscosity model. *Physics of Fluids A: Fluid Dynamics, 3* (7), 1760-1765. DOI: 10.1063/1.857955

Heinz, S. (2008). Realizability of dynamic subgrid-scale stress models via stochastic analysis. *Monte Carlo Methods and Applications, 14* (4). DOI: 10.1515/MCMA.2008.014

Heinz, S. and Gopalan, H. (2012). Realizable versus non-realizable dynamic subgrid-scale stress models. *Physics of Fluids, 24*, 115105. DOI: 10.1063/1.4767538

Heinz, S., Gopalan, H., Foroushani, E. K., Stoellinger, M. K., Mokhtarpoor, R., and Balakumar, P. (2015). Realizable dynamic LES subgrid-scale modeling. Proceedings of *9th International Symposium on Turbulence and Shear Flow Phenomena (TSFP-9).* Melbourne, Australia, June 30 - July 3, 2015.

Jeong, J. and Hussain, F. (1995). On the identification of a vortex. *Journal of Fluid Mechanics, 285*, 69-94. DOI: 10.1017/S0022112095000462

Kappler, M., (2002). Experimentelle Untersuchung der Umstr€omung von Kreiszylindern mit ausgepr€agt dreidimensionalen Effekten. Ph.D. thesis, Institute for Hydromechanics, University of Karlsruhe.

Leonard, A. (1974). Energy cascade in large-eddy simulations of turbulent fluid flows. *Advances in Geophysics, 18* (A), 237-248. DOI: 10.1016/S0065-2687(08)60464-1

Lilly, D. K. (1992). A proposed modification of Germano subgrid-scale closure method. *Physics of Fluids A: Fluid Dynamics, 4* (3), 633-635. DOI: 10.1063/1.858280

Meneveau, C. and Katz, J. (2000). Scale-invariance and turbulence models for large eddy simulation. *Annual Review of Fluid Mechanics, 32*, 1-32. DOI: 10.1146/annurev.fluid.32.1.1

Meneveau, C., Lund, T. S., and Cabot, W. H. (1996). A Lagrangian dynamic subgrid-scale model of turbulence. *Journal of Fluid Mechanics, 319*, 353-385. DOI: 10.1017/S0022112096007379

Sagaut, P. (2002). Large eddy simulation for incompressible flows: an introduction. Berlin, Germany: *Springer.*

Saha, A. K. (2013). Unsteady flow past a finite square cylinder mounted on a wall at low Reynolds number. *Computers and Fluids, 88*, 599-615. DOI: 10.1016/j.compfluid.2013.10.010

Sattari, P., Bourgeois, J. A., and Martinuzzi, R. J. (2012). On the vortex dynamics in the wake of a finite surface-mounted square cylinder. *Experiments in Fluids, 52* (5), 1149-1167. DOI: 10.1007/s00348-011-1244-6

Smagorinsky, J. (1963). General circulation experiments with the primitive equations: I. The basic experiment, *Monthly Weather Review, 91*, 99-164. DOI: 10.1175/1520-0493(1963)091<0099:GCEWTP>2.3.CO;2

Sohankar, A., Davidson, L., and Norberg, C. (1999). Large eddy simulation of flow past a square cylinder: Comparison of different subgrid scale models. *ASME Journal of Fluids Engineering, 122* (1), 39-47. DOI: 10.1115/1.483224

Tran, S. and Sahni, O. (2017). Finite element-based large eddy simulation using a combination of the variational multiscale method and the dynamic Smagorinsky model. *Journal of Turbulence, 18* (5), 391-417. DOI: 10.1080/14685248.2017.1280607

Vinuesa, R., Schlatter, P., Malm, J., Mavriplis, C., and Henningson, D. S. (2015). Direct numerical simulation of the flow around a wall-mounted square cylinder under various inflow conditions. *Journal of Turbulence, 16* (6), 555-587. DOI: 10.1080/14685248.2014.989232

Wang, B. C. and Bergstrom, D. J. (2005). A dynamic nonlinear subgrid-scale stress model. *Physics of Fluids, 17 (3)*, 035109. DOI: 10.1063/1.1858511

Wang, H. F. and Zhou, Y. (2009). The finite-length square cylinder near wake. *Journal of Fluid Mechanics, 638*, 453-490. DOI: 10.1017/S0022112009990693

Zhang, D., Cheng, L., An, H., and Zhao, M. (2017). Direct numerical simulation of flow around a surface-mounted finite square cylinder at low Reynolds number. *Physics of Fluids, 29* (4), 045101. DOI: 10.1063/1.4979479

Chapter 4

Periodic Motion in the Wake of a Finite Square Prism as Predicted by Large Eddy Simulation

A similar version of this chapter has been submitted as:

N. Moazamigoodarzi and D.J. Bergstrom, "Periodic Motion in the Wake of a Finite Square Prism as Predicted by Large Eddy Simulation", *Journal of Flow, Turbulence and Combustion*.

In addition, a part of this chapter was presented at the following conferences:

N. Moazamigoodarzi and D.J. Bergstrom, "Periodic Motion in the Wake of a Finite Square Cylinder as Predicted by Large Eddy Simulation", *22nd Annual Conference CFD Society of Canada,* Toronto, Canada, 1-4 June 2014.

N. Moazamigoodarzi, D.J. Bergstrom and D. Sumner, "Flow Structure on the Symmetry Plane of the Wake of a Finite-Height Square Cylinder Based on LES", *14th European Turbulence Conference*, ENS Lyon, France, 1-4 September 2013.

Preamble

The fourth chapter of this thesis reports a large eddy simulation (LES) using a dynamic nonlinear subgrid-scale model with a focus on phase-averaging based on the dominant frequency.

The current chapter contributes to the second objective of this thesis (described in Section 1.2.2), which investigates the periodic structure of the wake of a finite-height square prism.

The current chapter forms a major part of the fourth contribution of this thesis (described in Section 1.3.4), which is to perform a phase-averaged decomposition of the flow in the near-wake for the dynamic nonlinear model (DNM).

In this context, LES with DNM is used to predict the flow structure over a finite-height square prism mounted normally on a ground plane, with an aspect ratio of 3 (AR = H/D, where H is the cylinder height and D is the cylinder width) and a Reynolds number of 500, based on the cylinder width and freestream velocity. The inflow is laminar, with a boundary layer that is relatively thin $\delta/D \approx 0.2$, where δ is the boundary layer thickness). Visualization based on the second invariant and phase-averaging were implemented to better understand the underlying flow mechanisms and structure. The periodic frequency was calculated and used to perform phase-averaging based on five cycles and five phases. Specifically, phase-averaging shows larger-scale structures removed by time-averaging and not fully visible in the instantaneous data. Phase-averaging based on the Strouhal number reveals a wake structure with quasi-periodic features that is much different from the structure suggested by the mean velocity field.

Abstract

The current paper reports a Large Eddy Simulation (LES) of turbulent flow over a finite-height square prism mounted normal to a ground plane. The prism aspect ratio is $AR = 3$ and the Reynolds number based on the prism width and inlet velocity is $Re = 500$. The prism is immersed in a uniform freestream flow, which creates a thin laminar boundary layer on the ground plane. The LES uses a dynamic nonlinear subgrid-scale model. The near-wake structure is dominated by the shear layers being shed from the two sides and top wall of the prism, and their reconfiguration as vortex tubes which are convected downstream. Phase-averaging based on the Strouhal number reveals a wake structure with quasi-periodic features that is much different from the structure suggested by the time-average velocity/vorticity field. The time-average vorticity field in the wake is characterised by a pair of counter-rotating streamwise vortex tubes, whereas phase-averaging highlights the role of half-loop structures on opposite sides of the wake.

4.1 Introduction

Turbulent flow over a bluff body is often used to analyze wake structures. For a finite square prism mounted on a wall, the structure of the wake is influenced by the flow over the top of the free-end of the prism and the boundary layer developing on the ground plane, as well as the spanwise shear layers shed from the two sides of the prism. Turbulent flow over external bodies such as a prism is a complex phenomenon, since it involves both the large-scale periodic motions associated with vortex shedding, as well as smaller-scale motions associated with the fluid turbulence.

For a finite square prism, the time-average flow structure shows streamlines that separate from the top leading edge and upstream spanwise edges to create a large recirculation zone behind the prism. For an approach flow with a relatively thin boundary layer, there is one major pair of counter-rotating vortex structures, referred to as tip vortices, which originate at the free-end and extend into the near-wake. There is secondary recirculation close to the wall junction, but the tip vortices are dominant. In contrast to the time-averaged flow, the instantaneous velocity field in the wake presents significant complexity. It includes large-scale vortical structures, some of which exhibit a periodic behavior, as well as small-scale turbulent motions. For the periodic motions, phase-

averaging based on the dominant frequency of the fluctuating velocity field, can be used to identify the characteristic structure of the periodic cycle. Within this context, recent studies, e.g., Sattari *et al.* (2012) and Bourgeois *et al.* (2011, 2013), of finite prism flows aim to better understand the vortical structures in the near-wake, in particular the mechanism whereby the vertically oriented vortex tubes being shed from the lateral sides of the prism become re-aligned in the streamwise direction.

The flow over a finite-height square prism has been widely studied using experimental methods; many of these studies found periodic behavior even for relatively short prisms. For finite-height prisms, an important parameter is the aspect ratio $AR = H/D$, where H and D are the height and width of the prism, respectively. In a study by Sattari *et al.* (2012) particle image velocimetry (PIV) was used to study the flow field over a square prism of aspect ratio $AR = 4$ and Reynolds number of $Re = 12,000$ (based on freestream velocity U and the prism width D). They observed alternating vortex shedding on the prism sidewalls. In a related experimental study by Bourgeois *et al.* (2011, 2013) with the same flow configuration, phase-averaged structures were extracted from the velocity field based on the dominant shedding frequency. For this relatively thin boundary layer ($\delta/D = 0.72$), alternating half-loop structures were observed in the near-wake. The half-loop structure consists of two vortex tube segments aligned primarily in the vertical and streamwise directions. The vertical leg is perpendicular to the ground plane and is called the principal core. The horizontal leg, which has a streamwise orientation, is called the connector strand. Bourgeois *et al.* (2011) indicated that the connector strand of one half-loop connected across the wake to connect to the base of the principal core of the upstream half-loop. For one complete cycle, a half-loop structure is generated on each side of the prism wake in an alternating pattern. Within the same group, a third study (Hosseini *et al.* 2013) performed PIV measurements of the flow field over a finite-height square prism with aspect ratio $AR = 8$ and Reynolds number $Re = 12,000$ for two inflows representing a thin ($\delta/D = 0.72$) and a thick turbulent boundary layer ($\delta/D = 2.56$.) Recall that the dominant frequency, f, is used to determine the Strouhal number $St = fD/U$, which is often associated with vortex shedding. Although the Strouhal number $St = 0.102$ was the same for both boundary layers, for the thin boundary layer the time-averaged wake structure was dipole and the phase-averaged structure consisted of a half-loop, whereas for the thick turbulent boundary layer, the time-averaged wake was quadrupole and the phase-

averaged structure consisted of a full loop. A quadrupole wake is characterised by two pairs of streamwise vortices (tip and base vortices), whereas for the dipole wake there is only one pair (tip vortices.)

In a wind tunnel study of flow over a finite-height square prism, McClean and Sumner (2012 and 2014) observed a different flow behavior for $AR = 3$ compared to the other aspect ratios ($AR = 5, 7, 9$ and 11 for a Reynolds number of $Re = 73,000$. They also found that the Strouhal number increased for taller prisms. Wang and Zhou (2009) performed an experimental study of flow over a finite-height square prism for different aspect ratios ($3 \leq AR \leq 7$) and a Reynolds number of $Re = 9300$. They observed periodic behavior which tended to be more symmetric near the free-end and anti-symmetric near the wall junction.

The unsteady flow field over a finite-height square prism has also been studied using computational methods. Saeedi and Wang (2016) performed a large eddy simulation (LES) based on the experimental study of Bourgeois et al. (2011). The prism aspect ratio was $AR = 4$, and the Reynolds number was $Re = 12,000$ with a relatively thin boundary layer thickness of $\delta/D = 0.72$. They observed the generation of unsteady vortex structures due to the interaction of the shear layers shed from the prism sides and the tip vortices on the free-end, with indication of von Karman vortex shedding. Based on the shedding frequency, the Strouhal number was determined to be $St = 0.11$.

Direct numerical simulation (DNS) has also been used to simulate finite prism flows, but typically at much lower Reynolds numbers. Vinuesa *et al.* (2015) studied the flow over a wall mounted finite-height square prism for $AR = 4$ and Reynolds number of $Re = 1000$ for both a laminar and turbulent inflow boundary layer. In their DNS, the shedding frequency was found to be similar for both the laminar and turbulent inflow boundary layers, however, the flow structures became different from each other downstream of the prism ($X/D > 3$). For the laminar inflow case, the flow transitions from laminar to turbulent upstream of the wake, which is the main difference compared to the case of a turbulent inflow. Saha (2013) performed a DNS of flow over a finite-height square prism for a Reynolds number of $Re = 250$. His study considered four different aspect ratios: $AR = 2, 3, 4$ and 5. He found that a higher aspect ratio results in a larger Strouhal

number, and that vortex shedding exists for all aspect ratios except AR = 2. Doussetalb and Potherat (2010) performed a DNS of a finite-height prism with an aspect ratio of AR = 4 and Reynolds number that ranged from 10 to 400. They showed that the Strouhal number increases with increasing Reynolds number. In a recent study by Zhang et al. (2017), direct numerical simulation (DNS) of the flow over a finite prism was performed for aspect ratio AR = 4 and Reynolds number that ranged from 50 to 1000.

The present paper reports on an LES of a low Reynolds number (Re = 500) flow over a finite-height square prism of aspect ratio AR = 3. This aspect ratio implies a relatively short prism, in which the separation of the flow over the free-end and the boundary layer on the ground flow are minimal. The main objective of this study is to analyze the flow structure in the near-wake for a relatively low aspect ratio geometry and a thin laminar inflow boundary layer. Phase-averaging is used to explore the periodic motion, with the goal of better understanding the mechanism responsible for the half-loop structures in the wake.

4.2 Mathematical Model and Numerical Method

The LES is based on the filtered continuity and Navier-Stokes equations for constant property flow. In this study, the dynamic nonlinear model (DNM) developed by Wang and Bergstrom (2005) is used for the subgrid-scale (SGS) or residual stress term. This SGS model has the benefit of a more complex and realistic coupling with the smallest resolved scales. It is capable of predicting backscatter, i.e. the transfer of energy from SGS to the resolved scales, and does not require any special treatment to ensure numerical stability. The finite-volume method was used to discretize the filtered Navier-Stokes equations, with a semi-implicit Crank-Nicolson scheme for temporal interpolation. A second order fractional step method was used to solve the continuity and momentum equations. For incompressible flow, the velocity field was corrected to ensure mass conservation using a so-called pressure-correction method. A four-level multi-grid scheme was used to efficiently solve the linear algebraic equations obtained from the pressure-correction method. The mathematical equations and full details of the numerical method are presented in a companion study that evaluated the effect of the SGS model on the LES prediction for the velocity field (Moazamigoodarzi and Bergstrom, 2018).

Figure 4.1 shows the solution domain, as well as the spacing of the prism. For the square prism of width D and height H, the aspect ratio was $AR = 3$. The domain size was 16D long in the streamwise (X) direction, with 3D upstream and 12D downstream of the prism. The vertical or spanwise (Y) extent of the solution domain was 6D and the transverse (Z) extent was 7D. For the geometry adopted, the blockage ratio of the prism was 7 percent. Hyperbolic-tangent functions were used to create a non-uniform Cartesian mesh of hexahedral cells. The grid is refined near the side walls, the surface of the prism and the ground plane, and gradually coarsened downstream of the prism, as shown in Figure 4.2. The total number of control volumes is approximately 1.77×10^6, with 128, 144 and 96 control volumes in the streamwise (X), vertical (Y) and transverse (Z) directions, respectively. The number of control volumes used to define the prism are 34 in the streamwise direction, 98 in the vertical direction and 34 in the transverse direction. Comparison with the DNS studies of Saha (2013) and Zhang *et al.* (2017) indicates that although the present study uses a smaller solution domain, the grid density is similar to the fine meshes used in those studies, and that the resolution of the flow near the prism is in fact greater. In the companion study (Moazamigoodarzi and Bergstrom, 2018), we also show that the ratio of the maximum control volume dimension to the Kolmogorov length scale is always less than or equal to 2.8, which indicates that the grid is well-resolved for an LES study. For the grid adopted, use of a CFL number of $CFL = 0.3$ resulted in a maximum time-step of $\Delta t = 0.0001$ s.
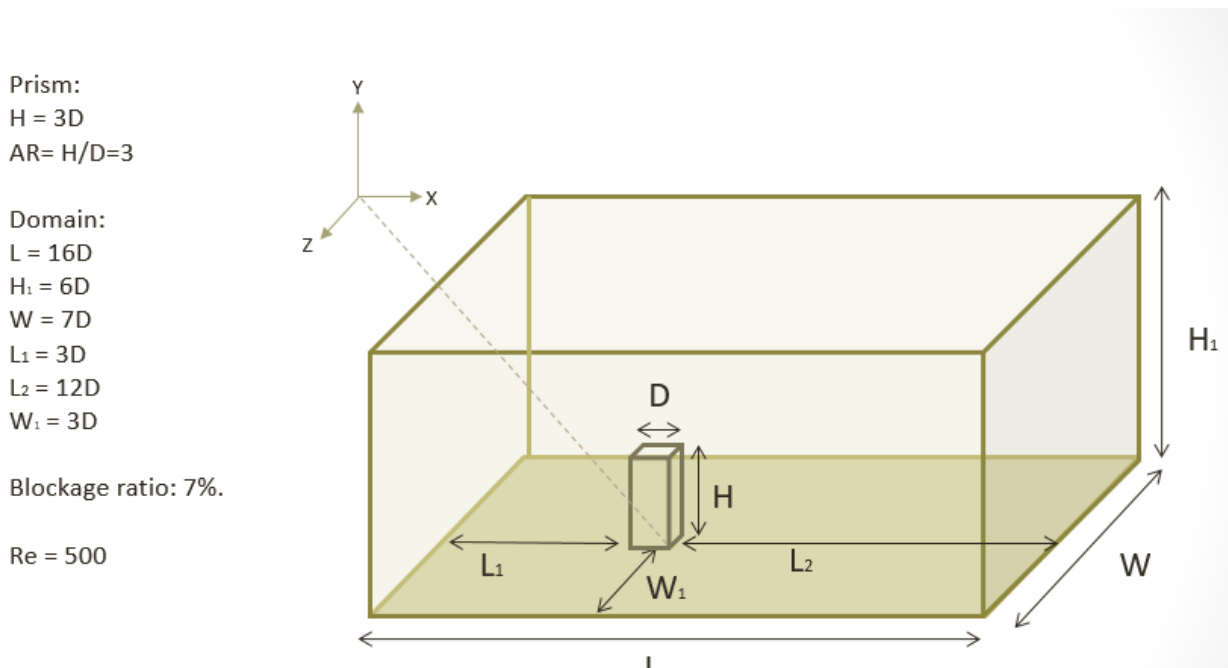

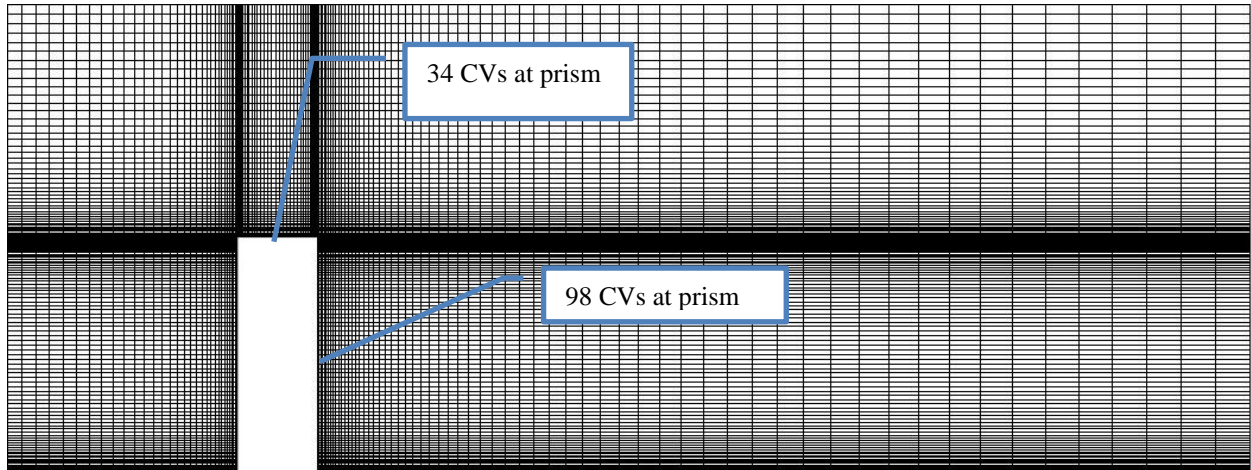Figure 4.1. Domain and prism geometry

Figure 4.2. Grid section in the vertical $(X - Y)$ mid-plane.

In terms of boundary conditions, the inflow is a uniform laminar velocity profile with a thin boundary layer of $\delta/D = 0.01$. The Reynolds number based on the freestream velocity and prism width is $Re = 500$. The ground plane and prism surfaces are treated as no-slip impermeable walls, while the side and top surfaces are modeled as free-slip walls. The outlet uses a convective boundary condition. The boundary layer thickness at the location of the prism was estimated to be approximately of $\delta/D \approx 0.2$.

In order to monitor the periodicity of the flow, three probes were positioned within the recirculation zones of the near-wake that are affected by vortex shedding from the prism. The locations of the probes are given in Table 1. The probes collected instantaneous values of the pressure and the three velocity components.

Probe number	x coordinate	y coordinate	z coordinate
Probe #1	2D	H/4	D/2
Probe #2	2D	H/2	D/2
Probe #3	2D	3H/4	D/2

Table 4.1. Probe locations, note that the location of the origin of the coordinate system is the intersection of the symmetry plane, prism rear wall and the ground plane. H is the prism height and D is the prism diameter

86

Use of the Fast Fourier Transform (FFT) and Power Spectrum subroutines in MATLAB enabled the power spectrum of the velocity signals to be plotted as a function of frequency. Figure 4.3a) shows a temporal trace of the instantaneous transverse (Z) velocity component and Fig. 4.3b) its power spectrum as recorded by probe number 3, located at $(X = 2D, Y = \frac{3H}{4}, Z = D/2)$. The spectrum exhibits a dominant peak frequency of $f = 2.35\ Hz$ which corresponds to a Strouhal number of $St = 0.125$ and a period of $T = 0.4252\ s$. This frequency is consistent with the velocity and pressure data of the other probes located in the near-wake which are not shown here. The value of the Strouhal number is consistent with the results of previous studies, e.g. the value of $St = 0.114$ from the DNS study of Saha (2013) for $AR = 3$ and $Re = 250$; the value of $St = 0.1$ from the DNS study of Doussetalb and Potherat (2010) for $AR = 4$ and $Re = 400$; the values of $St = 0.123$ and 0.113 from the DNS study of Zhang *et al.* (2017) for $AR = 4$ and $Re = 250$ and 500, respectively.

There is also a second peak frequency in the power spectrum of Figure 4.3 that corresponds to the time period for the shedding of a single vortex core from one lateral face of the prism. This frequency was $f = 10\ Hz$, which is approximately five times higher than that of the dominant frequency of the periodic cycle. This implies that a vortex core is shed from the lateral sides of the prism multiple times within a single periodic cycle. A line with a slope of -5/3 is also shown in Figure 4.3; a comparison with the power spectrum indicates that some of the resolved-scale turbulent motions have a similar slope, which is indicative of the inertial sublayer.

For phase-averaging, the time period associated with one complete cycle was divided into five smaller phase periods or bins. The velocity field in the wake was time-averaged over each phase of the cycle, and the result stored in that bin. At the end of one periodic cycle, five phase bins were collected, each of which contained the velocity field averaged over the phase period. Each periodic cycle required approximately 42108 time-steps. The velocity field in each bin can be considered indicative of the characteristic features of the velocity field at a time in the periodic cycle corresponding to the center of the bin. This procedure was repeated five times to provide data for five complete cycles. Finally, for each phase the velocity fields in the five bins were averaged again, which resulted in the phase-averaged velocity field for the prism wake. As documented in
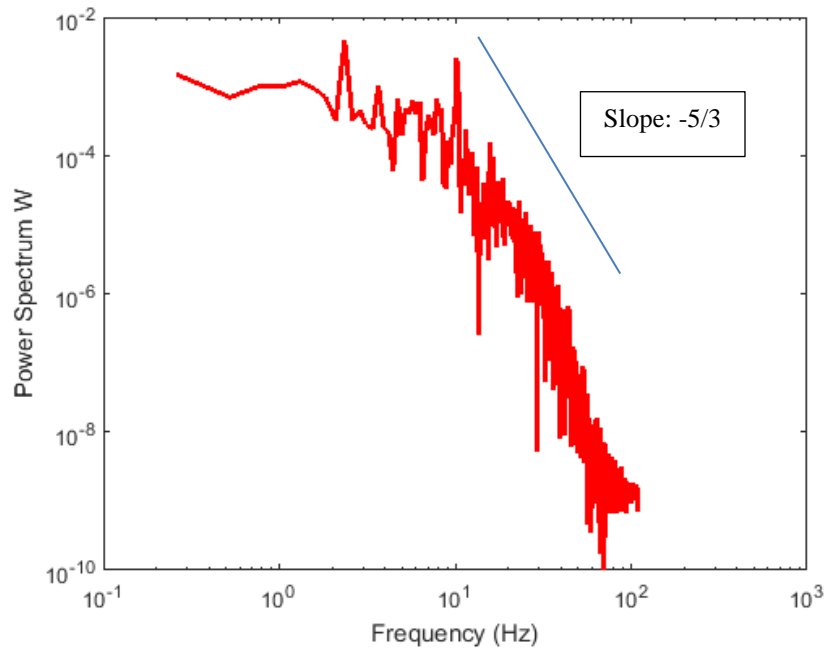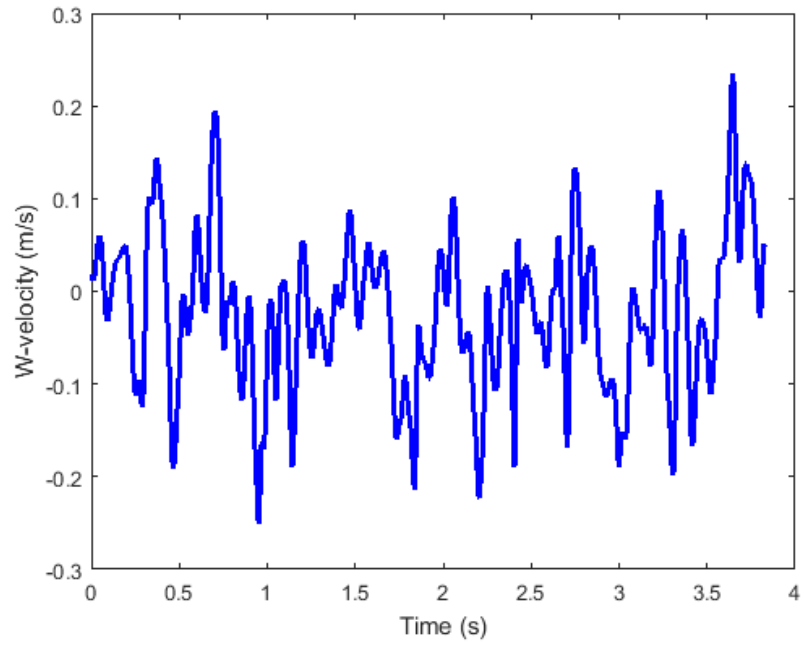
Figure 4.3. a) Trace, and b) power spectrum of transverse velocity for probe 3 in the near-wake of the prism $(X = 2D, Y = 3H/4, Z = D/2)$

the next section, phase-averaging revealed a wake structure with quasi-periodic features that is much different from the structure suggested by the mean velocity field.

4.3 Results and Discussion

Figures 4.4a) to 4.4e) show the three-dimensional (3D) phase-averaged vortex structure in the near-wake for phases N = 1 to 5, visualized from above by contours of the second invariant of the velocity gradient tensor flooded by streamwise velocity. In this case, the variation in the streamwise velocity is informative, since it results in stretching and deformation of the vortex structures. In terms of an overall pattern, these figures show shear layers separating from the top and side walls of the prism, moving downstream as initially vertical cores, and finally developing into larger horizontal structures which extend downstream. The flow structure appears to be relatively symmetric near the prism becoming asymmetric further downstream. A more careful scrutiny of the vortex shedding process on each side of the prism reveals a life cycle which might be characterized as follows: the shear layer sheds from the side of the prism, separates and rolls up into a vortex core with a vertical orientation; the core is transported downstream, in the process it is deformed such that the height is reduced and the top portion becomes (partially) aligned in the streamwise direction; with further deformation, streamwise cores become dominant; finally, the entire vortex structure dissipates further downstream. This process occurs sequentially on both sides of the prism and one periodic cycle consists of successive shedding sequences on each side of the prism. Note that there are also are multiple horseshoe vortices created by the initial interaction of the upstream flow with the prism and the ground plane.

Within the general shedding process described above, the flow develops such that it moves through a sequence of phases each of which has a distinct characteristic structure. These figures show the evolution of the vortex shedding process over one complete cycle or period. As noted above, the analysis used 5 phase bins to describe the overall cycle; the number assigned to a specific phase is arbitrary, since it is only the sequence of the phases which is important. The phase development can be characterized in terms of the downstream transport of vortex structures shed at the rear vertical edge of the prism, and the associated deformation and realignment of the vorticity. If we

focus first on the left side of the prism (viewed from downstream) the process can be described as follows:

1) In phase $N = 1$, we observe three vortex cores labelled A_1, B_1 and C_1 as shown in Figure 4.4 a) which have been shed from the sidewall of the prism. The first two cores exhibit a curvature, such that the bottom and top ends stretch back toward the prism. The third core, C_1, is relatively small with only a very short vertical leg, and is notably stretched in the streamwise direction. Note that on the opposite side of the wake from the relatively weak core, C_1, is a large dominant half-loop structure. On both sides of the prism, the first core is still connected to the shear layer on the side of the prism by a small strand which is in the process of being pinched off as part of the shedding process. Beyond approximately 5D downstream from the prism, the wake consists of mostly streamwise vortex tubes. For this phase the streamwise tubes are strongly aligned on the left side of the prism.

2) In phase $N = 2$, we again observe three vortex cores. The vortex core labelled A_1 in phase $N = 1$ (Figure 4.4a) has now been convected downstream and is identified as A_2; likewise vortex core B_1 moves downstream to become B_2; the third vortex core C_1 is no longer visible as a distinct entity since it has been dissipated. The displacement of each core over the time between phase periods is estimated to be approximately 1.5D if the convection velocity is assumed to be approximately equal to the freestream velocity. This corresponds roughly to the observed distance of translation of each core between phases. Note again that the top of the vortex core either bends back into the wake such as A_2 or trails back to connect to the previous vortex core such as B_2. The vortex core B_2 has also become larger and stronger, and is bent slightly outward. In the downstream region dominated by horizontal cores, the vortex structures have moved laterally such that they occupy the center region of the wake.

3) In phase $N = 3$, we again observe three vortex cores that have detached from the prism and moved downstream. In this phase, the core labelled A_2 in phase $N = 2$ has moved further downstream and is now shown as A_3, while the core labelled B_2 in phase $N = 2$ has moved into the far wake and dissipated. The core A_2 has many of the features of a half-loop structure, i.e. a strong shorter core representing the vertical leg and a connector strand that extends back

to link with the top of the preceding vortex core. On the opposite side of the wake from the half-loop there is the absence of any strong vertical leg, and instead multiple streamwise cores occupying the central region of the wake. Further downstream, the wake is dominated by structures on the right side, although one core stretches across diagonally to terminate near the ground plane on the left side.

4) In phase $N = 4$, the same pattern of three vortex cores is repeated on the left side of the wake; further downstream there are additional vestigial structures which exist mostly as streamwise cores. The process of formation of a half-loop has now moved to the right side of the wake. Three vortex cores are evident, with the one downstream being the strongest. A side profile of the structures – such as that shown in Fig. 4.6c) – indicates that the last downstream core on the right side has the feature of a half-loop with the lower portion representing a vertical leg and the upper portion stretching back and slightly inward as a connector strand.

5) In phase $N = 5$, the flow exhibits three vortex cores on each side of the wake. On both sides, the core furthest downstream has some features of a half-loop, however, the downstream core on the right side is much stronger. Further downstream, the flow is dominated by streamwise cores, with some diagonal alignment across the wake. This phase represents the growing dominance of the vortex structures on the right side of the wake. As the periodic cycle repeats itself, in phase $N = 1$ a strong half-loop structure is evident on the right side of the wake, and in phase $N = 2$ the structures on the right side begin to diminish as the dominance shifts back to the left side.
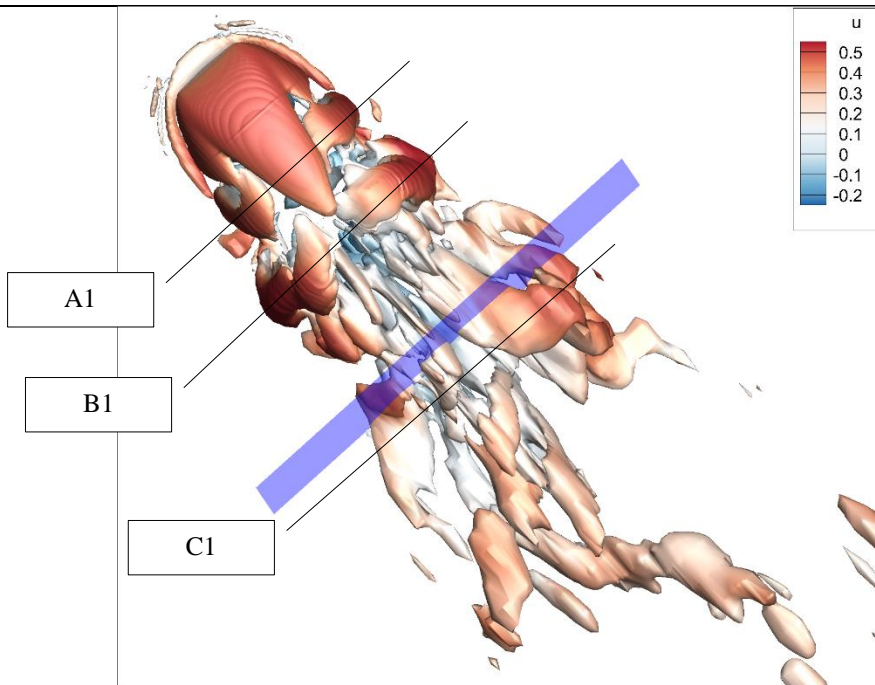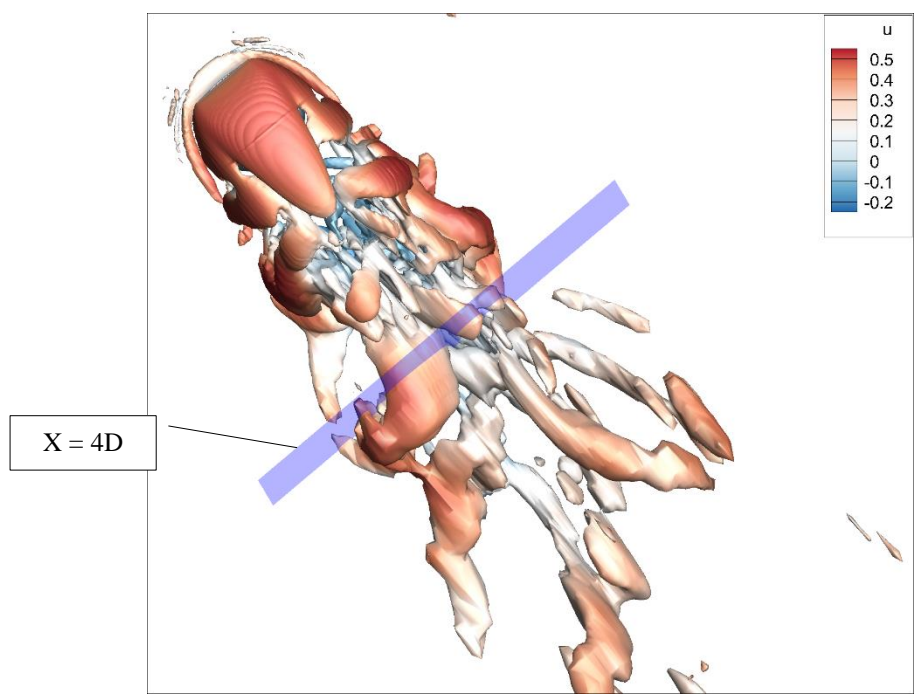
a) Phase N=1
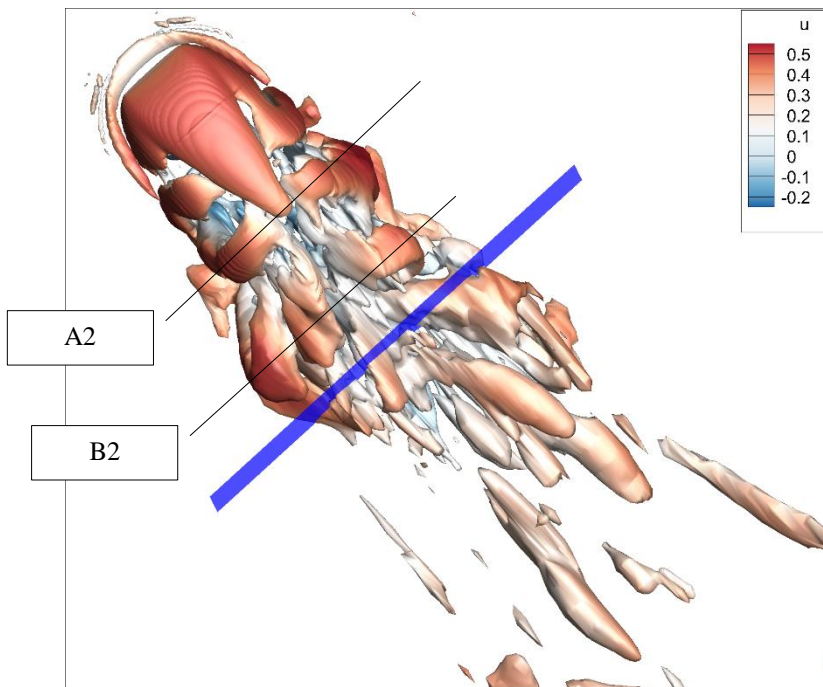
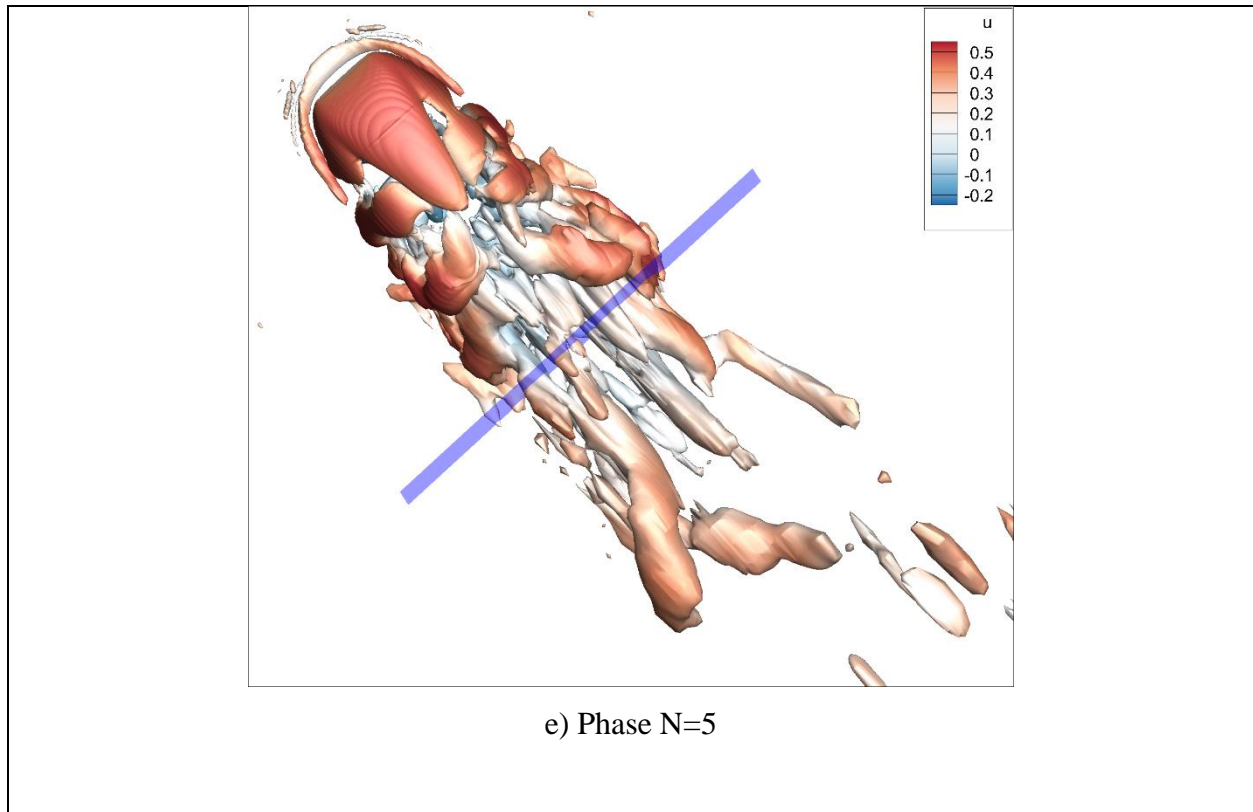b) Phase N=2
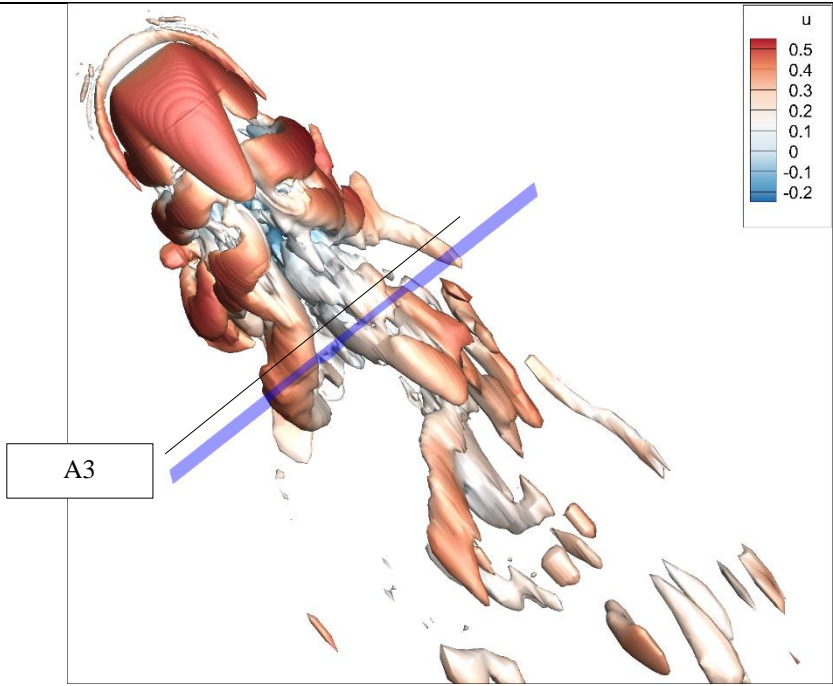
c) Phase N=3

d) Phase N=4

e) Phase N=5

Figure 4.4. Visualization of phase-averaged vorticity field using second invariant contours flooded by streamwise (X) velocity.

Figure 4.5a) shows a representative half-loop structure extracted from phase $N = 3$; it represents the third vortex core shed on the left side of the prism. In this case, the vertical leg leans back toward the prism at the upper end; the lower end does not directly contact the ground plane. The upper end of the half-loop becomes a connector strand which appears to link back to both vertical cores upstream. The connections between vertical cores on the left side of the prism wake is different from the model proposed by Bourgeois *et al.* (2011), as shown in the Figure 4.5b), who suggested that a connector strand typically crosses the wake to connect with the previous half-loop structure on the opposite side of the wake. One possible explanation for this difference is the much lower Reynolds number considered in the present study.

Half-loop

Connector strand

Principal core

a) Phase-average structure for N = 3

b) Schematic from Bourgeois *et al* (2011).

Reprinted from [Bourgeois, J. A., Sattari, P., and Martinuzzi, R. J. (2011). Alternating half-loop shedding in the turbulent wake of a finite surface-mounted square cylinder with a thin boundary layer. Physics of Fluids, 23 (9), 095101], with the permission of AIP Publishing.
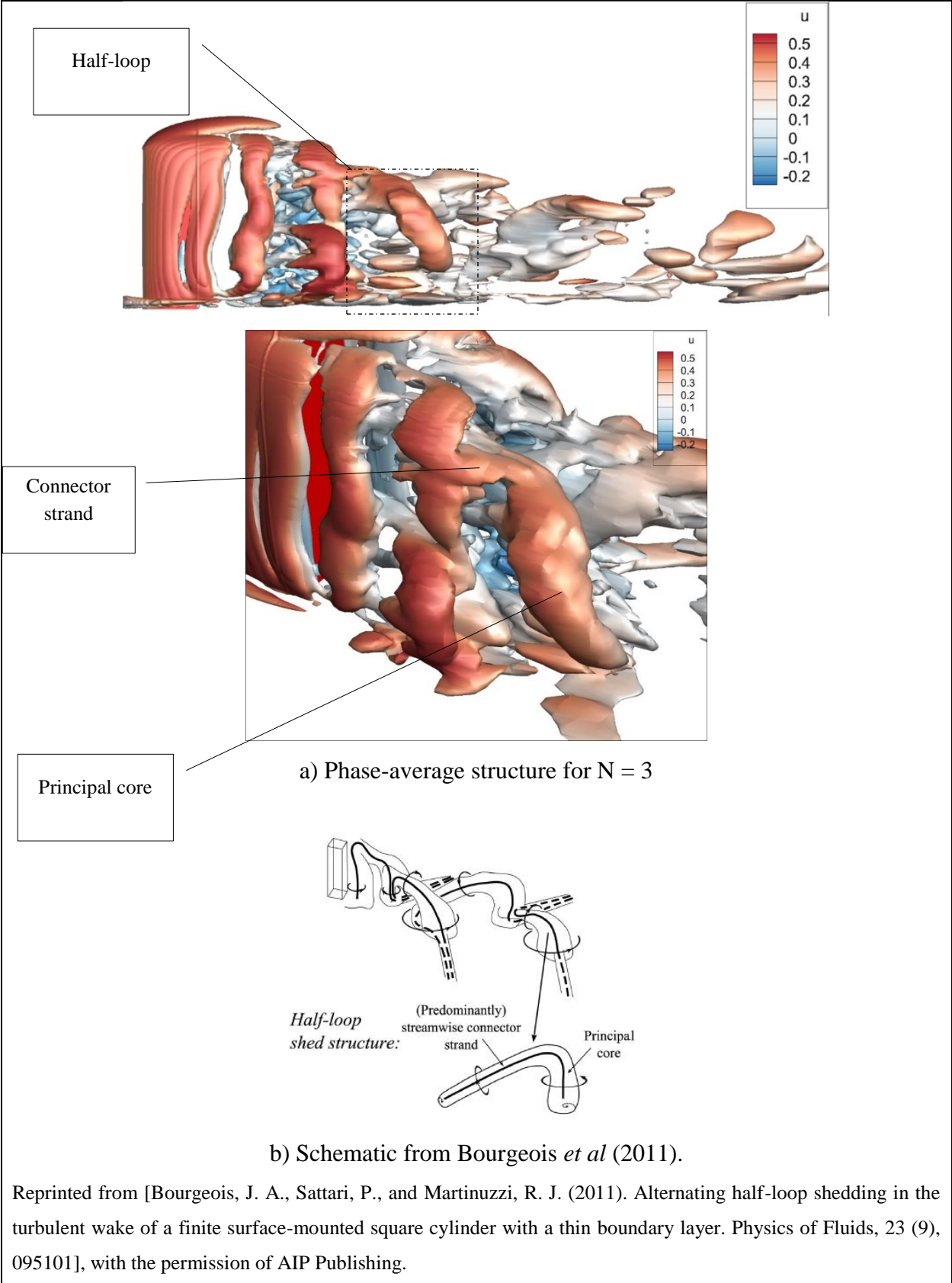
Figure 4.5. Half-loop structures

Figures 4.6 to 4.10 present a vertical section through the wake located at $X/D = 4$ for each of the five phases. It characterizes the local flow structure in terms of velocity vectors and contours of streamwise vorticity in a plane perpendicular to the dominant flow direction. It also uses streamtraces in the plane to highlight the rotational structures, although these are not strictly streamtraces, since there is a strong streamwise velocity component normal to the plane. These visualizations highlight the presence of any vortex cores, such as connector strands, oriented in the streamwise direction; vortex tubes in the vertical direction, such as the vertical leg of a half-loop, are not visualized in these planes. Overall, these figures indicate that each phase is characterized by the presence of a distinct set of vortex structures. For all phases, the flow pattern at the centre of the wake is dominated by downwash flow. Near the ground plane, the flow becomes more complicated, including jet-like flows into and out of the wake, and narrow vortex structures located close to the ground plane.

In Figure 4.6a) for phase $N = 1,$ the strong clockwise vortex motion on the right side of the wake creates a large recirculation zone. If we use streamtraces in the plane to further visualize the flow pattern, see Figure 4.6b), the dominance of this vortex structure is clearly evident. Finally, comparing to the 3D vortical structure shown in Figure 4.6c), the large vortex is associated with the connector strand coming from a strong half-loop structure on the right side of the wake. The connector strand connected to the half-loop results in counter-clockwise rotation, indicative of positive vorticity.

For phase $N = 2$, Figures 4.7a) and 4.7b) indicate multiple stronger vortex structures of different sign and at different heights on both sides of the wake. The connector strand associated with the half-loop developing on the left side of the wake results in a clockwise rotation associated with negative vorticity. However, there are also smaller vortex structures with positive vorticity on the left-hand side. Although the streamtraces again indicate a recirculation zone on the right side of the wake, it is weaker than for phase $N = 1$.

For phase $N = 3$, Figures 4.8a) and 4.8b) show that the flow is characterized by two strong clockwise vortex motions which straddle the location of the right side of the prism. These also induce a larger recirculation zone on the right side of the wake, as shown by the streamtrace
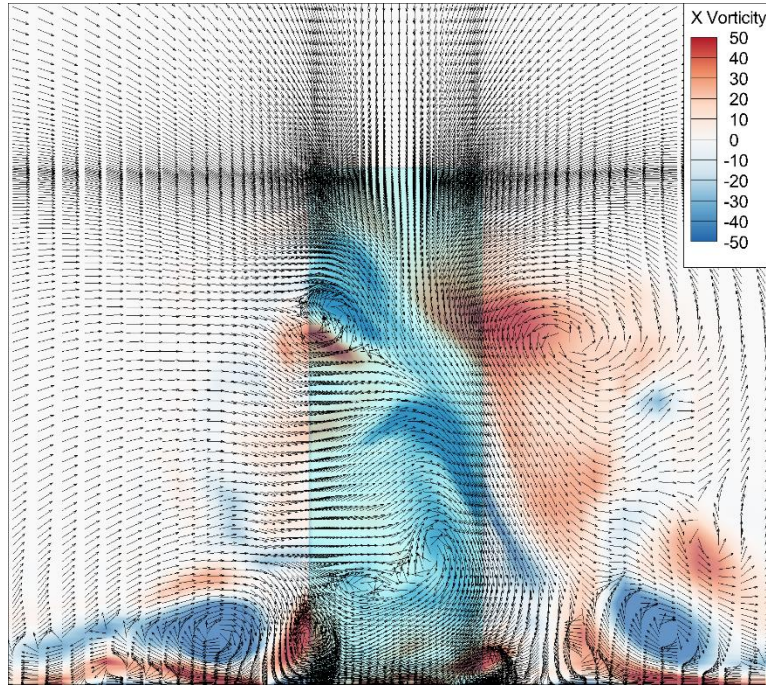
a) Velocity vectors and contours of streamwise vorticity
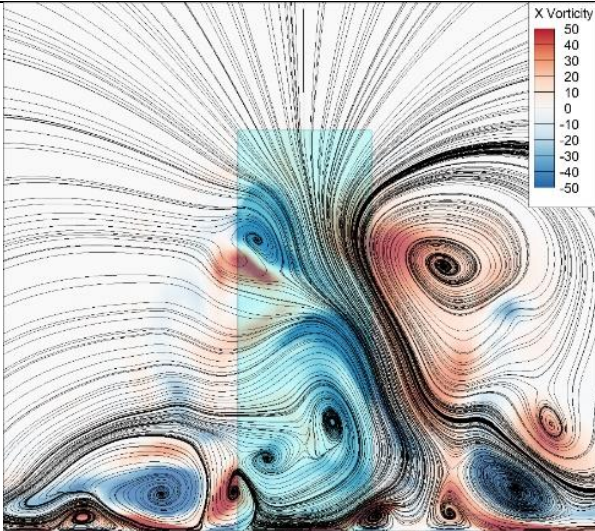
b) Streamtraces in the (Y-Z) plane
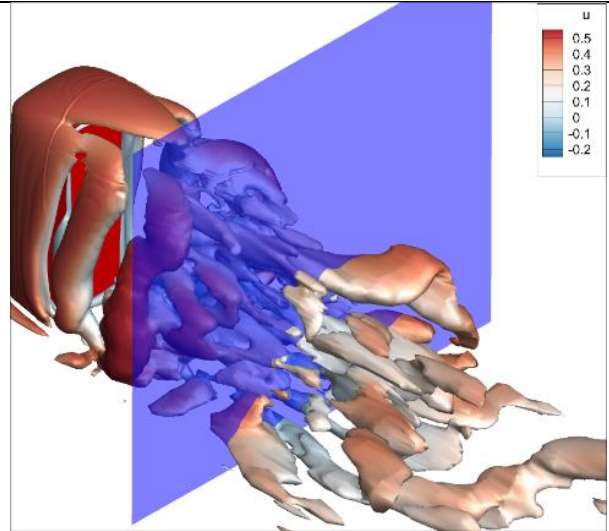
c) Visualization of the 3D vortex structure

showing section plane

Figure 4.6. Phase N=1 in the perpendicular plane X = 4D

a) Velocity vectors and contours of streamwise vorticity

b) Streamtraces in the (Y-Z) plane

Figure 4.7. Phase N=2 in the perpendicular plane X = 4D

a) Velocity vectors and contours of streamwise vorticity

b) Streamtraces in the (Y-Z) plane

Figure 4.8. Phase N=3 in the perpendicular plane X = 4D

pattern, see Figure 4.8b). Note that the overall flow pattern in this plane is from left to right across the wake. The absence of strong vortex structures on the left side of the wake is due to the fact that for this phase, the flow on the left side is characterized by a half-loop structure just upstream, with no connector strand cutting the transverse plane.

For phase $N = 4$, Figures 4.9a) and 4.9b) show the dominant vortex structure is now located on the left side of the wake, with a weaker vortex of opposite sign located below and to the right. A third vortex structure, also characterised by clockwise rotation and positive vorticity, is also present on the left side just below the other two vortex structures. Both the projected velocity vectors and streamtrace patterns indicate a large recirculation zone on the left side of the wake. Comparison with the 3D vortex structure shown in Figure 4.9c) indicates that the strong vortices observed in the velocity vector and streamtrace fields can be associated with horizontal vortex tubes being cut by the section plane. In the lower two-thirds of the wake, the transverse flow is from right to left, which is opposite to that for phase $N = 3$.

Finally, in Figures 4.10a) and 4.10b) for phase $N = 5$, the wake contains multiple vortex structures, with two larger structures downstream of the lateral edges of the prism. Recall in this phase the flow is in transition, with the half-loop structure on the left side dissipating and the next half-loop structure on the right side just developing. Overall, the phase-averaged flow pattern reveals the movement of dominant streamwise vortex structures from one side of the wake to the other over one periodic cycle. These structures are the signature of the passage of streamwise connector strands associated with half-loop structures on either side of the wake.

Streamtraces and contours of spanwise vorticity for the phase-averaged velocity field in the horizontal mid-plane located at $Y/H = 0.5$ are shown in Figure 4.11 for phase $N = 1$ and in Figure 4.12 for phase $N = 4$. When the flow initially encounters the prism, it creates a stagnation point on the front face and then divides to move around the sidewalls of the prism, as well as upward and over the free-end. The separation at the sharp leading edges of the prism creates narrow regions of reverse flow along the sidewalls of the prism. The separated shear layers do not reattach to the sidewalls but instead extend farther downstream into the wake region. The mean flow field (not shown) indicates that the near-wake region immediately behind the prism is dominated by reverse

a) Velocity vectors and contours of streamwise vorticity
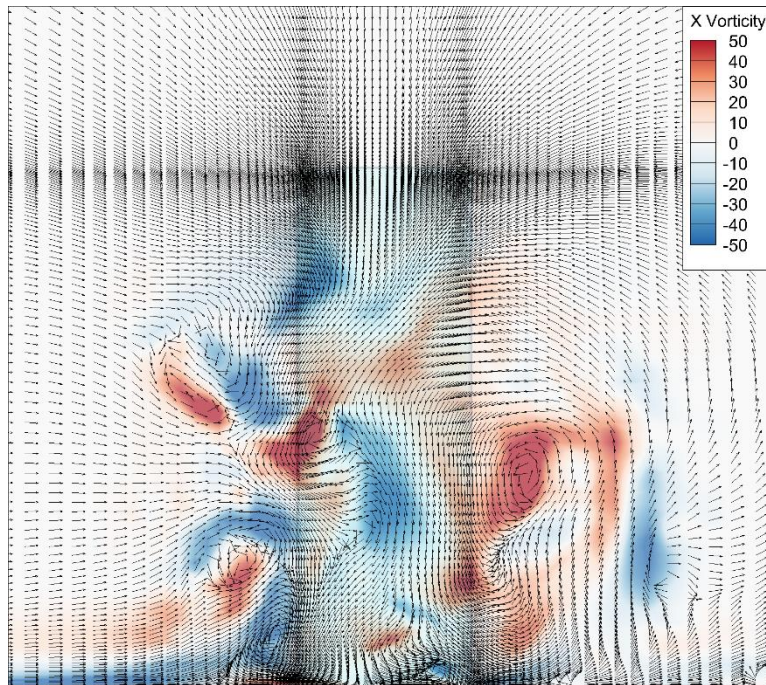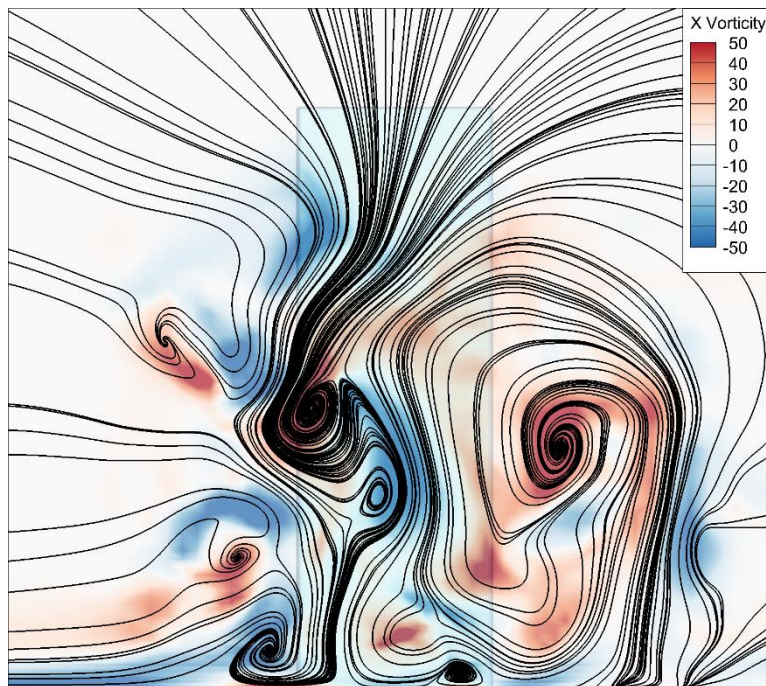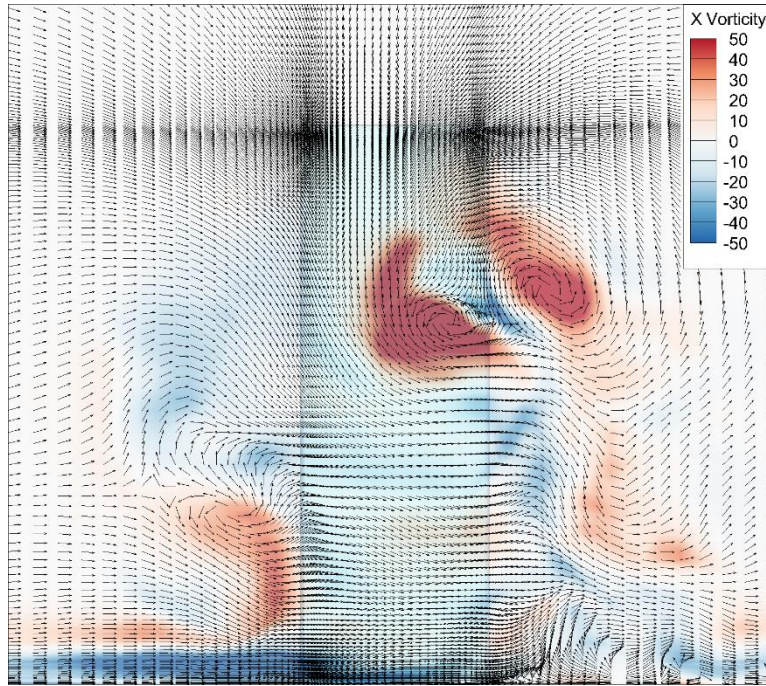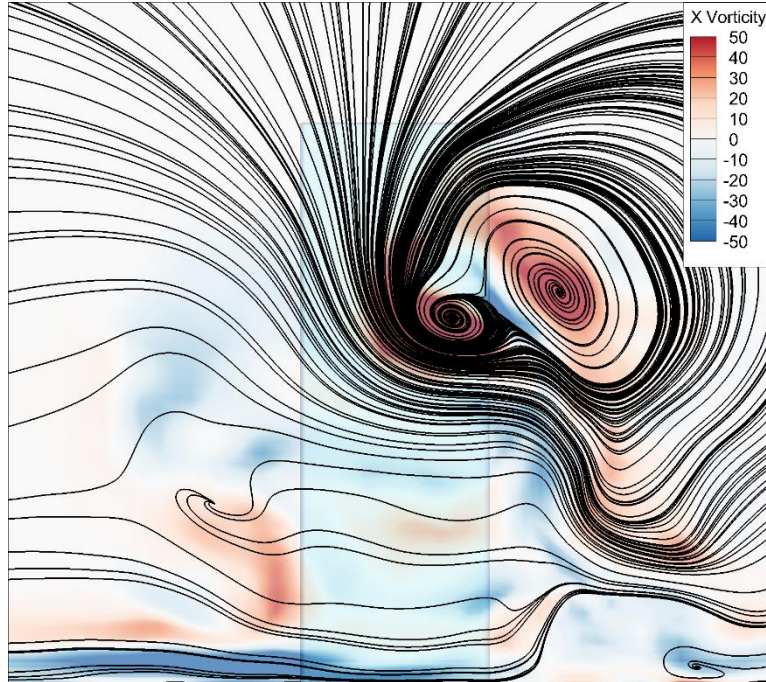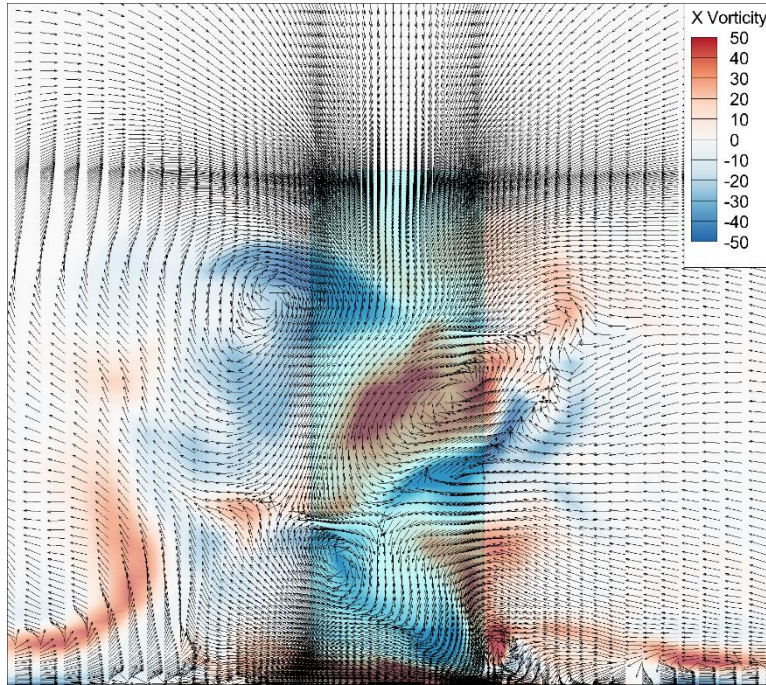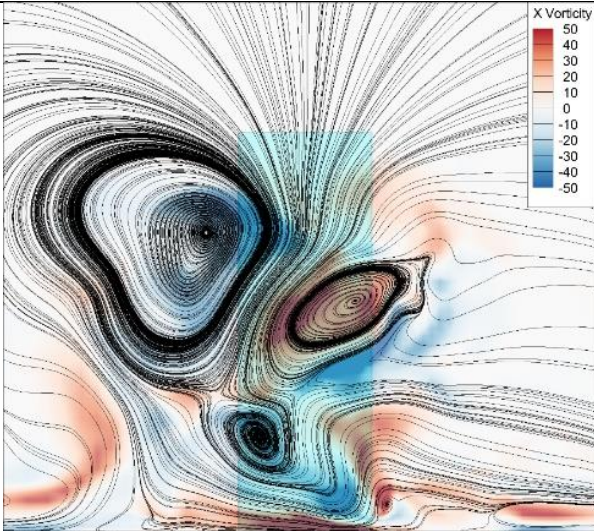

b) Streamtraces in the (Y-Z) plane
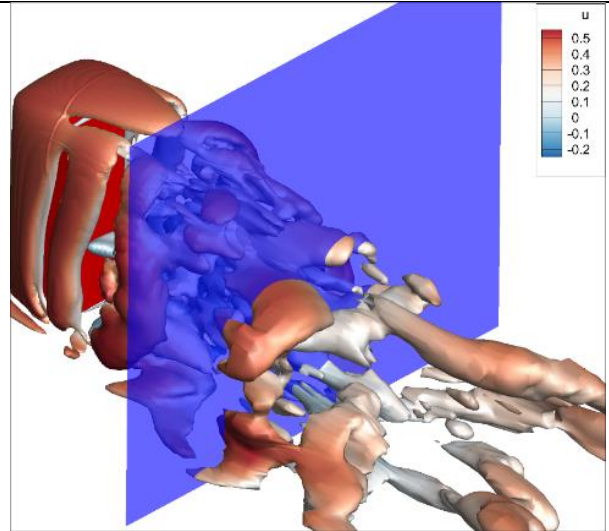
c) Visualization of the 3D vortex structure

showing section plane

Figure 4.9. Phase N=4 in the perpendicular plane X = 4D

a) Velocity vectors and contours of streamwise vorticity

b) Streamtraces in the (Y-Z) plane

Figure 4.10. Phase N=5 in the perpendicular plane X = 4D

flow which extends for approximately five diameters downstream from the rear face of the prism. There is a small reverse flow and recirculation region under the separated shear layer on each sidewall of the prism.

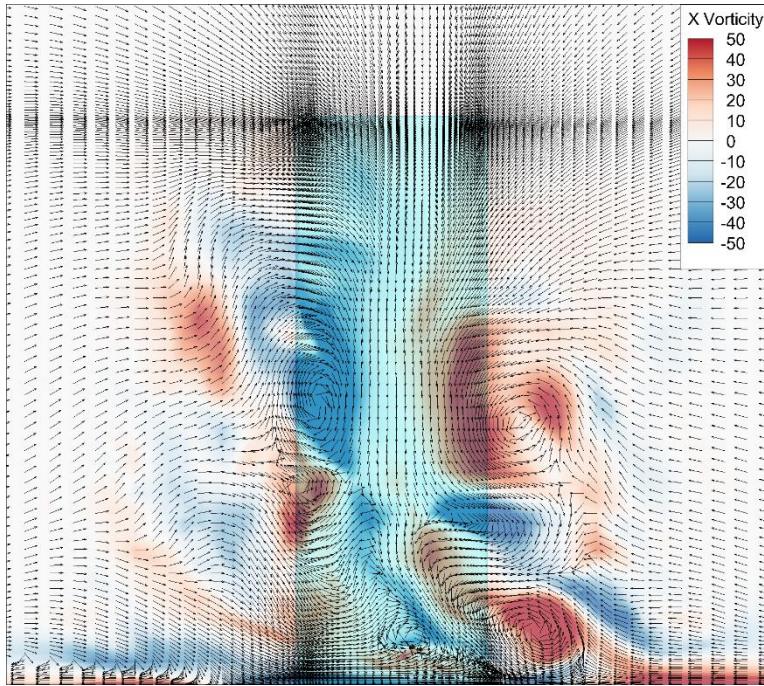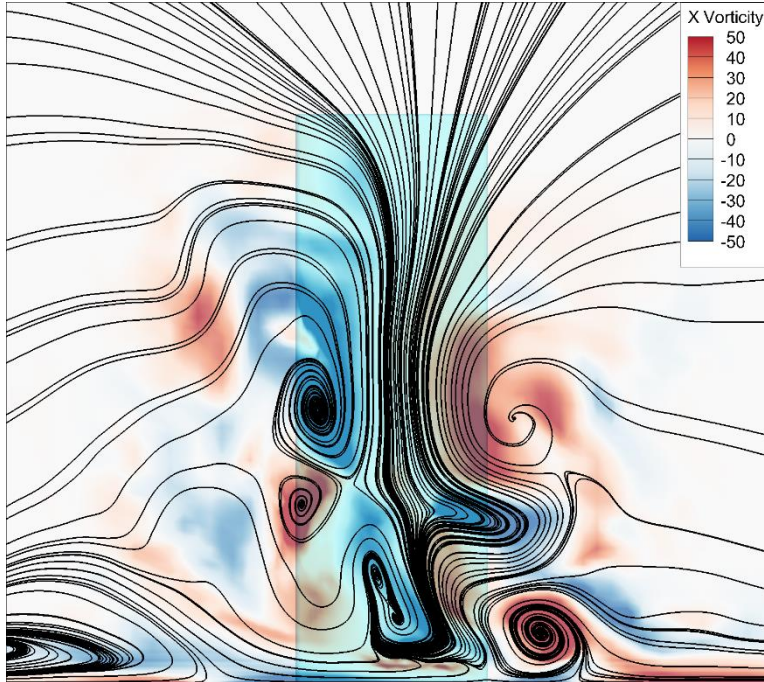Figure 4.11a) shows the three-dimensional flow structure for phase $N = 1$ with a horizontal section in blue indicating where the mid-plane cuts the vortex cores. The vertical cores are clearly evident on the left side of the wake in Figure 4.11a), but obscured by internal structures on the right side. Further downstream on the right side is a flattened connector strand which attaches to the vertical leg of a half-loop located below the section plane. These cores correlate with the vortices evident in the streamtrace patterns in Figure 4.11b). The streamtraces indicate three vortex structures on each side of the prism wake; the direction of rotation is opposite across the wake. The first vortex structure on each side of the wake is located along the sidewall. The next two vortex structures observed in the streamtrace pattern are associated with the first two vortex cores shed from the trailing edge of each side of the prism. Immediately behind the prism, the streamtraces indicate a reverse flow moving upstream toward the prism, where it interacts with a flow moving laterally across the rear face of the prism to supply the recirculation zone on the left side of the prism. The reverse flow is more clearly seen from the velocity vectors shown in Figure 4.11c). Finally, for this phase the flow pattern in the downstream section of the wake is displaced toward the right side of the prism, which is part of the large-scale oscillation of the wake over one periodic cycle.

Figure 4.12a) shows the three-dimensional vortex structure for phase $N = 4$ together with a horizontal section plane. The vertical vortex cores being cut by the section plane correspond to the vortices shown in the streamtrace pattern for the phase-average velocity field shown in Figure 4.12b). There is a single dominant vortex on the left side of the wake (upper region in Figure 4.12b) and as many as four vortices on the right side of the wake (lower region in Figure 4.12b). The direction of rotation of the vortices is opposite on opposite sides of the wake. Both the streamtrace pattern in Figure 4.12b) and the velocity vectors in Figure 4.12c) illustrate the reverse flow in the near-wake.

Figure 4.11. Visualization of the phase-average velocity field on the horizontal mid-plane for phase N = 1: a) section plane on 3D vortex structure; b) streamtraces and spanwise vorticity contours, and c) velocity vectors and spanwise vorticity contours.
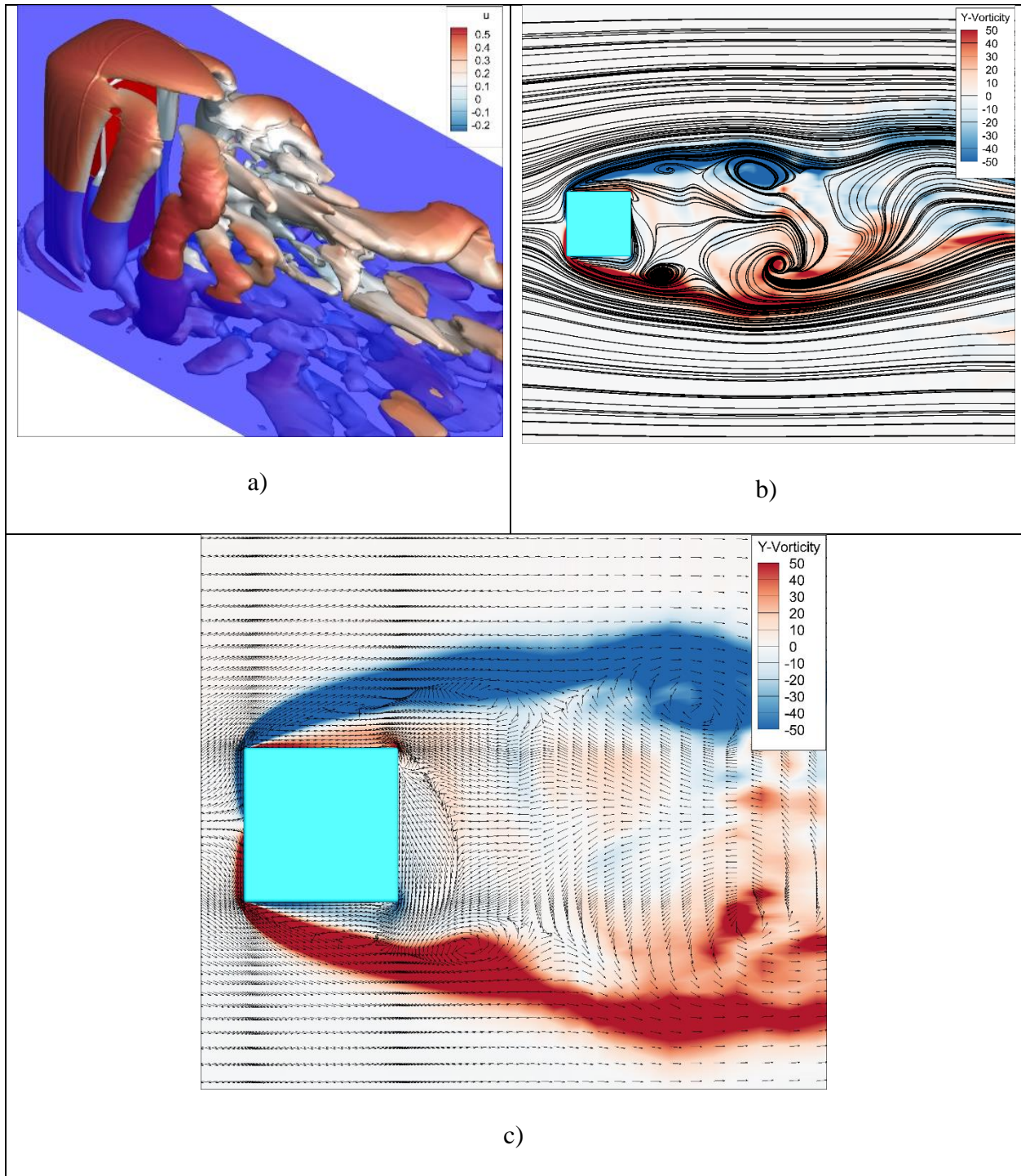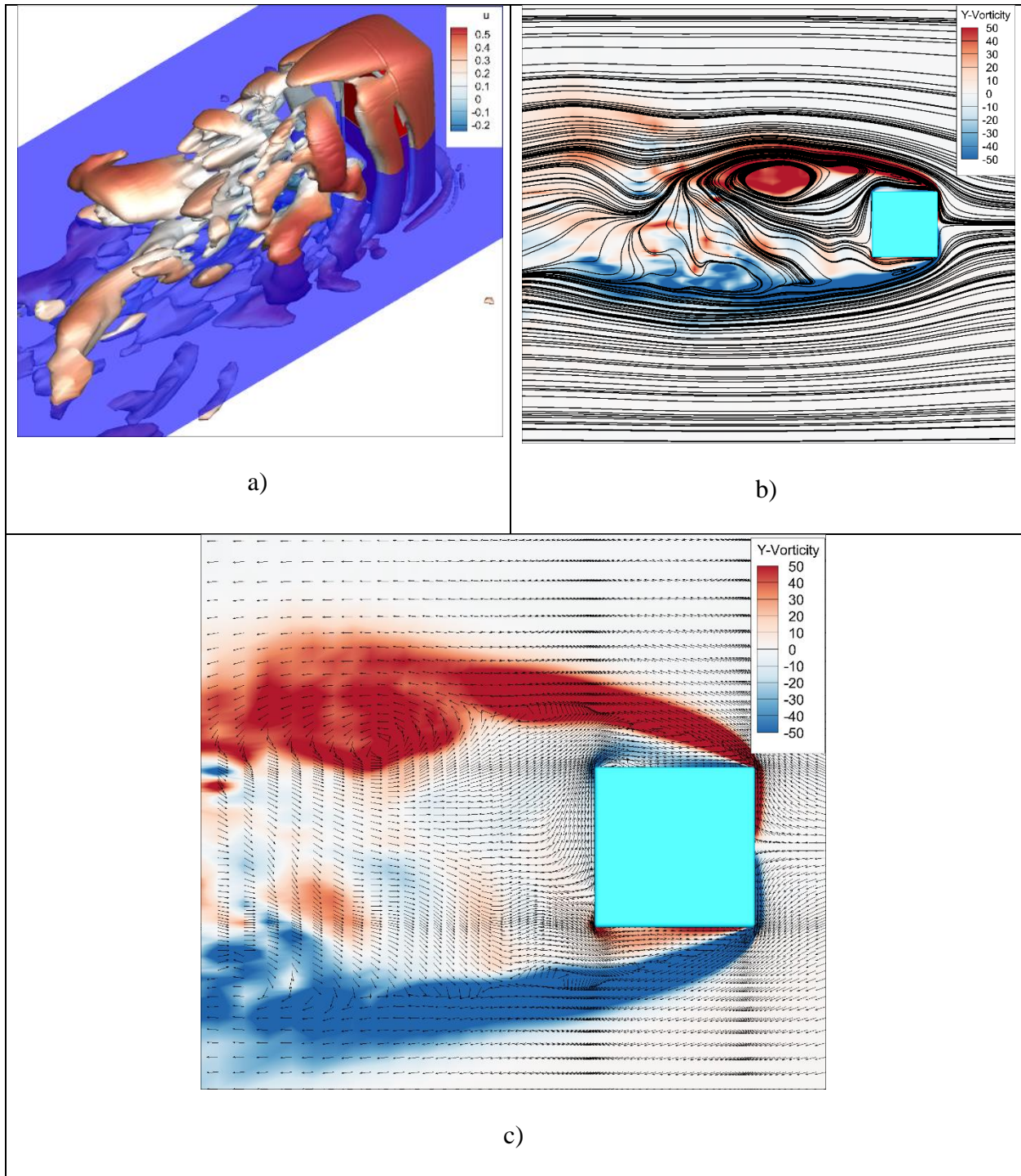
Figure 4.12. Visualization of the phase-average velocity field on the horizontal mid-plane for
phase N = 4: a) section plane on 3D vortex structure; b) streamtraces and spanwise vorticity
contours, and c) velocity vectors and spanwise vorticity contours

4.4 Conclusions

The present paper documents an LES study of low Reynolds number (Re = 500) flow over a finite-height square prism mounted on a ground plane. The inflow boundary layer is laminar and thin. The flow field predicted for this sub-critical aspect ratio of AR = 3 reveals a complex wake structure created by the interaction of the flow over top of the prism with the flow separating from the sidewalls. The analysis of the LES velocity field focuses on the phase-average structure based on the periodic cycle associated with the dominant frequency of the energy spectrum of the fluctuating velocity field. The period is not defined by a single vortex core being shed from the side of the prism. Instead, during a complete periodic cycle, multiple cores are shed from the sidewalls of the prism, and move downstream to become half-loop structures. During one periodic cycle, a half-loop structure is formed and dissipated in a sequential pattern on each side of the wake. The half-loop structure consists of a short vertical core called the leg, with a connector strand that trails backward to connect to the previous vortex core. This structure is similar to that observed by Bourgeois *et al.* (2011), except in their case the connector strand typically crossed the wake to connect to the half-loop formed on the opposite side of the wake.

The periodic cycle was also analysed in terms of the pattern of vortices in a vertical section of the wake oriented perpendicular to the freestream direction. Most phases are characterized by a preferential location of the dominant vortices on one side of the prism wake. During the periodic cycle, the location of the dominant vortices moves laterally across the wake. These vortices are evidence of streamwise vortex tubes, some of which are clearly the connector strands of half-loop structures. As the dominant vortices change their location in the section plane, they cause the overall transverse flow field to change its direction. The downstream section of the near-wake is typically dominated by vortex cores aligned in the horizontal direction. Furthermore, the horizontal vortex tubes exhibit a preference for one side of the wake depending on the phase.

When the phase-averaged velocity field is visualized in the horizontal mid-plane, the vertical vortex cores being shed from the lateral sides of the prism appear as a series of vortices within the two shear layers being shed from the leading vertical edges of the prism. The flow in the wake immediately downstream of the prism exhibits reverse flow. Depending on the phase, most of the

reverse flow moves toward one sidewall of the prism, connecting to the region of recirculation between the separating shear layer and the prism wall.

The present results use phase-averaging of an LES field to investigate the complex structure of the near-wake of a finite-height square prism flow. It is surprising that for this very low aspect ratio prism, the flow structure remains strongly periodic. The flow under consideration is characterized by a low Reynolds number flow and a laminar inflow boundary layer. For higher Reynolds numbers and different inflow conditions, aspects of the flow structure will likely change, as has been observed in some of the experimental studies in the literature, e.g. Sattari et al. (2012).

4.5 Acknowledgements

4.6 References

Bourgeois, J. A., Noack, B. R., and Martinuzzi R. J. (2013). Generalized phase-average with applications to sensor-based flow estimation of the wall-mounted square cylinder wake. *Journal of Fluid Mechanics, 736*, 316-350. DOI: 10.1017/jfm.2013.494

Bourgeois, J. A., Sattari, P., and Martinuzzi, R. J. (2011). Alternating half-loop shedding in the turbulent wake of a finite surface-mounted square cylinder with a thin boundary layer. *Physics of Fluids, 23* (9), 095101. DOI: 10.1063/1.3623463

Dousset, V. and Pothérat, A. (2010). Formation mechanism of hairpin vortices in the wake of a truncated square cylinder in a duct. *Journal of Fluid Mechanics, 653*, 519-36. DOI: 10.1017/S002211201000073X

Hosseini, Z., Bourgeois, J. A., and Martinuzzi, R. J. (2013). Large-scale structures in dipole and quadrupole wakes of a wall-mounted finite rectangular cylinder. *Experiments in Fluids, 54* (9), 1595.

McClean, J. F. and Sumner, D. (2012). Aerodynamic forces and vortex shedding for surface-mounted finite square prisms and the effects of aspect ratio and incidence angle. Proceedings of *ASME 2012 Fluids Engineering Summer Meeting*. Rio Grande, Puerto Rico, USA, July 8-12, 2012.

McClean, J. F. and Sumner, D. (2014). An experimental investigation of aspect ratio and incidence angle effects for the flow around surface-mounted finite-height square prisms. *ASME Journal of Fluids Engineering, 136* (8), 081206. DOI: 10.1115/1.4027138

Moazamigoodarzi, N. and Bergstrom, D. J. (2018). Large eddy simulation of a finite prism wake flow using dynamic linear and nonlinear subgrid-scale models. *International Journal of Computers and Fluids (Submitted).*

Saeedi, M. and Wang, B. C. (2016). Large-eddy simulation of turbulent flow around a finite-height wall-mounted square prism within a thin boundary layer. *Flow, Turbulence and Combustion*, *97* (2), 513-538. DOI: 10.1007/s10494-015-9700-7

Saha, A. K. (2013). Unsteady flow past a finite square prism mounted on a wall at low Reynolds number. *Computers and Fluids, 88*, 599-615. DOI: 10.1016/j.compfluid.2013.10.010

Sattari, P., Bourgeois, J. A., and Martinuzzi, R. J. (2012). On the vortex dynamics in the wake of a finite surface-mounted square prism. *Experiments in Fluids, 52* (5), 1149-1167. DOI: 10.1007/s00348-011-1244-6

Vinuesa, R., Schlatter, P., Malm, J., Mavriplis, C., and Henningson, D. S. (2015). Direct numerical simulation of the flow around a wall-mounted square prism under various inflow conditions. *Journal of Turbulence, 16* (6), 555–587. DOI: 10.1080/14685248.2014.989232

Wang, H. F. and Zhou, Y. (2009). The finite-length square cylinder near wake. *Journal of Fluid Mechanics, 638*, 453-490. DOI: 10.1017/S0022112009990693

Wang, B. C. and Bergstrom, D. J. (2005). A dynamic nonlinear subgrid-scale stress model. *Physics of Fluids, 17 (3)*, 035109. DOI: 10.1063/1.1858511

Zhang, D., Cheng, L., An, H., and Zhao, M. (2017). Direct numerical simulation of flow around a surface-mounted finite square cylinder at low Reynolds number. *Physics of Fluids, 29* (4), 045101. DOI: 10.1063/1.4979479

Chapter 5

Conclusions

5.1 Thesis Summary

This thesis has considered the application of linear and nonlinear dynamic SGS models to predict the complex wake flow behind a finite-height square prism of aspect ratio AR = 3 mounted normally to a ground plane. The inlet boundary layer was relatively thin and laminar, and the Reynolds number based on the prism width and freestream velocity was Re = 500. The code was based on LES with two different SGS models: the dynamic Smagorinsky model (DSM) and dynamic nonlinear model (DNM). The time-averaged and instantaneous flow fields, including the resolved velocity and pressure, and the dissipation of turbulence kinetic energy (SGS and resolved scale), were compared to assess the impact of the SGS models, especially on the mean flow in the near-wake. The first goal of the thesis research was to compare the outcomes of the two different methods of modeling unresolved small-scale motions in terms of the impact on the flow structure. A second goal of this thesis was to analyze the periodic flow structure for a relatively low aspect-ratio finite-height square prism at a low Reynolds number. The power spectrum of the fluctuating velocity field indicated a dominant frequency, corresponding to a Strouhal number of St = 0.12, consistent with previous experimental and numerical studies. Phase-averaging of the instantaneous velocity field based on the dominant frequency was used to investigate the periodic structure of the near-wake in terms of vortical structures. This process revealed structures that are removed by time-averaging and also are not fully visible in the instantaneous fields.

5.2 Conclusions

The first objective of this thesis (as described in Section 1.2.1) was to compare and assess the performance of two different dynamic SGS models in predicting the flow over a finite-height prism, with respect to flow structure and SGS energy transfer. The current study looked at the effects of the SGS models and, specifically, compared the predicted velocity field for the wake for a linear (DSM) and nonlinear (DNM) SGS model. Although the flow fields predicted by the two different SGS models were similar in many ways, there were also notable differences in both the instantaneous and mean velocity and vorticity fields. The LES results showed that the DNM has advantages compared to the DSM in terms of stability and grid resolution. The current study indicated that the stabilization mechanism negatively affects the ability of the DSM to accurately predict the smallest scale motions. For the same grid, the DNM predicted noticeably finer-scale structures compared to the DSM, because the DNM does not use any smoothing mechanism. This positively influenced the results for the time-averaged and instantaneous velocity and vorticity fields, as further discussed in the next section.

The second objective of this thesis (as described in Section 1.2.2) was to investigate the periodic structure of the wake of a finite-height square prism. The flow field predicted for this sub-critical aspect ratio of AR = 3 revealed a complex wake structure created by the interaction of the flow over the top of the prism with the flow on the sidewalls. The instantaneous flow exhibited a dominant frequency with a corresponding periodic structure. The phase-averaged spanwise vorticity patterns indicated a symmetric shedding type behavior immediately downstream of the prism. This quickly developed into an asymmetrical pattern further downstream, associated with strong transverse sweeping motions across the near-wake region. The originally vertical-oriented vortex cores formed by the roll-up of the shear layers shed from the lateral sides of the prism evolved downstream to create streamwise structures. The phase-averaged velocity field in transverse plane sections through the wake indicated strong vortical streamwise structures that changed their location over the course of a phase-average cycle. The phase-averaged velocity field in the horizontal mid-plane also showed the signature of the vertical cores being shed from the side of the prism and convected downstream within the shear layers bounding the near-wake.

Further discussion of the phase-averaged structures will be presented in the next section, in particular the development of half-loop structures.

5.3 Contributions

Overall, the current study complements current DNS studies in the literature, and makes a contribution by documenting specific flow features for this relatively small aspect ratio prism. The results obtained suggest that the AR = 3 flow is much more interesting – and complex – than might have been imagined. The paragraphs below document the principal contributions:

5.3.1 This section summarises the first contribution of the thesis (as described in Section 1.3.1) which relates to performing the two LES studies and evaluating the results. LES predictions of the finite prism flow with two different SGS models were implemented. Both subgrid-scale model's formulations were implemented and tested for their ability to resolve the complex wake structure associated with this flow. A comparison of the local length scale of the grid with an estimate of the Kolmogorov microscale at the same location indicated that overall the grid was well resolved for a LES for both SGS models. In particular the grid resolution of the LES near the prism compared favorably with the DNS studies. The results also showed that for the same grid, the DNM predicted a noticeably finer-scale structure compared to the DSM. This feature might be important for flows at higher Reynolds numbers, for which a higher grid resolution is needed. The combination of the dynamic method with a Smagorinsky model caused large negative values of the SGS viscosity. These large negative values also caused computational instability and required a stabilization mechanism. In this research, volume-averaging and clipping were used to restrict the magnitude of the SGS viscosity and hence to control computation stability. In contrast, the DNM does not have this stability issue. Summary comparisons of the main flow structure with DNS studies in the literature for a similar aspect ratio and Reynolds number indicated that both SGS models captured the main flow features (which will be discussed further below.) These low Reynolds number predictions also shared many similar features to the flows documented by experimental and computational studies at much higher Reynolds numbers.

5.3.2 This section summarises the second contribution of the thesis (as described in Section 1.3.2), which is to explore and contrast the main features of the mean and instantaneous velocity fields for the two SGS models. Although the flow fields predicted by the two different SGS models were similar in many ways, there were also notable differences in both the instantaneous and mean velocity and vorticity fields. It was surprising to see SGS effects evident in the mean velocity field. For example, the recirculation zone immediately downstream of the prism in the vertical mid-plane for the two SGS models was different in both shape and extent. There were also noticeable differences in the mean streamtraces in the horizontal mid-plane, in terms of shape, extent, and the location of the two principal vortices. In addition to the effect of the SGS model on the mean field, there were some significant differences relating to the magnitude of the SGS stress tensor τ_{yz} in the horizontal mid-plane. The DSM predicted peak values on the upstream face of the prism and for an extended region located in the shear layers bounding the mixing region. In contrast, the DNM predicted peak values in the initial region of the shear layers separated from the upstream edges of the prism; the values in the mixing region were relatively low.

5.3.3 This section documents the third contribution of the thesis (as described in Section 1.3.3), which is to analyze the dissipation of turbulence kinetic energy for the two different SGS models. In terms of the SGS dissipation of turbulence kinetic energy for each SGS model, the DNM predicted much less backscatter compared to the dynamic Smagorinsky model. The level of SGS dissipation was also much lower for the DNM, while the resolved and, hence, total dissipation was higher. The resolved dissipation was significantly higher than that for the DSM because the DNM preserves a much finer scale structure at the grid-scale, since it does not use the smoothing mechanism required to stabilize the DSM. In contrast to the DNM, the DSM was characterised by high levels of SGS dissipation and frequent occurrence of backscatter, with large peak values of positive and negative dissipation occurring next to each other. Overall, this comparison indicated that the two SGS models have much different mechanisms for achieving the total dissipation required to stabilise the LES.

5.3.4 This section documents the fourth contribution of the thesis (as described in Section 1.3.4), which is to perform a phase-averaged decomposition of the flow in the near-wake for the DNM. Unlike the time-averaged velocity field, the phase-averaged velocity field indicated asymmetric

periodic flow structures formed by the vortex tubes being shed from the top and side walls of the prism. These tubes re-oriented and interacted as they detached from the prism and moved further downstream, giving evidence of the half-loop structure alternatively on both sides of the prism wake. More specifically, the lower part of the core formed the vertical leg of a half-loop, while the top part of the core was bent back toward the prism and reconnected to the previous core, forming the connector strand. Note that the vortices in the transverse plane section were the effect of connector strands being created and transported downstream. The structure observed for the AR = 3 prism was similar to that for higher Reynolds number flows, but also different in some respects, possibly due to the difference in the Reynolds number. One difference was the fact that many of the connector strands in the present simulation did not cross over to connect to the half-loops on the other side of the wake, but instead connected to vertical cores upstream and on the same side of the wake. Overall, the deformation and realignment of the vortex tubes explains the generation of streamwise vorticity in a flow where the initial vorticity just downstream of the prism is aligned in the spanwise (vertical) direction.

5.4 Recommendations for Future Study

Flow over a bluff body has many practical applications, but is also of interest as a prototype flow for research purposes because of its complexity. The flow over a low aspect ratio finite-height square prism is complex and extremely three-dimensional. Finite prism flows are being actively studied within the fluid-structure community to better understand the effects of the free-end conditions. The wake structure has been shown to include a quasi-periodic component in addition to the turbulent fluctuations. As a result, these flows provide a critical opportunity for numerical methods and turbulence models, including SGS models, to be tested and evaluated.

The present study compared the LES predictions to DNS results for similar flows from the literature. There would be distinct advantages to performing an in-house DNS of this specific flow as a benchmark to assess the SGS models' effectiveness in predicting the impact of small eddies. For example, this would allow comparison of features of the SGS stress components to the filtered fields obtained from the corresponding small-scale eddies resolved by the DNS.

The current phase-averaged study has been performed based on just five phases and five periods, so it would be important to extend the number of phases and increase the averaging time to obtain more refined results, e.g. use 10 phases averaged over 50-100 periods.

The present study focused mostly on the mean and instantaneous velocity fields, but did not document the resolved-scale Reynolds stress components. It would be of specific interest to determine whether this transport feature, which is due to the larger resolved-scale eddies, is affected by the SGS model.

It is also recommended that the current results be used to investigate the mechanism of vortex-structure detachment from the prism, the role of the cap vortex, and the flow structure immediately behind the prism, where there seems to be no strong vortex elements.

In this study, the impacts of two different SGS models were explored on the mean and instantaneous flow structures and energy dissipation for a relatively low Reynolds number flow. Usually in low Reynolds number flows, the SGS energy and momentum are relatively small and become more significant in high Reynolds number flows. Hence it would be insightful to evaluate and compare two different SGS models (e.g., DSM versus DNM) for wake flows with higher Reynolds numbers. Greater differences at higher Reynolds numbers would be expected because the level of the SGS energy becomes more important as the Reynolds number increases.

The prism aspect ratio is another important parameter with significant influence on flow structure. The current thesis investigated the phase-averaged behavior for an aspect ratio of $AR = 3$, which is subcritical. It would be useful to perform further analysis of prisms with higher aspect ratios, especially with respect to their periodic and phase-averaged behavior. Usually a higher aspect ratio increases the unsteadiness of the flow and changes the dominant frequency. Also it would be insightful to reduce the aspect ratio to see how a low aspect ratio prism asymptotes to the behavior of a cube.

The boundary layer used in the present study was laminar and relatively thin. The next step would be to investigate the flow structure and effects of the SGS models on thicker and/or turbulent

boundary layers. For example, a pre-cursor flow could be simulated to provide an inflow turbulent boundary layer with a predefined thickness and also a specific turbulence intensity level.

This study documented that the stabilization methods typically used for the DSM had adverse effects on the prediction of the small-scale motions. Therefore, it would be worthwhile to investigate the performance of these – and other – SGS models in more detail, specifically to determine the effects of stabilization on the smallest scales and to develop novel stabilization methods that do not significantly alter these scales.